Electrical Properties of Grain Boundaries in Low Doped Polycrystalline Materials with Applications to Detectors

Mazharul Huq Chowdhury

A Thesis

In the Department

of

Electrical and Computer Engineering

Presented in Partial Fulfillment of the Requirements

for the Degree of Master of Applied Science at

Concordia University

Montréal Québec Canada

September 2010

CONCORDIA UNIVERSITY

School of Graduate Studies

This is to certify that the thesis prepared

By: Mazharul Huq Chowdhury

Entitled: Electrical Properties of Grain Boundaries in Low Doped Polycrystalline Materials with Applications to Detectors and submitted in partial fulfillment of the requirements for the degree of

Master of Applied Science (Electrical Engineering)

complies with the regulations of the University and meets the accepted standards with respect to originality and quality.

Signed by the final examining committee:

Dr. Dongyu Qiu Chair

Dr. Mojtaba Kahrizi Examiner

Dr. Benjamin C.M. Fung Examiner

Dr. M. Zahangir Kabir Supervisor

_____ Supervisor

Approved by William E. Lynch

Chair, Department of Electrical and Computer Engineering

September 2011 Christopher W. Truemen

Associate Dean, Faculty of Engineering and Computer Science

ABSTRACT

Electrical Properties of Grain Boundaries in Low Doped Polycrystalline Materials with Applications to Detectors

Mazharul Huq Chowdhury

Polycrystalline materials are widely used in large area electronic devices such as flat panel x-ray image detectors, and solar cells due to their suitability to deposit over large area at low cost. The performance of polycrystalline-based flat panel detectors are showing encouraging results (good sensitivity, good resolution and acceptable dark current) and give possibility to replace existing x-ray film/screen cassette. Therefore large area polycrystalline based flat panel detectors have opened new clinical possibilities and the polycrystalline solar cells give the opportunity of manufacturing low cost photovoltaic cells. Consequently, active research has been carried out to find out suitable polycrystalline materials (e.g. HgI_2, CdTe, CdZnTe, PbI_2, PbO etc) for various large area applications. However a polycrystalline material is composed of micro crystallites joined together by grain boundaries (complex structure, consisting of a few atomic layers of disordered atoms) which posses trap centers for charge carriers. Therefore, grain boundaries can trap a large amount of charges during detector operation. A potential barrier for drifting carriers may exist at the grain boundary, which controls the carrier mobility. Moreover, the performance of these polycrystalline detectors are affected due to the polarization phenomena (any change in the performance of the detector after the detector biasing) under applied bias.

Therefore, in this research work, an analytical model is developed to study the electrical properties (electric field and potential distributions, potential barrier height, and polarization phenomenon) of polycrystalline materials at different doping levels for detector and solar cell applications by considering an arbitrary amount of grain boundary charge and a finite width of grain boundary region. The general grain boundary model is also applicable to highly doped polycrystalline materials. The electric field and potential distributions are obtained by solving the Poisson's equation in both depleted grains and grain boundary regions. The electric field and potential distributions across the detector are analyzed under various doping, trapping and applied biases. The electric field collapses, i.e., a nearly zero average electric field region exists in some part of the biased detector at high trapped charge densities at the grain boundaries. The model explains the conditions of existence of a zero average field region, i.e., it explains the polarization mechanisms in polycrystalline materials. The potential barrier at the grain boundary exists if the electric field changes its sign at the opposite side of the grain boundary. The potential barrier does not exist in all grain boundaries in the low doped polycrystalline detector and it never exists in intrinsic polycrystalline detectors under applied bias condition provided there is no charge trapping in the grain.

To my loving parents

&

My wife, Sadeka Onam

ACKNOWLEDGMENTS

Foremost, I would like to thank my wife Sadeka Onam for her inspiration, support to complete the master's degree and especially for her patience during this endeavor. I am indebted to Dr. M. Zahangir Kabir for his continuous guidance, encouragement, help and financial support during the course of this research work. I also would like to extend my deepest gratitude to my parents, brother, and sister for giving me encouragement, support throughout my life. This work would not be possible without the warm, healthy and knowledgeable discussion with all the members of our research group. I am grateful to my colleagues Mr. Md. Wasiur Rahman, Mr. Md Shahnawaz Anjan, Mr. Md. Abdul Mannan and especially to Mr. Shaikh Asif Mahmood for their useful discussions. I also would like to show my gratitude to the professors and staffs at Concordia University. Many thanks go to Dr. Pouya Valizadeh for his encouragement during the course of my Master's program. Finally, I am gratefully to our creator almighty ALLAH.

TABLE OF CONTENTS

LIST OF FIGURES

LIST OF TABLES

LIST OF ABBREVIATIONS

a-Se	Amorphous Selenium
AMA	Active Matrix Array
AMFPI	Active Matrix Flat Panel Imager
CIS	Copper Indium Diselenide
CIGS	Copper Indium Gallium Selenide
CdS	Cadmium Selenide
CdTe	Cadmium Telluride
CdZnTe	Cadmium Zinc Telluride
CSS	Close Space Sublimation
EHP	Electron-hole Pair
FPD	Flat Panel Detector
GB	Grain Boundary
HgI_2	Mercuric Iodide
ITO	Indium Tin Oxide
PV	Photovoltaic

Pb	Lead
PbI_2	Lead Iodide
PbO	Lead Oxide
Pd	Palladium
PVD	Physical Vapor Deposition
PIB	Particle in Binder
TFT	Thin Film Transistor
SCR	Space Charge Region
Zn	Zinc

CHAPTER 1 INTRODUCTION

Polycrystalline materials are becoming increasingly important for large area devices (device consisting of large area, e.g. solar cell, LCD) through the possibility of replacing single crystal materials. It has received much attention as a material for low-cost photovoltaic devices, thin film solar cells, integrated circuit elements, flat panel displays and flat panel detectors [1]-[2]. Solid state devices replaced vacuum tubes since the invention of the transistor in 1947 by Bell Lab. There has been a rapid progress of the development in the solid state device and integrated circuit technology in making large area devices, with the invention of different fabrication technology for polycrystalline material based devices. A brief description of few important large area devices are given in the following sections.

1.1 Solar Cell

Solar cell is one of the important large area detectors to meet the future energy crisis as well as to overcome the issue of global warming caused by the consumption of the fossil fuel. A solar cell or photovoltaic cell is a semiconductor device that converts energy of sunlight directly into electricity by the photovoltaic effect. The first working solar cells were built by an American inventor named Charles Fritts in 1883 out of Selenium [3]. Although the efficiency of Fritts's solar cell was very low (less than 1%), his invention proved that it was possible to create electricity from sunlight. A solar cell consists of two thin layer of different type of semiconductor (one p-type and other n-type), sandwiched

together to form a pn-junction. A built-in electric field induces across the junction of these two layers (Figure 1.1). When sunlight strikes a solar cell, the photons of the absorbed light extricate the negatively charged electrons from the atoms. The free electrons then move through the cell, creating and filling in mobile positive charges, i.e., holes in the cell. In an ordinary pn junction these photo generated electrons and holes recombine after a short time and their absorbed energy waste away as heat. However in solar cell the mechanism is little bit different than ordinary pn junction. The generated electrons and holes near the junction are swept across in opposite directions by the influence of built-in electric field and other diffuse towards the junction to compensate the loss of electron and holes in the cell (Figure 1.1). Thus this movement of positive and negative charges generates electricity. The solar cell is produced on a glass substrate. The glass substrate is transparent, strong and cheap. Therefore this acts as a protective layer for the active cell. An anti-reflecting coating is applied to the cell to increase the absorption of light thorough the solar cell. The cell is finished with low resistance positive and negative terminals on the back.

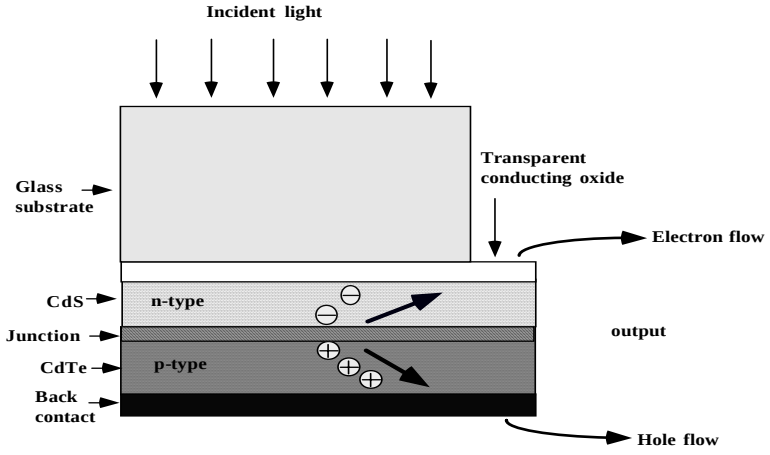

Figure 1.1 A schematic representation of CdS/CdTe solar cell.

One single solar cell produces a small amount of power (about ~ 2 watts). Therefore a number of solar cells are connected together in series and encapsulated a module to produce useful amount of output power. These individual modules further can be assembled into larger units called arrays (Figure 1.2). Cells within a module are implemented with bypass and blocking diode to avoid complete failure of the module with problem in an individual cell. Moreover, modules within an array are protected in similar fashion. This modular nature of the solar cell makes attractive for different types of applications.

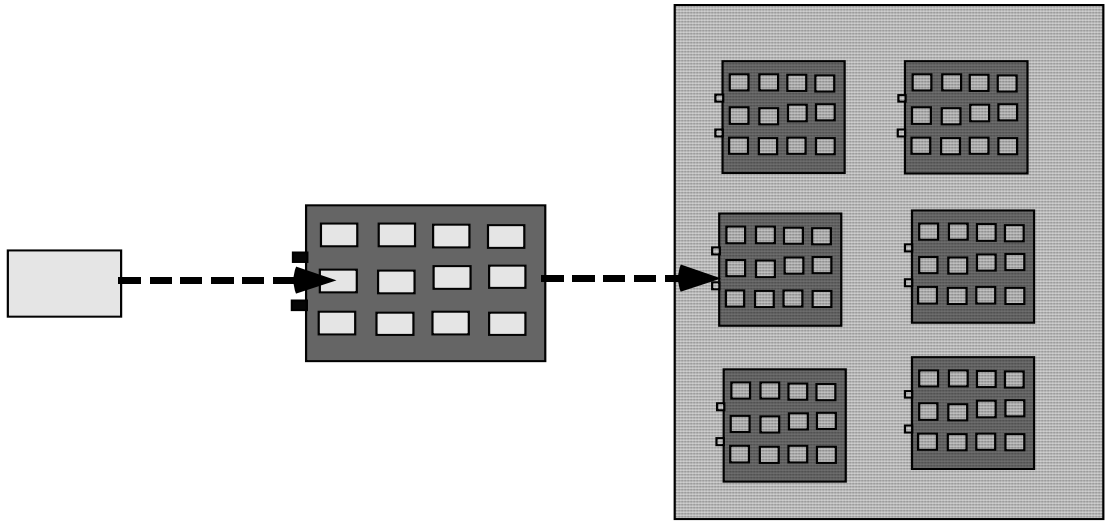

(a) (b) (c)

Figure 1.2 Modular representation of Solar cell, (a) cell (b) module (c)array of cells. The modular nature of solar cell allows great flexibility in applications.

The wafer-based crystalline silicon solar cells are referred as first generation of solar cells. Chapin *et al.* have developed first silicon solar cell at Bell Laboratory in mid 1950's [4]. The silicon solar dominates today's photovoltaic market. The best reported

commercial single crystal Si-solar cell has efficiency of about ~18% [5].The main factor behind the popularity of silicon based solar cell is that high quality Si has already been produced at large quantities by the conventional technique in the semiconductor industry. However the high fabrication cost (first generation solar cell) drive us to find out alternative technology [5]. Polycrystalline thin-films significantly reduce the cost of manufacture of photovoltaic (PV) modules and thus make solar cell economically viable. They need less thickness to absorb light energy and thus lighter compared to the crystalline cells. Moreover, polycrystalline thin films are tolerant of imperfect boundaries between crystallites, whereas crystalline devices typically demand significant consistency from one unit cell to other. Such tolerance results in thin-film polycrystalline thin-films being conformable to large-scale production. In addition, polycrystalline thin-films are more stable than some of the potential amorphous thin films.

Direct band gap materials are preferable for photovoltaic (PV) applications due to their high absorption coefficient [6]. However the maximum efficiency of solar cell can be achievable if the band gap of the materials lies in the range of ~1.2-1.8 eV [7, 8]. Therefore, materials like Cadmium telluride (CdTe, E_g~1.44), Cadmium selenide (CdS, E_g~1.67eV), Cadmium zinc telluride (CdTe, E_g~1.57-1.70) show good possibility as a potential polycrystalline solar cell [9, 10, 11]. Polycrystalline CdTe solar cells have demonstrated efficiency about 16.5% and Copper Indium Gallium Selenide (CIGS) show efficiency of more than 20% [12], [13],[14]. However, there has been active research going on to improve the efficiency of the polycrystalline thin-films solar cell [15]. The charge carrier diffusion lengths are shorter in polycrystalline thin film solar cells as

compared to crystalline solar cells. Therefore a p-i-n type structure is utilized in thin film solar cells so that carriers can be absorbed in wide i-layer and collected by the built-in electric field in i-layer.

1.2 Flat Panel Detector

Flat panel x-ray image detector is another important large area device used in digital radiography imaging system. The combination of large area thin film transistor (TFT) or switching diode self scanned active matrix array (AMA) and X-ray detection material constitutes the basis of the flat-panel X-ray image detector. Active matrix arrays are used in flat panel imagers, called Active matrix flat panel imagers (AMFPI). Existing imaging systems are easily adaptable to flat panel image detectors. AMFPI can easily use to perform fluoroscopy as they are able to read-out entire image in 1/30 seconds [16]. The fabrication and doping of large area hydrogenated amorphous-silicon (a-Si: H) films became technologically possible in the early 1990s, which helped a lot to the development of AMA [17].

Flat panel x-ray image sensor is replacing existing x-ray film/screen cassette and enable a clinical transition to digital radiography [18], [19], [20]. It can provide image immediately after the patient's exposure, monitor the quality of image and automatically adjust the exposure settings as necessary so that a better, real-time x-ray image can be available for analysis. Therefore these detectors are ideally suited for fluoroscopic procedures. Moreover, image can be stored on a computer disk easily rather than in archaic film stacks and transfer electronically over computer networks for expert opinion;

the radiation doss is less compared to the conventional x-ray detection system, therefore, biological effects due to radiation is decreased. In digital flat panel detector there is no need for chemical materials to develop image so the risk of using hazardous material is removed. Thus, it provides a more convenient patient management with less handling and computer-aided diagnosis system. Figure 1.3 shows a schematic diagram of digital radiography system. Besides, several advantages Flat panel detector system has some drawbacks such as high cost, limited high contrast resolution etc.

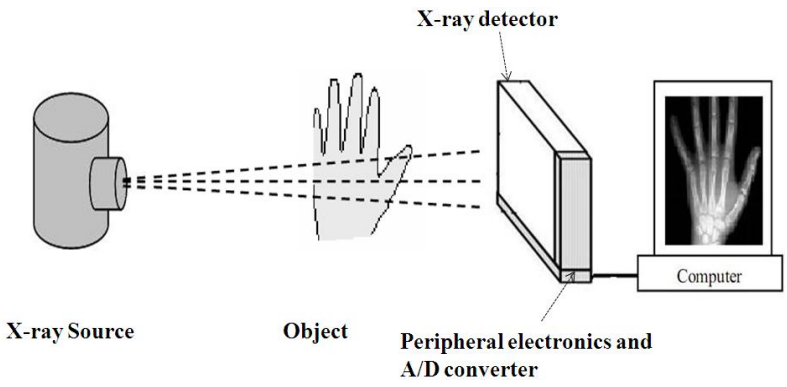

Figure 1.3 Schematic diagram of digital x-ray image detector (Flat-panel panel detector).

Two types of flat panel x-ray detection processes can be used such as: (i) Indirect conversion and (ii) direct conversion approach. The indirect conversion detector consists of phosphor layer (e.g. a screen such as Gd_2O_2S:Tb , structured scintillator such as CsI:TI) in intimate contact with an AMA (Active Matrix Array) to convert the x-ray radiation into visible light [18], [21]. The structure of indirect conversion detector is illustrated in Figure 1.4. The intensity of the light emitted from a particular location of the phosphor layer is proportional to the intensity of the x-ray radiation incident on the surface of the x-

ray detector at that particular pixel. A photosensitive layer or a p-i-n diode is incorporated in the each pixel of the AMA to convert the light signal into an electrical signal (such as charge) and stored this charge until the AMA is readout. The magnitude of the electrical charge from the different pixel contain the information about the imaging information of the object inherent in the variation of x-ray's intensity. Therefore, the complete process of getting x-ray image from indirect detector involves two steps: (1) First, the conversion of X-ray radiation into visible light and (2) Conversion of visible light into electrical signal . Hence, the performance of indirect conversion x-ray detectors depend on the efficiency of intermediate step (x-ray radiation to light).

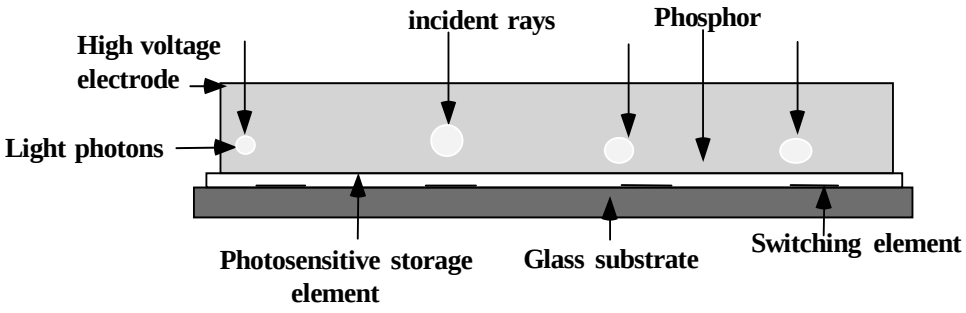

Figure 1.4 Schematic illustration of indirect conversion flat panel x-ray imaging systems.

Direct conversion detector can directly records the electrical signal (Figure 1.5) with the help of thick layer of photoconductor material [18], [19]. The electrical charges that are produced by the photoconductor material are proportional to the amount of radiation received by the detector. Direct conversion detectors consist of a solid-state x-ray sensitive photoconductive material (e.g. HgI_2) and two metal electrodes. A thick layer of photoconductive material is coated over the actve matrix array and an electrode is

deposited on top of the photoconductor. A simplified cross sectional view of the two pixels of direct conversion flat-panel x-ray image detector depicts in Figure 1.5 [22]. A high atomic number, large bandgap semiconductor such as polycrystalline HgI_2 layer is coated onto the AMA to serve as a photoconductor layer. In order to facilitate the application of a biasing potential a top or radiation receiving electrode, T, is sputtered onto the surface of the photoconductor (e.g. HgI_2). The bias potential creates an electric field, F, which drives the generated carriers either to the top electrode or charge collection electrode, B. The voltage applied to the top electrode is either positive or negative. This voltage may vary from several hundred to thousand volts and most of the applied bias voltage drops across the photoconductor layer since the pixel capacitance, C_{ij} is larger than the capacitance of the photoconductor layer.

During the x-ray exposure, x-ray photons that pass through a patient, generate electron-hole pairs (EHPs) in the photoconductor layer. The movement of the electrons and holes are governed by the applied bias. If positive bias is applied on electrode T, electrons are drift to the top electrode and holes are drift to the bottom electrode where they are collected and stored by the pixel capacitor C_{ij} and vice versa for negative applied bias on electrode T. Collected carriers (electron or hole) provide a charge signal Δq_{ij} (proportional to the the amount of incident radiation absorbed within the pixel area) on the pixel storage capacitor C_{ij}. The charge signals are scanned by the self-scanned electronics and constitute an x-ray image.

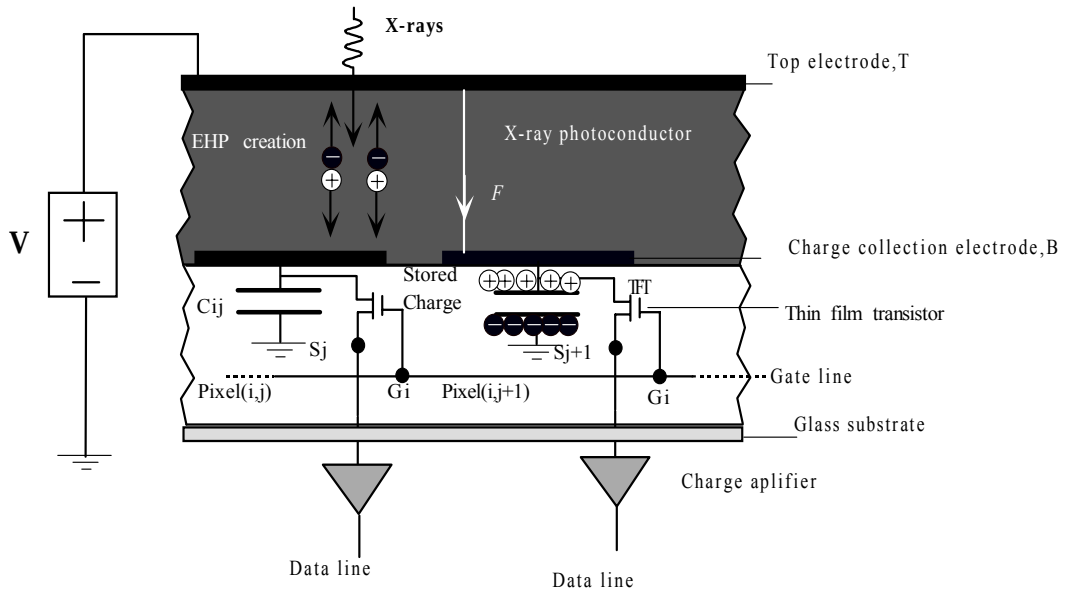

Figure 1.5 A Schematic diagram of cross-sectional view of the detector structure for flat panel direct conversion (e.g. HgI_2 based detector) digital x-ray detectors (two pixels).

It has been found that the direct approach has several advantages over indirect approach. First, the image quality of direct conversion detectors is superior to indirect one. Again, direct conversion detectors are simple, compact cheaper and easier due to their simpler structure [23]. The lateral spreading of the x-ray generated response is less in direct conversion detector. Therfore, in direct detector the x-ray generated response can be measured at the position in the image plane where the x-ray photon is absorbed. On the otherhand, indirect detectors suffer from blurring due to the scatter of optical photons by the phosphor grains [24]. Secondly, the sensitivity of an indirect detector is governed by the relative low x-ray sensitivity of the phosphor screen. However, the absorption efficiency of solid-state detector can be maximized by using suitable photoconductor materail, operating bias, and photoconductive layer's thickness [25].Thus direct conversion detector has become a major choice in digital radiography [18, 26]. However

the material properties over the large area detector have to be uniform and the detector response has to be linear. Therefore, the choice and design of the x-ray photoconductor is one of the challenges in digital x-rays. Only amorphous (e.g. a-Se) or polycrystalline photoconductors (such as HgI_2, PbI_2, PbO, CdTe etc) are currently practical for large area x-ray image photoconductor in flat panel x-ray imager [27, 28].

The large area coating requirement (e.g. 35 cm × 43 cm for chest radiography or greater) the use of crystalline materials as x-ray photoconductor is ruled out due to their difficulty to grow in large areas. Only amorphous and polycrystalline materials are fulfill this requirement and thus suitable as a large area photoconductor. Direct conversion flat panel detectors based on a-Se photoconductors has been made commercially available by the use of two amorphous semiconductors such as amorphous silicon (a-Si:H) and amorphous selenium (a-Se). Amorphous silicon is used to develop large are TFT. Both these can be easily prepared in large areas, which is essential for developing large area detector.

Although, stabilized a-Se is the preferred choice for the photoconductor, there has been an active research to find alternative photoconductors to replace amorphous selenium in flat panel image detectors due to its high ionization energy $W_{\pm}$ (~45eV at typical applied electric field of 10V/μm) and very high applied bias (KV range) [29]. The energy required to create a single electron-hole pair is called the ionization energy. Whereas, the value of ionization energy is typically 5-6eV for polycrystalline materials such as

mercuric iodide (HgI_2), cadmium zinc telluride (CdZnTe). However polycrystalline detector suffers adverse effect of non-uniform response due to large grain size and also the charge carrier transport properties of the polycrystalline materials are limited by the grain boundary trapping effect. There has been active research going on to improve the dark current of ploy crystalline material (HgI_2, CdZnTe) [30]-[31] and HgI_2, PbI_2, CdZnTe (< 10 % Zn), and PbO polycrystalline x-ray photoconductor have shown encouraging results [32, 33, 34].

1.3 Research Motivations

Polycrystalline based direct conversion flat panel x-ray image detectors with an active matrix array have been provide excellent image quality, immediate readability and the ability to be send the images electronically. Polycrystalline materials have shown better x-ray absorption and low electron hole pair generation energy than commercially available a-Se based flat panel detector [22, 35]. Therefore extensive research has been carried out to find out suitable polycrystalline material to replace the a-Se based photoconductor [11, 36, 37, 38].The polycrystalline HgI_2 imagers show excellent sensitivity, good resolution and acceptable dark current which makes the material a good candidate for medical x-ray image detectors among the potential replacement of a-Se based detector [37]. Moreover recent research shows that the cost of thin-film polycrystalline solar cell is lower compared to the single crystal solar cells [5]. In addition the thin-film solar cells use lesser amount of raw materials and thus lighter

compared to the crystalline cells. The polycrystalline solar cells (e.g. CdTe) also show higher efficiency. However a polycrystalline material is composed of micro crystallites joined together by grain boundaries (complex structure, consisting of a few atomic layers of disordered atoms). A several crystallographic defects such as dislocations, vacancies, interstitial, dangling bonds, and distorted bond angles can be originated at the grain boundaries. All these irregularities of the inter-atomic bonding at the grain boundaries lead to the formation of electronic states. These electronic states may have energies in the bandgap and these intra band gap states act as a trap centers for carriers. Therefore, grain boundaries can trap a large amount of charges during detector operation. A potential barrier for drifting carriers may exist at the grain boundary, which controls the carrier mobility. Therefore, it is well believed that the properties of grain boundary region control the carrier transport properties of the polycrystalline materials. This may affects the charge collection efficiency.

Moreover the performance of some polycrystalline detectors (e.g. HgI_2, CdTe etc) are affected due to the polarization phenomena under applied bias [11, 37]. The polarization effect is defined as any change in the performance of the detector after the detector biasing. The polarization phenomena occur due to the charge trapping and de-trapping at the grain boundary interfaces. This also significantly affects the charge collection efficiency of the detector. One important consequence of the polarization effect is the existence of a zero average electric field region in some portion of the detector under applied bias, which significantly affects the charge collection efficiency of the detectors.

In solar cells or detector applications, intrinsic or lightly doped polycrystalline materials are used. Seto *et al.* has proposed a comprehensive model to explain the charge transport phenomena in polycrystalline materials by solving the one-dimensional Poisson's equation in the depleted grain region [39]. Seto's model has not considered the finite width of the grain boundary region and the effect of applied bias. Later, Greuter *et al.* has extended the Seto's model by incorporating the effect of applied bias [40]. All the previous models have considered equal amount of charges (with opposite polarity) in the grain boundary and depleted grain regions (i.e., there exists the charge neutrality in the material). However, the grain boundaries can possess more trapped charge compare to the depleted bulk grain in intrinsic or low-doped detectors under light illumination and thus imbalance the charge neutrality. Therefore, none of these previous models is applicable for low or intrinsic doped polycrystalline materials. Moreover, the polarization phenomena in polycrystalline detector under applied bias cannot be explained through these models. Therefore, it is necessary to develop a general grain boundary model considering an arbitrary amount of grain boundary charge, doping, biasing and a finite width of grain boundary region.

1.4 Research Objectives

In polycrystalline materials some of the photo-generated carriers (electrons or holes) are trapped in the grain boundary trap centers (from which there is no escape over the time

scale of charge read out) during their travel towards the charge collecting electrodes. The trapped charges reduce charge collection efficiency and also change the electric field distribution. The electric field may collapse in some portion of the detector thickness, which depends on the grain boundary properties, doping levels, the amount of trapped charges, grain size, the total detector thickness and the applied bias. The overall objectives of this research work are,

(i) To develop a general analytical grain boundary model for electrical properties of polycrystalline materials considering an arbitrary amount of grain boundary charges, doping, bias voltages and a finite width of grain boundary region so that the model can be applicable for any doping levels of the polycrystalline materials.

(ii) To analyze the electrical properties (e.g. electric and potential distributions, charge carrier barrier height) of grain boundaries in polycrystalline detectors under low or intrinsic doping at applied bias condition. Polycrystalline mercuric iodide (HgI_2) detector is taken as an example.

(iii) To extend the model for heavily doped polycrystalline materials under applied bias condition.

(iv) To explain the polarization phenomenon in polycrystalline based detectors. The conditions of existence of an energy barrier at the grain boundary and a zero average field region in some portion of the detector will also be determined.

The proposed model has been applied to polycrystalline HgI_2 photoconductors. However the same model can be applied to other polycrystalline photoconductive materials (e.g., poly-CdZnTe, poly-PbI_2) used in detector and solar cell applications.

1.5 Thesis Outline

The thesis is divided into five chapters. This chapter introduces the basic description of large area detectors, e.g., solar cell, flat panel detectors and also fabrication requirement of the large area detectors. The second chapter provides comparison of different photoconductive materials in large area polycrystalline detectors along with previous grain boundary models. The proposed analytical model and its detail analysis are given in chapter three. Chapter four presents results and discussions. Finally, Conclusions, contributions and future work are summarized in chapter five.

CHAPTER 2 BACKGROUND THEORY

The photoconductor used in large area detectors plays an important role to determine the performance of the device. The photoconductor acts as a photon to electrical charge transducer and thus controls the charge collection of the detector. In this chapter, the properties of some potential polycrystalline photoconductor will be discussed for large area detector along with previous grain boundary models.

2.1 Polycrystalline Based Photoconductor

A polycrystalline material is composed of micro crystallites joined together by grain boundaries (Figure 2.1). The atoms are arranged in a periodic manner inside each grain but differ from orientations of other neighboring grains. Therefore, each grain can be considered as a small single crystal and band structure, absorption coefficient is virtually identical to that of the single crystalline material. However, both electrical carrier transport and recombination properties are governed by the grain boundaries. The grain boundary is a complex structure, consisting of a few atomic layers of disordered atoms. At grain boundary, crystal lattices of neighboring regions do not match perfectly. Atoms in the grain boundary represent a transitional region between different neighboring crystallites. The orientations of grain boundary surfaces may vary over a large angular range. Therefore, a several crystallographic defects such as dislocations, vacancies,

interstitials, dangling bonds, and distorted bond angles can be originated at the grain boundaries. Polycrystalline materials may contain extrinsic impurities which are also likely to concentrate at the grain boundaries. All these irregularities of the inter-atomic bonding at the grain boundaries lead to the formation of electronic states. These electronic states may have energies in the bandgap and these intra band gap states act as a trap centers for carriers. Every defect has its own energy, defect density (cm^{-2}), and capture cross sections for carriers (electrons or holes). Defects can be either 'shallow defects' or ' deep defects', shallow defects act as electron traps (acceptors) when they located near the conduction band or act as hole traps (donors) when they located near the valance band. Deep defects may be capable of trapping either type of carrier as they located at energies center of the bandgap.

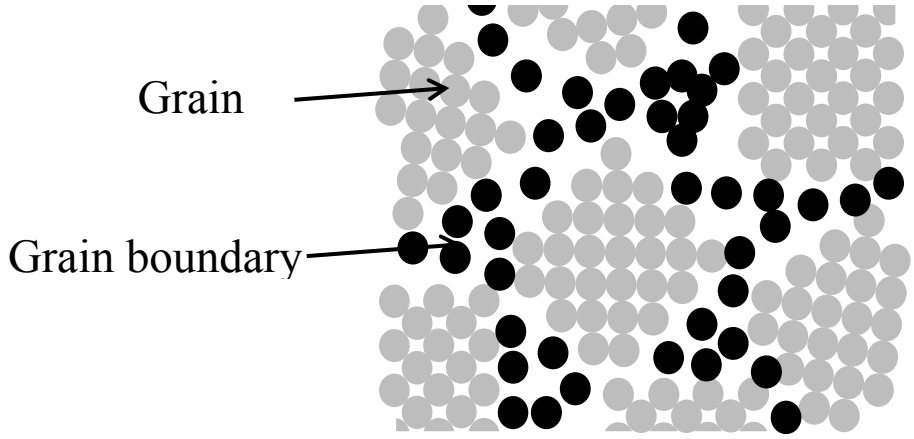

Figure 2.1 A schematic view of grain boundaries in polycrystalline materials.

The polycrystalline materials may have several defect levels at the grain boundary interface. These defects level may be continuous if the density of defects are very high.

But it is sufficient to model the grain boundary using one or few defect levels around the center of the bandgap.

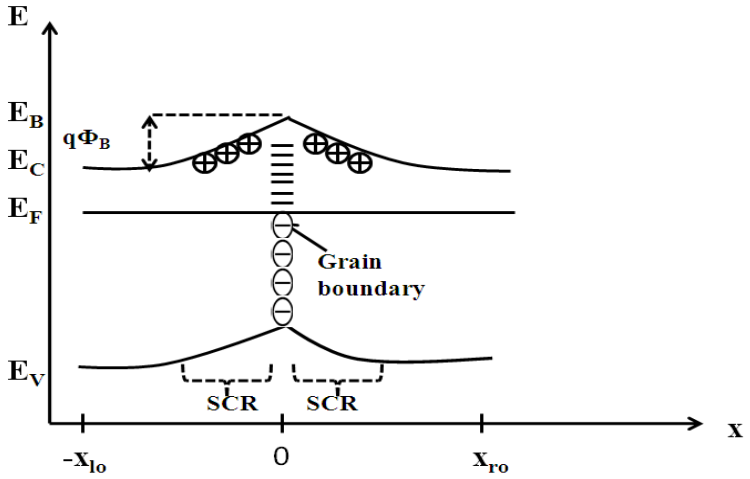

Figure 2.2 Band diagram of polycrystalline material (n-type).

The trapping states of grain boundary interface traps majority carriers (electron in n-type materials) from the crystallites, when these carriers are attempting to move from one grain to other. Thus these trap states immobilize the majority carriers and become charged, which in turn create a space charge region (SCR) near the grain boundary. The charge density of space charge region is governed by the doping density. Therefore, the majority carrier concentrations are reduced within the bulk of the crystallites. Figure 2.2 depicts this situation for n-type polycrystalline material, showing the negative grain boundary charges (GB) and positive space charge regions (SCR) surrounding the GBs. The charge neutrality condition controls the length of the SCR. A band banding (E_B=$q\Phi_B$) occurs at the GBs due to the electric field of the space charge region.

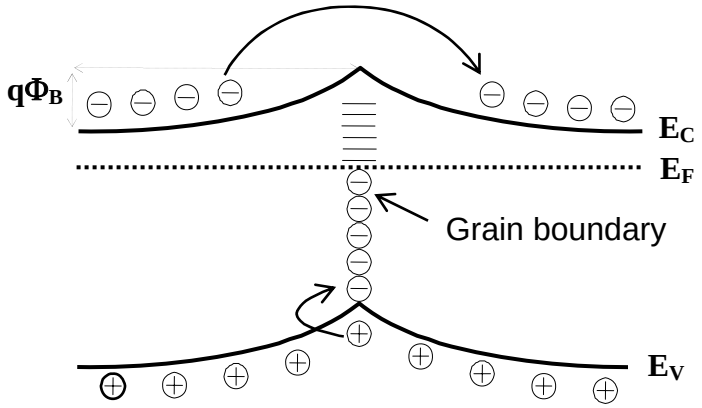

Figure 2.3 Majority and minority carrier movement (n-type) through grain boundary interface.

The band banding has effects on the electrical transport and carrier recombination. Figure 2.3 depicts that majority carriers (electron for n-type materials) have to overcome the potential barrier height (Φ_B) while crossing from one crystallite to other and thus the mobility of the carriers decrease. Minority carriers (hole for n-type materials) also suffer due to the grain boundary effect under illumination of light. Grain boundary interface act as sinks for the minority carriers (Figure 2.3), once they reach the GBs they recombine with the trapped majority carriers. Therefore, Grain boundary effects influence the electrical properties of polycrystalline material in several ways.

a) Grain boundaries barrier reduce the mobility of majority carrier (electron for n-type material) and thus increase series resistance.
b) The minority carriers' recombination at grain boundaries with the trapped majority carriers reduces lifetime of minority carriers.

The charge collection of polycrystalline detectors is affected due to these reasons. Therefore a theoretical model for explaining the electrical properties in polycrystalline is necessary to improve the performance of polycrystalline based detector.

2.1.1 Mercuric Iodide (HgI_2)

Polycrystalline Mercuric Iodide has been used as an x-ray photoconductor for several years in medical imaging application (e.g. mammographic, radiographic, fluoroscopic) and it can be fabricated by two different methods: (i) Physical vapor deposition (PVD) or (ii) Particle in binder (PIB) in which HgI_2 is gluing with poly-metric type binder [41], [42]. A bias electrode (a several hundred angstroms of Pd or Au) is deposited on top of the deposited HgI_2 film (which is deposited onto either conductive e.g. ITO, gold coated glass plates or a-Si TFT arrays) followed by a polymer encapsulation layer [43].The large area HgI_2 based flat-panel detector of size 20 cm x 25 cm for radiographic and fluoroscopic medical application are reported [43].The HgI_2 layer thickness varies from 100-500μm, grain size varies from 20-60μm. The energy bandgap E_g=2.1eV, the density of poly-HgI_2 is 6.3 gm/cm^3, the electron hole pair (EHP) creation energy $W_{\pm}$~5eV, the relative permittivity ε_r=8.3 and the resistivity of this material is ~40GΩ-cm [41], [44].

The charge transport properties ($\mu\tau$) are superior for electrons to holes in the HgI_2 materials. The $\mu\tau$ products for electrons in PVD HgI_2 is higher and it is reported in the range of 1×10^{-5} to 1×10^{-4} cm^2/V, which is comparable to that of single crystal HgI_2 [30], [45]. PVD sample with larger grain size have increasing $\mu\tau$ as the larger grain size may have fewer grain boundary defects. But larger grain size cause non-uniform response of

the x-ray photoconductor. However, this non uniform response can be improved by keeping the grain size smaller than the pixel size of the detector [32]. It is reported that the HgI_2 x-ray photoconductor with smaller grain sizes show good sensitivity with an acceptable uniform response.

2.1.2 Lead Iodide (PbI_2)

Lead iodide (PbI_2) is one of the promising polycrystalline materials for direct conversion x-ray detector [46]. PbI_2 photoconductive layers have been grown using PVD on substrate coated with ITO or gold electrodes [47]. A large area direct conversion AMFPI of 20x25 cm^2 size have been demonstrated by using PVD poly-PbI_2 of 60-250 μm thick for radiographic imaging application [48]. The high atomic number (Z_{Pb}~82, Z_I~53) of PbI_2 makes it efficient x-ray absorber compared to a-Se (Z~34). The band gap energy, E_g~2.3 eV, resistivity is around 10×10^{13}Ω-cm, and ionization energy $W_{\pm}$~ 5eV, [47], [49].The charge transport ($\mu\tau$) property of PbI_2 of holes and electrons are 1.8×10^{-6} cm^2/V and 7×10^{-8} cm^2/V respectively [48]. The hole mobility in PbI_2 is controlled by the shallow trap as the μ_h in poly-PbI_2 and single crystal PbI_2 are in the range of 0.02-0.15 $cm^2/V.s$ and 2 $cm^2/V.s$ respectively [50].

2.1.3 Lead Oxide (PbO)

Brauers *et al.* was first demonstrated a small TFT based receptor based on Lead oxide in 1998 and recently, a large area (18 cm x20 cm; 960x1080 pixels) direct conversion flat

panel detectors with ~300μm thick PbO has been reported [34], [51]. PbO photoconductive layer have been prepared through direct evaporation process onto the substrate in a vacuum chamber where the substrate temperature was about 100^{o}C and the temperature of crucible (source material) temperature was 900-950^{o}C [52]. Through this technique a 300μm thick PbO is possible to deposit. A deposition of 100nm to 200nm thick Al, Au or Pd is used to form top electrode.

PbO is a good x-ray absorber and also heavy element K-edges are absent in PbO for the entire diagnostic range up to 88 keV. The band gap of PbO is E_g~1.9 eV, the ionization energy $W_{\pm}$~8eV, density is 4.8 gm/cm^3, and the resistivity of this material is 7×10^{12}Ω-cm -10×10^{12} Ω-cm [34], [52]. The electron charge transport ($\mu\tau$) of the PbO is about 5×10^{-7} cm^2/V [34]. PbO photoconductive layer suffers due to residual signal lag which is around 10% and is quite high for imaging application. Therefore, residual lag should improve to compete with the other potential candidate of direct conversion flat-panel detector.

2.1.4 Cadmium Telluride (CdTe)

Polycrystalline Cadmium Telluride (poly-CdTe) have attracted increasing interest as both x-ray detector and solar cell due to their high photon absorption efficiency, wide band gap, good room temperature performance, high detection efficiency and also good mechanical and chemical stability [9], [11]. The band gap of CdTe is about 1.44eV at room temperature and it has the photon absorption coefficient is about ~5×10^4 cm^{-1} for visible light [53]. Therefore 2-μm thick CdTe films give good enough efficiency in photovoltaic (PV) applications. The theoretical efficiency achieved in the CdS/CdTe solar

cell is about 30%, however the reported efficiency is about 16% [12], [53]. CdTe is also a good x-ray absorber due to its high atomic number Z_{Cd}~48, Z_{Te}~52. Therefore it is used as a potential candidate for flat panel detector. However, it suffers from high leakage current due to low resistivity of ~1×10^9 Ω-cm [11]. CdTe can be deposited by electro deposition or close-space sublimation (CSS) and a post deposition is required for doping, grain growth and resistivity reduction at temperature above 400^{o}C [53].

2.1.5 Cadmium Zinc Telluride (CZT)

Single crystal Cadmium Zinc Telluride (CZT) is not suitable for large area devices due to the difficulty in manufacturing defect free, uniform, high resistive large area wafers and on the other hand poly-CZT material can be grown with lower cost than that of single crystal material [52],[54]. Moreover CZT has potential for preparation of high efficiency tandem solar cell due its bandgap of E_{gCZT}~1.45-2.26eV [55]. CZT thick films have been deposited by closed space sublimation (CSS) method at the furnace temperature is about 600^{o}C and a sintered mixture of CdTe and ZnTe was used as a source material [33]. A 350μm Cl-doped poly-CZT (*Zn=4%)* with a average grain size 4-5 μm was reported [54].

The resistivity of CZT is one or two order of magnitude greater than that of CdTe and thus the leakage current is lower [11]. The poly-CZT Schottky diodes with Indium contact exhibit the leakage current around 14 nA/cm^2 at an operatic applied bias of 40V [56]. Hole mobility in CZT decrease with the increase of Zn concentration but the

electron mobility remains nearly constant. The charge transport properties ($\mu\tau$) for holes and electrons of poly-CZT ($Cd_{0.95}Zn_{0.05}Te$) are 3×10^{-6} cm^2/V and 2×10^{-4} cm^2/V respectively. The carrier transport properties ($\mu\tau$) of Poly-CZT are poorer than that of single crystal CZT is due to the carrier scattering at the grain boundary.

2.1.6 Copper Indium Gallium Selenide (CIGS)

Copper Indium Gallium Selenide has been attracted as a potential material for solar cell in past 10 years due to its optimum bandgap for solar energy conversion. The bandgap of CIGS varies 1.04 to 1.67 eV [57]. The maximum efficiency of solar cell can be achievable if the band gap of the materials lies in the range of ~1.2-1.8 eV [7]-[8]. However depending on the composition the band gap of the CIGS varies and thus has impact on the efficiency. The reported efficiency for CIGS solar cell is about 20% [12]-[15]. Like other thin-film photovoltaic technologies, these films can be deposited onto cheap substrates at low temperature [55].

The properties of several potential photoconductors for both flat panel direct conversion detectors and solar cell have been discussed. The poly-HgI_2 receptors show excellent sensitivity, good resolution, acceptable dark current, low electron hole pair generation energy for flat panel detector. Large grain sizes improve the charge transport properties as the number of grain boundary interfaces decrease but it causes non-uniform response. Therefore the grain size must be kept smaller than the pixel size to get uniform response in image detectors. The CZT detectors are both mechanically and chemically more stable [33]. Moreover CZT has shown good possibility as solar cell by overcoming the leakage

issue in CdTe based solar cell. The grain boundary interface of the poly-CZT may influence on both non-uniformity and stability of the output. However, polycrystalline materials are showing good prospects as a direct conversion flat panel x-ray photoconductor and solar cell due to their high absorption ability, low ionization energy, low cost of production; but still these suffer image lag, high dark current (dependent on applied bias), lack of uniform response, low photovoltaic efficiency compare to single crystal solar cell. The charge transport properties in polycrystalline materials are controlled by the grain boundary interfaces.

2.2 Polycrystalline Grain Boundary Model

The electrical transport properties of polycrystalline materials have been interpreted in two different ways [39], [58]: (i) the segregation theory, and (ii) the grain-boundary trapping theory. According to segregation theory, the grain boundary act as a sink for impurities due to impurity segregation at the grain boundary, and impurities are electrically inactive there. However, this segregation model does not explain the temperature dependency of the film resistivity []. In case of grain-boundary trapping model, a large number of defects are considered at the grain boundaries. These defects are due to the incomplete atomic bonding of disordered atoms at the grain boundary, act as trapping states for carriers, and immobilize them. The traps are creating a potential barrier for carriers as they become electrically charged after trapping the mobile carriers. Therefore, the mobility of carriers is reduced. Based on these thoughts several models were developed. In this chapter, we will discuss these models.

2.2.1 Seto's Grain Boundary Model

Seto has developed a comprehensive theory of transport phenomena in polycrystalline materials (e.g. polysilicon) by combining the grain-boundary trapping model with a thermionic emission mechanism through the grain boundary barriers [39]. The electrical transport properties of polycrystalline material are governed by carrier trapping at the grain boundary. This model is based on the calculation of the energy barrier at grain boundaries due to carrier trapping. Following assumptions are made to develop this model,

a) Polycrystalline silicon is composed of identical crystallites having small grain size of length L_{GB} unit, and cubic shape. Practically, in a real polycrystalline materials consist of irregular shapes grains, but for simplicity these grains are assumed to be identical.
b) The representation of polycrystalline silicon is mono-dimensional for the purpose of calculating its transport properties, although it is a three-dimensional substance.
c) Band structure of mono-crystalline silicon is assumed to be applicable inside the crystallites.
d) The grain boundaries are assumed to be of negligible thickness compared to the thickness of grains, L_{GB}.
e) The defects are considered as a carrier trap centers that are located only in the grain boundaries. These trap centers are assumed to be initially neutral and become charged by trapping carriers (electrons or holes) and the trap concentration is defined in per surface unit.

f) The traps are acceptors in the n-type **(**N_{TA} per surface unit**)** and donors in the p-typed (N_{TD} per surface unit**)** semiconductors.

g) The trap energy level, E_T is located more or less in the middle of the forbidden band i.e. near the intrinsic Fermi Level, E_i.

h) Doping concentration (N_D**,** donor doping concentration in n-type or N_A, acceptor doping concentration in p-type) in polycrystalline silicon is uniform and all the doping atoms are ionized.

By using the above assumptions and abrupt depletion approximation, Seto has calculated the energy band diagram in the crystallites [39]. Figure 2.4 gives a one-dimensional presentation of n-type polysilicon along with the charge distribution and energy band diagram. The mobile carriers in the region ($L_{GB}/2$ -X_{lo}) or ($L_{GB}/2$ –X_{ro}) from the grain boundary are trapped by trapping states , which in turn results a depletion region on both sides of the grain boundaries.

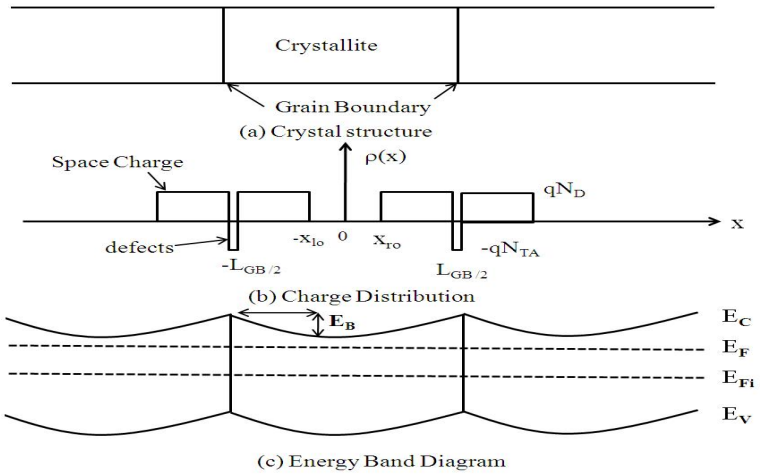

Figure 2.4 (a) crystal structure of polysilicon, (b) the charge distribution in polysilicon, (c)energy-band diagram in polysilicon.Defects are electrically active at grain boundaries.

This space charge layer is made of ionized doping atoms (donor in n-type polysilicon), maintain the charge neutrality and also compensate the equivalent trapped charges located at the grain boundary. An abrupt depletion approximation is used to calculate the energy band diagram while solving the Poisson's equation in the grain. Using the above mentioned approximation, the energy barrier height E_B is determined as,

$$E_B = \left(\frac{q^2 2N_D}{8\varepsilon_s \varepsilon_o} \right) X^2 \qquad (2.1)$$

Where, ε_o = permittivity in vacuum, ε_s = semiconductor permittivity. X= extension of the space charge (X_{lo}+X_{ro}).

The value of X has to maintain the charge neutrality i.e.

$$qXN_D = qN_{TA} \qquad (2.2)$$

Therefore space charge extension is, $X = \frac{N_{TA}}{N_D}$ depending on the exact values of N_D and N_{TA}, $X/2$ cannot be higher than $L_{GB}/2$. Seto's model defines a critical doping concentration as follows:

$$N_D^* = \frac{N_{TA}}{L_{GB}} \qquad (2.3)$$

For a fixed trap density, there exist two possible conditions depending on the doping concentration:

a) Case $N_D < N_D^*$:

In this case the effective doping concentration is not high enough to compensate the equivalent trap charge concentration at grain boundaries and the crystallite is

completely depleted of carriers, traps are partially filled (N_{TA}^-). Therefore, the energy barrier height E_B can be written as,

$$E_B = \left(\frac{q^2 N_D}{8\varepsilon_s \varepsilon_o} \right) L_{GB}{}^2 \quad ; X = L_{GB} \tag{2. 4}$$

b) Case $N_D > N_D^*$:

In this case, the effective doping concentration is higher than the critical doping concentration, the space charge layer is lower than the grain size ($X < L_{GB}$). Therefore, the energy barrier height E_B is given by,

$$\begin{aligned} E_B &= \left(\frac{q^2 N_D}{8\varepsilon_s \varepsilon_o} \right) \left(\frac{N_{TA}}{N_D} \right)^2 \quad ; X = \frac{N_{TA}}{N_D} \\ \Rightarrow E_B &= \left(\frac{q^2}{8\varepsilon_s \varepsilon_o} \right) \frac{N_{TA}^2}{N_D} \end{aligned} \tag{2. 5}$$

Therefore the energy barrier height is independent of the crystallite size, L_{GB}. The barrier height decreases with the increase of doping. Therefore polysilicon resistivity tends to approach the crystalline resistivity at a very high doping.

From the above results, the barrier height can be plotted as function of the doping concentration with the grain size as shown in Figure 2.5.

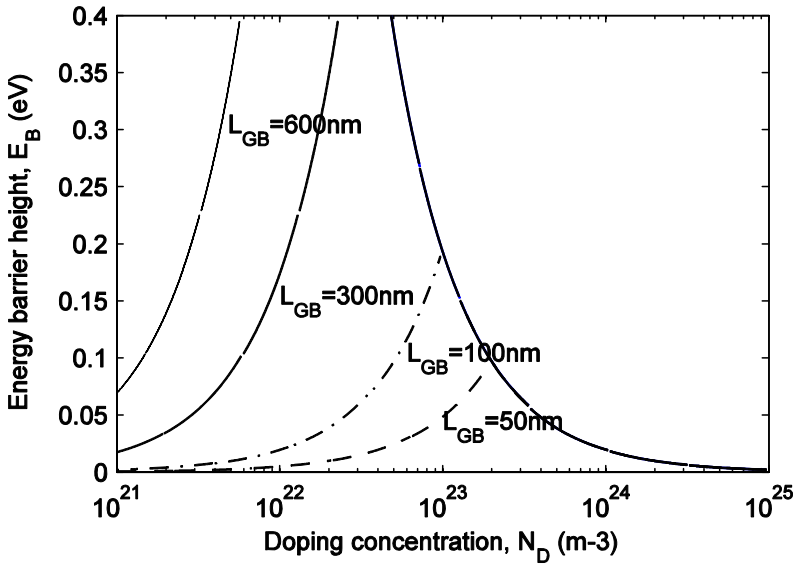

Figure 2.5 Dependence of the energy barrier as a function of doping concentration in polysilicon material $N_{TA}=1\times10^{16}\text{m}^{-2}$, E_T is located at midgap.

Seto's model leads to unrealistic results for the large grain size. All the curves are superimposed for higher doping concentration. Here, it is shown that in case of polysilicon the barrier height becomes too high to be realistic for grain size, L_{GB} larger than 300 nm. Therefore the energy barrier height of polycrystalline can be calculated by seto's model if the grain size is small enough, depending on the trapping states in the grain boundaries (N_{TA}).

2.2.2 Improvement of Seto's Model

Baccarani *et al.* has been proposed an improvement of Seto's model by taking into account the progressive ionization of the traps as a function of the position of the Fermi

level []. In case of n-type polycrystalline, the traps are acceptor in nature. The electron concentration is governed by the following Fermi-Dirac statistics for acceptor-like traps,

$$N_{TA}^{-} = N_{TA}\left(1+e^{\left(\frac{E_T-E_F+E_B}{kT}\right)}\right)^{-1} \tag{2. 6}$$

The barrier height can be calculated by using the following equation (seto's model),

$$E_B = \left(\frac{q^2 N_D}{8\varepsilon_s\varepsilon_o}\right)X^2$$

However the critical doping concentration can be deduced from the charge neutrality condition according to the following relation,

$$\begin{aligned} & qXN_D = qN_{TA}^{-} \\ \Rightarrow\ & XN_D = N_{TA}^{-} \\ \Rightarrow\ & XN_D = \left(\frac{N_{TA}}{1+e^{\left(\frac{E_T-E_F+E_B}{kT}\right)}}\right) \\ \Rightarrow\ & N_D^{*} = \left(\frac{8\varepsilon_s\varepsilon_o}{q^2 L_{GB}^2}\right)\left(E_F - E_T + kT\ln\left(\frac{N_{TA}}{N_D^{*}L_{GB}}-1\right)\right) \end{aligned} \tag{2. 7}$$

Through this relation the critical doping concentration can be calculated for large grain size numerically. This model is more complex than the Seto's model. However it gives more realistic results when the grain size is large. If (E_F-E_T-E_B)>>KT then the above critical doping (equation 2.7) concentration becomes,

$$N_D^{*} \approx \frac{N_{TA}}{L_{GB}} \tag{2. 8}$$

This is the critical doping concentration of Seto's model. The energy barrier height can be calculated in both cases as,

a) Case $N_D < N_D^*$:

The whole crystallite is fully depleted of free carrier, thus $X = L_{GB}$ and the energy barrier height is,

$$E_B = \left(\frac{q^2 2N_D}{8\varepsilon_s \varepsilon_o} \right) L_{GB}^{\ 2} \tag{2. 9}$$

Which is similar to seto's model.

b) Case $N_D > N_D^*$:

The crystallite is partially depleted and the barrier height can be calculated as follows:

$$E_B = \left(\frac{q^2 N_D}{8\varepsilon_s \varepsilon_o} \right) X^2$$

$$\begin{aligned} &\frac{N_{TA}}{XN_D} = 1 + e^{\left(\frac{E_T - E_F + E_B}{kT} \right)} \\ &\Rightarrow\ E_B = \left(E_F - E_T + kT \ln \left(\frac{qN_{TA}}{\sqrt{8\varepsilon_s \varepsilon_o N_D E_B}} - 1 \right) \right) \end{aligned} \tag{2. 10}$$

If $(E_F - E_T - E_B) >> KT$ then the energy barrier height, E_B becomes,

$$E_B = \left(\frac{q^2}{8\varepsilon_s \varepsilon_o} \right) \frac{N_{TA}^2}{N_D} \tag{2. 11}$$

This is same as Seto's model. From the above correction, the barrier height can be plotted as function of the doping concentration with the grain size as shown in Figure 3. 3.

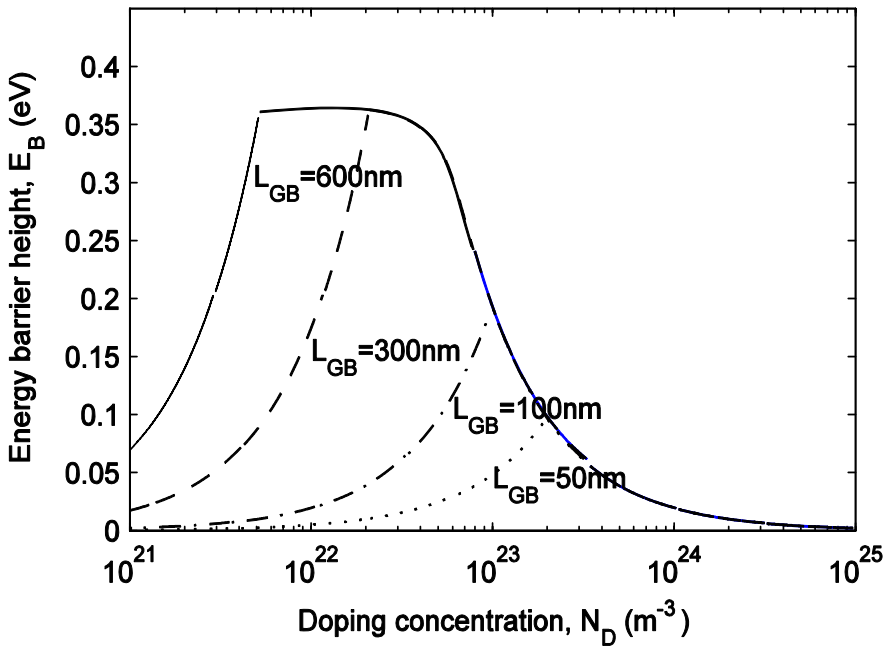

Figure 2.6 Dependence of the energy barrier (improvement of seto's model) as a function of doping concentration in polysilicon material, N_{TA}=1×10^{16}m^{-2}, E_T is located at midgap.

2.2.3 Grain Boundary Model with Applied Biasing

The electronic charge trapped in the grain boundary act as a repulsive force for majority carriers (for electron in case of n-type materials) crossing the interface. In the energy band diagram of the polycrystalline material, this represents by the band banding, $\Phi(x)$ in Figure 2.7. If a bias voltage (V) is applied across the material, the energy levels tilt until breakdown occurs [59]. Blatter *et al.* has developed a model to determine the effect of bias voltage on the potential barrier height, Φ_B [40], [60]. To develop the model, the poison's equation is solved for the potential $\Phi(x)$ and Charge distribution $\rho(x)$ as follows:

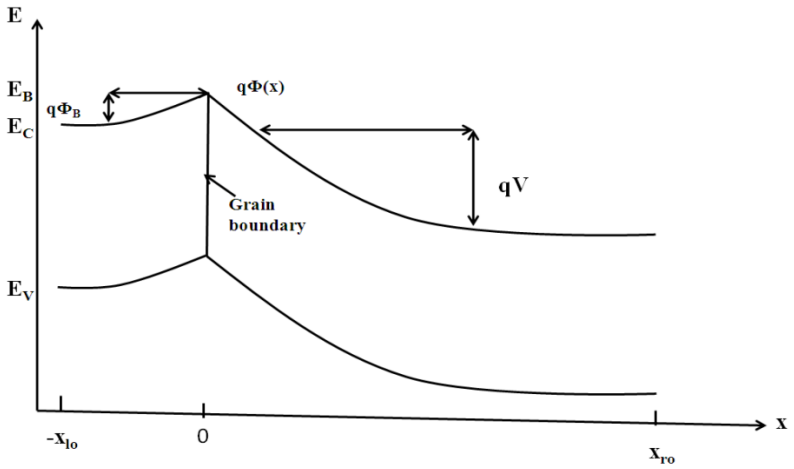

Figure 2.7 Energy-band diagram of polycrystalline material under bias voltage, V.

$$\frac{d^2}{dx^2}\left(\Phi(x)\right)=\frac{\rho(x)}{\varepsilon_o\varepsilon_s} \tag{2. 12}$$

Where, $\rho(x)=qN_D[\Theta(x+x_{lo})-\Theta(x-x_{ro})]-N_{TA}\delta(x)$, Θ (x)= Heaviside step function, δ(x)= delta function.

By using boundary conditions

$$\Phi(-\infty)=\Phi(-x_{lo})=0;\quad \Phi(\infty)=\Phi(x_{ro})=-V$$

$$\Phi(O^-)=\Phi(0^+)=\Phi_B;\quad \Phi(O^-)-\Phi(0^+)=-\left(\frac{qN_{TA}}{\varepsilon_s\varepsilon_o}\right)$$

The barrier height Φ_B is calculated in terms of applied bias, V and the interface charge qN_{TA},

$$\Phi_B=\frac{V_C}{4}\left(1-\frac{V}{V_C}\right)^2 \tag{2. 13 }$$

Where, $V_C=\dfrac{\varepsilon_s\varepsilon_o}{2qN_D}\left(\dfrac{qN_{TA}}{\varepsilon_s\varepsilon_o}\right)^2$.

Therefore this potential barrier height explains the behavior same as Seto's model (for $N_D > N_D^*$ region i.e. for high doping substance) [39]. However this model includes the applied bias effect at heavily doped polycrystalline material. Here, it seems that the barrier height decreases with the applied voltage (within the break down voltage). The behavior of barrier height with the bias voltage cannot be expressed in case of low doping ($N_D < N_D^*$) as they consider it only for high doping substance.

2.2.4 Joshi's Grain Boundary Model

The Grain boundaries in polycrystalline material are found to act as (i) potential barrier for majority carriers which impedes the transport of carriers from one crystallites to the other and thus effect their mobility, (ii) these also act as a recombination surface between the trapped majority carriers and photogenerated minority carriers [61]. These effects of recombination and potential barrier become more complicated when the devices are subject to optical illumination. Therefore the electrical transport properties are governed by the traps at the grain boundaries. When a polycrystalline material is illuminated, the minority carriers move towards the grain boundary surface in an attempt to pass the grain boundary interface due to the high electric field of space charge layer. These minority carriers (holes for n-type materials) are then attracted by the trapped majority carriers (electrons in n-type materials) in the grain boundary surface and thus recombine with them. Therefore, electric field of space charge layer enhances the recombination of excess minority carriers with the trapped majority carriers. This recombination process leads to a lowering of the carrier concentrations in grain boundary region and a new

interface charge is established at the GB interface through Shockley-Read-Hall capture and emission processes [62]. This results a reduction of space charge potential barrier from its dark value and Fermi level, E_F splits into electron quasi-Fermi level, E_{Fn}, hole quasi-Fermi level, E_{Fp}. Optical illuminations disturb the charge neutrality between the GB and the two depletion regions of either side of the GB [61]. Therefore, the GB trap states distribution are modified and the minority carrier quasi-Fermi level (E_{Fp}) does not remain flat throughout the entire depletion region.

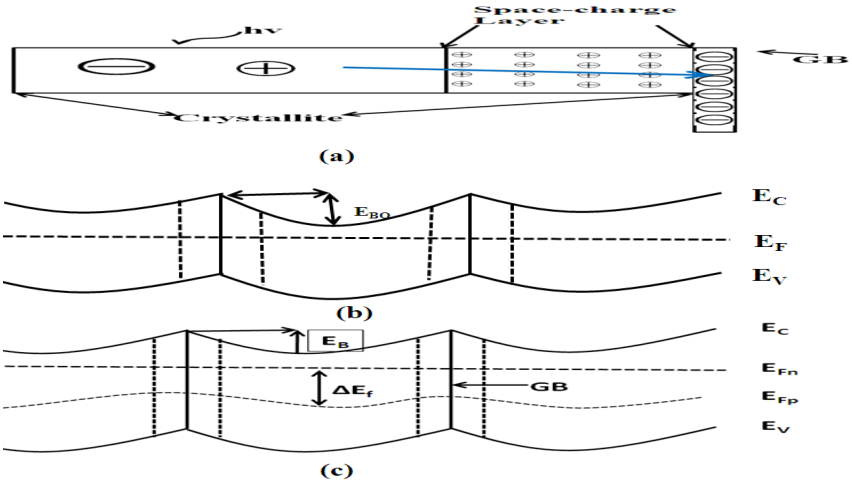

Figure 2.8 (a) Optically generated minority carrier (holes for n-type materials) with trapped majority carriers in grain boundary of polycrystalline material, (b) Energy band diagram in the dark (n-type polycrystalline material), (c) Energy band diagram under optical illumination (n-type polycrystalline material).

Several works has been carried out on grain boundary recombination process in polycrystalline materials [63], [64], [65], [66]. Card *et al.* has been first studied theoretically the grain boundaries recombination processes [63], based on the assumptions of equal capture cross-sections of grain boundary states for electrons and

holes. Moreover, they assumes that quasi-Fermi level of minority carriers are nearly flat in the grain boundary space charge region, however this assumptions hold true at low grain boundary energy barrier [64]-[66]. Therefore Panayotatos *et al.* have presented a theoretical model of grain boundary recombination by considering unequal capture cross-sections for majority and minority carriers [64]. But they have neglected the emission process from the grain boundary states, which may be critical in case of large potential barrier height samples [67]. Seager has proposed a theoretical model of grain boundary recombination under optical illumination [65]-[66]. His analysis is based on uniform illumination of grain boundaries and pinning of the dark Fermi level at the mono-energetic level of GB states which is valid for low doping concentrations. He also assumes that under low injection level the majority carrier transport from quasi-neutral crystallite to the grain boundary surface occurs via thermionic emission. However practically the illumination levels are non-uniform and the barrier height is quite low at high illumination level, therefore the process of thermionic emission is not solely responsible for the transport of majority carriers. Joshi *et al.* has presented a comprehensive theory of grain boundary recombination under optical illumination by considering both δ-function and Gaussian energy distribution of grain boundary states along with the Shockley-Read-Hall (S-R-H) recombination statistics [62], [67]-[68]. They have also considered that the effect of grain boundary is not only confined in the GB depletion regions but also in the neutral and quasi-neutral regions of the adjacent grains. The assumptions of the model are,

a) Polycrystalline material is composed of identical crystallites with an average grain size, L_{GB} unit.

b) The grain boundary width is much smaller than L_{GB}.

c) The grain boundary space charge layer width is (X_{lo}+X_{ro}=X) small compared to L_{GB} and this region is depleted of free carriers [64]–[67]. This assumption is valid under both low and high illumination. The space charge layer, X will be negligible as compared to L_{GB} under high illumination level.

d) Under sufficient illumination condition, the grain boundary recombination current density will be predominant over the space charge recombination current density. Therefore, space charge recombination current can be negligible [66]-[67].

e) The photo generated electrons and holes are uniform throughout the sample [66]-[67]. However in thick sample the uniform photo generation of minority carriers cannot be maintained.

f) Capture cross sections of grain boundary states are equal. There are two carrier capture cross sections of different magnitude for the recombination process [64]: (i) capture cross sections for the capture by a neutral center (σ_N), (ii) cross sections for the capture by a coulombic center (σ_C). So for n-type material if σ_p= hole capture cross section, σ_n =electron capture cross section, then $\sigma_{p=}$ σ_C and σ_n= $\sigma_{N.}$

g) The quasi-Fermi level of the majority carriers E_{Fn} is flat everywhere and the quasi-Fermi level of the minority carriers E_{Fp} is varied with distance under sufficient illumination.

h) The dark hole concentration is negligible under sufficient illumination [67].

By considering above assumptions Joshi *et al.* have developed a model for highly doped polycrystalline semiconductor to investigate the effects of grain size, illumination level,

and the bulk diffusion length of minority carriers on the grain boundary potential barrier height as[67],

$$\sqrt{\left(8\varepsilon_s\varepsilon_o N_D\phi_B\right)} = qN_{TA}\left(\sigma_N N_D e^{\left(\frac{-q\phi_B}{kT}\right)}+\sigma_C n_i\beta^{-1}\right)\left\{\left(\sigma_N N_D e^{\left(\frac{-q\phi_B}{kT}\right)}+\sigma_C n_i\beta\right)+\sigma_N n_i\beta+\sigma_C\left(\frac{n_i^{\,2}}{N_D}\right)e^{\left(\frac{q\phi_B}{kT}\right)}e^{\left(\frac{\Delta E_F}{kT}\right)}\right\}^{-1} \quad (2.\ 14)$$

Where, ΔE_F= quasi Fermi level separation [67]. At very low illumination levels ($G\approx 0$), ΔE_F is very small and then potential barrier height reduces to,

$$\sqrt{\left(8\varepsilon_s\varepsilon_o N_D\phi_{BO}\right)} = qN_{TA}\left(1+e^{\left(\frac{E_T-E_F+q\phi_{BO}}{kT}\right)}\right)^{-1} \quad (2.\ 15)$$

This gives dark value (without illumination) of the potential barrier height, Φ_{BO} and the same results obtained by Baccarani to calculate potential barrier height [58]. According to Joshi's model potential barrier height, Φ_B depends on the illumination level, G. For both n-type and p-type polysilicon has dark value Φ_{BO} up to a certain illumination level, but after certain value of G, potential barrier height decreases with the increase of illumination level. Their model also shows the dependency of potential barrier height on the bulk diffusion length and the ratio of hole capture cross section to electron capture cross section of the grain boundary recombination centers. The basic influence of grain boundaries on the carrier transport can be expressed by δ-function energy distribution of grain boundary states in a similar manner of Gaussian energy distribution [68]. Joshi's model is valid for high doping levels and for small grain sizes ($L_{GB}\approx 0.1\mu m$ and

$N_D \approx 10^{15}\text{cm}^{-3}$) especially in low illumination condition (large dark potential barrier height) [68].

Several models were developed to explain the effect of grain boundary barrier and its characteristics. However none of them can comprehensively explain the effect of grain boundary under biasing condition for low doping polycrystalline materials when crystallites are fully depleted and charge neutrality may not maintained in the polycrystalline material.

2.3 Mobility and Life-time in Polycrystalline Material

The grain boundary interface in polycrystalline material has an impact on the both mobility and life-time of charge carriers. The mobility in the polycrystalline material is dependent on the two different regions such as high conductivity and low conductivity region. The grain regions of a polycrystalline materials refer as a high conductivity as like crystalline materials. However the mobility in the grain boundary interface degrades due to presence of the potential barrier. Therefore the mobility in the polycrystalline material can be written as [69],

$$\frac{1}{\mu_{Total}} = \frac{1}{\mu_{Grain}} + \frac{1}{\mu_{GB}} \tag{2. 16}$$

Where, μ_{Total}= total mobility in the polycrystalline material, μ_{Grain}= mobility in the grains, μ_{GB}=mobility in the grain boundary interface. Generally $\mu_{Grain} >> \mu_{GB}$, the overall mobility thus depends on the charge carrier transfer through the grain boundary interface. The conductivity of polycrystalline material with a grain size L_{GB} can be written as [39], [70], [71], [72],

$$\sigma_{GB} = \frac{L_{GB} q^2 n}{\sqrt{2\pi mkT}} e\left(-\frac{q\phi_B}{kT}\right) \tag{2. 17}$$

Where σ_{GB}=conductivity in polycrystalline material through grain boundary interface, n= average density of carriers in grain, m= effective mass of the charge carriers, T= temperature, k= Boltzmann constant Φ_B= Charge carrier barrier height at grain boundary. By using the relationship in semiconductors,

$$\sigma_{GB} = qn\mu_{GB} \tag{2. 18}$$

The charge carrier mobility through grain boundary interface can be written as,

$$\begin{aligned} \mu_{GB} &= \frac{L_{GB} q}{\sqrt{2\pi mkT}} e\left(-\frac{q\phi_B}{kT}\right) \\ \Rightarrow \mu_{GB} &= \mu_o e\left(-\frac{q\phi_B}{kT}\right) \end{aligned} \tag{2. 19}$$

Taking into account scattering in both the grain and at the grain boundaries interfaces, the carrier mobility in the polycrystalline material is written as,

$$\mu_{Total}{}^{-1} = \mu_{Grain}{}^{-1} + \mu_o{}^{-1} e\left(\frac{q\phi_B}{kT}\right) \tag{2. 20}$$

Therefore, the mobility in polycrystalline material is thermally activated and depends on the barrier created due to trapped charge at the grain boundary interface.

The life time of charge carriers in polycrystalline materials is also governed by the grain boundary interface as the majority carriers are trapped in the GBs. On illumination, the minority carriers are moved towards the grain boundary surface in an attempt to pass the

grain boundary interface due to the high electric field of the space charge layer. These minority carriers (holes for n-type materials) are then attracted by the trapped majority carriers (electrons in n-type materials) in the grain boundary surface and thus recombine with them. Therefore effective minority carrier life time depends on the grain boundary interface states. Polycrystalline materials are very promising candidate for low-cost solar cells. However the efficiency of polycrystalline solar cells is low compared to the single crystal [73]. The loss of minority carriers in polycrystalline materials (i.e. decrease in life time) is responsible for the decrease in solar cell efficiency [74]. Card *et al.* has reported that the life time of polycrystalline materials decreases with an increasing grain boundary interface states and decreases linearly with a decreasing grain size [63]. The band bending at the grain boundary interface depends on the doping concentration and thus controls the minority carrier recombination rate. Therefore minority carrier life-time also decreases with the increasing doping concentration [63]. However effective life-time of minority carriers can be expressed as [74],

$$\tau_{Effective}^{-1} = \tau_{Bulk}^{-1} + \tau_{GB}^{-1} \qquad (2.\ 21)$$

Where τ_{Bulk}= single crystal life time in bulk, τ_{GB}= Grain boundary life time.

Dimitriadis *et al.* has reported that the effective minority life time $\tau_{effective}$ becomes τ_{GB} for small grain size and $\tau_{effective}$ becomes τ_{Bulk} for large grain size polycrystalline materials [74]. However they determine the grain boundary life time τ_{GB} through their proposed model [74].

CHAPTER 3 ANALYTICAL MODEL

Polycrystalline materials are increasingly used in large-area detectors and solar cells due to their cost-effective, fast and flexible fabrication methods [37], [75]. In these applications, intrinsic or lightly doped polycrystalline semiconductor is used. A polycrystalline material is composed of micro crystallites joined together by grain boundaries (complex structure, consisting of a few atomic layers of disordered atoms). A several crystallographic defects such as dislocations, vacancies, interstitial, dangling bonds, and distorted bond angles can be originated at the grain boundaries. All these irregularities of the inter-atomic bonding at the grain boundaries lead to the formation of electronic states. These electronic states may have energies in the bandgap and these intra band gap states act as a trap centers for carriers. Therefore, grain boundaries can trap a large amount of charges during detector operation. A potential barrier for drifting carriers may exist at the grain boundary, which controls the carrier mobility. Therefore, it is well believed that the properties of grain boundary region control the transport properties of the polycrystalline material.

Polycrystalline detectors have experienced a rather rapid advance in the recent years and extensive research has been carried out to improve the transport properties of the polycrystalline materials [33], [38]. However the performance of these polycrystalline detectors are affected due to the polarization effect under applied bias [11], [32]. The polarization effect is defined as any change in the performance of the detector after the

detector biasing. The polarization effect occurs due to charge trapping and de-trapping at the grain boundary interfaces. One important consequence of the polarization effect is the existence of a zero average electric field region in some portion of the detector under applied bias, which significantly affects the charge collection efficiency of the detectors [11], [32]. The polarization effect pre-dominates when the internal electric field due to charge trapping becomes comparable to the electric field generated by the applied bias [76].

Seto *et al.* has proposed a comprehensive model to explain the transport phenomena in polycrystalline materials by solving the one-dimensional Poisson's equation in the depleted grain region [39]. Seto's model has not considered the finite width of the grain boundary region and the effect of applied bias. Later, Greuter *et al.* has extended the Seto's model by incorporating the effect of applied bias [40]. All the previous models have considered equal amount of charges (with opposite polarity) in the grain boundary and depleted grain regions (i.e., there exists the charge neutrality in the material). However, the grain boundaries can possess more trapped charge compare to the depleted bulk grain in intrinsic or low-doped detectors under light illumination and thus imbalance the charge neutrality. Therefore, none of the previous models is applicable in this case.

This research work presents a general grain boundary model considering an arbitrary amount of grain boundary charge and a finite width of grain boundary region. The present model is applicable for any doping levels of the polycrystalline materials. The one-

dimensional Poisson's equation has been solved in both depleted grain and grain boundary regions. The electric field and potential distributions across the detector is examined under various doping, trapping and applied biases. The model explains the conditions of existence of a potential barrier at the grain boundary and a zero average field region in some portion of the detector. Thus, this model also explains the polarization mechanisms in polycrystalline materials.

3.1 Analytical Model

Let us consider a detector geometry consisting of a polycrystalline photoconductor layer sandwiched between two electrodes and the photoconductor layer has a total m numbers of grain. The detector is biased with a voltage $V_{applied}$ to establish an electric field $E_{applied}$ in the photoconductor to develop analytical model for evaluating electrical properties in polycrystalline detector (Figure 3.1). The following assumptions are taken into account for calculating barrier height as well as electric field of each grain,

a) The single crystalline energy band structure is assumed to be applicable inside the grains.
b) Polycrystalline detector consists of m identical grains depending on doping, trapping at grain boundary interfaces and grain size.
c) Doping concentration (N_d) in polycrystalline material is uniform and all the dopants are ionized.
d) All the grain has same size, L_G.

e) The grain boundary has thickness of d (10 A^0 i.e. few atomics distance). Which is smaller than the length of the grain size L_G (i.e. $d<<L_G$).

f) Only one type of trap is considered in the grain boundary interface which is initially neutral and become charged by trapping carriers. The traps are acceptor in the n-type and donors in the p-type semiconductor.

The detector thickness can be divided into m-segments of equal width. Each segment has a grain boundary region at its center that is sandwiched between two crystalline (grain) regions as shown in Figure 3.1. The voltage drops in various segments are denoted as V_1, V_2, V_3, and so on. The trap carriers at grain boundary deplete free carriers from the doped grains and create a space charge region surrounding the grain boundary. At first, poisson equation will be solved for the first segment to develop the general relation of potential and electric field of a particular segment.

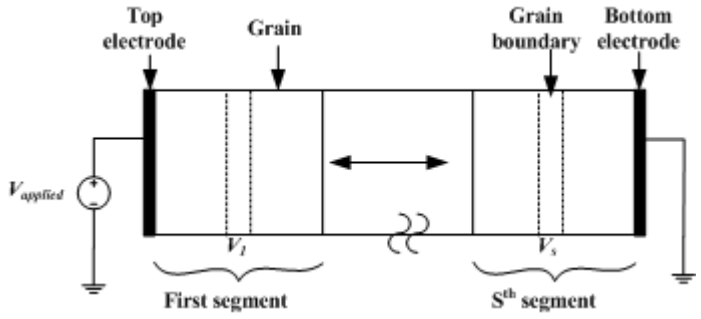

Figure 3.1 Schematic diagram illustrating the grains and segments in polycrystalline detector. Each segment contains a grain boundary surrounded by crystalline grain regions. The total length of the grain region in each segment is equal to the grain size.

The polycrystalline detectors can be classified depending on their doping concentrations as follows:

a) **Highly doped polycrystalline detector**
b) **Lightly doped Polycrystalline detector**

3.2 Electrical Properties in Highly Doped Detector

For high doped polycrystalline materials, the grain is partially depleted. We define high doping case when $N_{ta} < N_d L_G$ and maintains charge neutrality in every segment, where N_{ta} is the trapped electron density (cm^{-2}). Each segment of the detector has both nonzero and zero electric field region. The charge carrier transport model in highly doped semiconductor is governed by the barrier height created due to trapped charge in the grain boundary interface. Let us consider m-segment detector (Figure 3.2), considering the same assumptions were made in section 3.1 along with the following assumptions:

a) Each detector segment is doped highly so that they become partially depleted i.e. $x_l < L_G/2$ and $x_r < L_G/2$.
b) The applied voltage is dropped across the depletion region near the grain boundary and thus the voltage drop across each grain is, $V_S = V_{applied}/m$.
c) The charge neutrality of each segment in between grain boundary and grain is maintained.
d) The depleted grain width within a segment, $W = x_r + x_l - d = N_{ta}/N_d$ ($W < L_G$) (i.e. charge neutrality condition).

The space charge concentration, electric field, and potential distributions in the first segment are schematically shown in Figure 3.2. It is assumed that the doping is n-type and the applied bias is positive. The trapped charge in the grain boundary and the applied voltage control the space charge widths (x_l and x_r) (Figure 3.3).

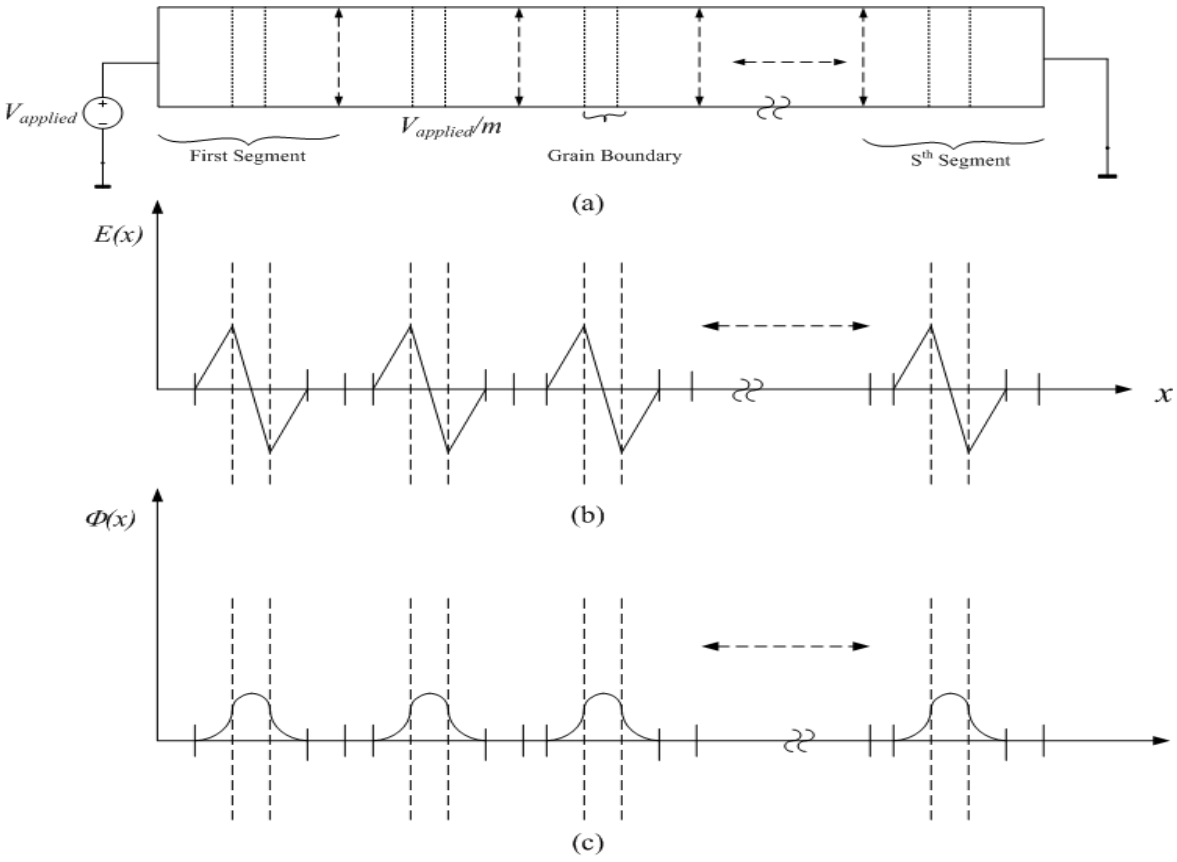

Figure 3.2 Schematic presentation of (a) *m*-segment detector (n-type) under biasing condition, (b) electric field distribution in each segment, (c) potential distribution of the detector segments.

Each segment is divided into three regions considering the grain boundary in the middle of the segment. The three regions are: (a) region-I ($-x_l \le x \le -d/2$), (b) region-II ($-d/2 \le x$

≤ $d/2$), and (c) region-III ($d/2 \le x \le x_r$). The Poisson's equation is solved in three regions separately.

Poisson's equation is,

$$\frac{d^2\Phi(x)}{dx^2} = -\frac{\rho(x)}{\varepsilon} \tag{3. 1}$$

where, $\rho = qN_d$ in regions I & III, and $\rho = q\,N_{ta}/d$ in region II. Here, q is the elementary charge, and ε is the permittivity of the polycrystalline material.

The boundary electric fields are assumed as $E(x_l) = E_S = 0$ and $E(x_r) = E_{S+1} = 0$. The boundary potentials are assumed as $\Phi(x_l) = 0$ and $\Phi(x_r) = -V_1 = -V_{applied}/m$.

Continuity of the electric field gives, $E_I(-d/2) = E_{II}(-d/2)$ and $E_{II}(d/2) = E_{III}(d/2)$. Also, continuity of potentials can be written as, $\Phi_I(-d/2) = \Phi_{II}(-d/2)$ and $\Phi_{II}(d/2) = \Phi_{III}(d/2)$.

By using all these boundary conditions the potential and electric field for all three regions are calculated as follows:

$$\Phi_I(x) = -\left(\frac{qN_d}{2\varepsilon}\right)(x+x_l)^2 - (x+x_l)E_S; \qquad (-x_l \le x \le -d/2) \tag{3. 2 a}$$

$$\Phi_{II}(x) = \left(\frac{qN_{ta}}{2d\varepsilon}\right)(x+d/2)^2 - \left(\frac{qN_d}{\varepsilon}\right)(x_l - d/2)(x+d/2) - \left(\frac{qN_d}{2\varepsilon}\right)(x_l - d/2)^2 - (x+x_l)E_S; \quad (-d/2 \le x \le d/2) \tag{3.2 b}$$

$$\Phi_{III}(x) = -\left(\frac{qN_d}{2\varepsilon}\right)(x-d/2)^2 - \left(\frac{qN_d}{\varepsilon}\right)(x_l - d/2)(x+d/2) - \left(\frac{qN_d}{2\varepsilon}\right)(x_l - d/2)^2 - (x+x_l)E_S + \left(\frac{qxN_{ta}}{\varepsilon}\right); \qquad (d/2 \le x \le x_r) \tag{3.2 c}$$

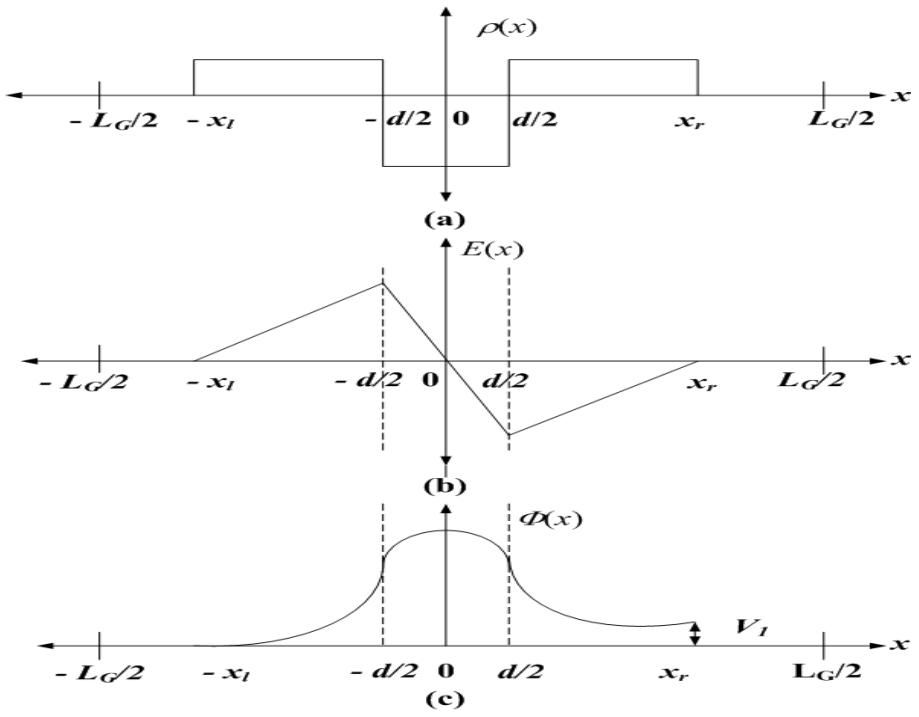

Figure 3.3 Schematic diagram illustrating the space charge concentration, electric field, and potential distributions in any segment of the detector: (a) charge concentration ($\rho(x)$), (b) electric field ($E(x)$), and (c) potential variation ($\Phi(x)$).

And electric field,

$$E_I(x) = \left(\frac{qN_d}{\varepsilon}\right)(x + x_l) + E_S;\ (-x_l \le x \le -d/2) \tag{3. 3 a}$$

$$E_{II}(x) = -\left(\frac{qN_{ta}}{d\varepsilon}\right)(x + d/2) + \left(\frac{qN_d}{\varepsilon}\right)(x_l - d/2) + E_S;\qquad (-d/2 \le x \le d/2) \tag{3.3 b}$$

$$E_{III}(x) = \left(\frac{qN_d}{\varepsilon}\right)(x - d/2) + \left(\frac{qN_d}{\varepsilon}\right)(x_l - d/2) + E_S - \left(\frac{qN_{ta}}{\varepsilon}\right);\qquad (d/2 \le x \le x_r) \tag{3.3 c}$$

By using the assumption in potential for third region,

$$\Phi_{III}(x_r) = -V_1 = - \ V_{applied} / m$$

$$\Rightarrow \Phi_{III}(x_r) = -\left(\frac{qN_d}{2\varepsilon}\right)(x_r - d/2)^2 - \left(\frac{qN_d}{\varepsilon}\right)(x_l - d/2)(x_r + d/2) - \left(\frac{qN_d}{2\varepsilon}\right)(x_l - d/2)^2 + \left(\frac{qN_{ta}x_r}{\varepsilon}\right)$$

$$\Rightarrow -V_{applied} / m = -\left(\frac{qN_d}{2\varepsilon}\right)\left\{(x_l + x_r)^2 - 2x_r\left(d + \frac{N_{ta}}{N_d}\right)\right\}$$

$$\therefore \ x_r = \frac{(W+d)}{2}\left(1 - \frac{V_{applied}}{mV_c}\right) \tag{3. 4}$$

Where, V_C is defined as potential due to doping and trapping in a grain,

$$V_C = \frac{qN_d}{2\varepsilon}\left(N_{ta}N_d^{-1} + d\right)^2 \tag{3. 5}$$

We have,

$$\left(x_l - \frac{d}{2}\right) + \left(x_r - \frac{d}{2}\right) = W_h + d$$

$$\Rightarrow x_l = \frac{(W+d)}{2}\left(1 + \frac{V_{applied}}{mV_c}\right) \tag{3. 6}$$

Therefore space charge region of highly doped detector in each grain is varied with the applied bias and thus alter the barrier height for electron (n-type).

3.3 Critical Doping Concentration

The space charge region (source of barrier height) of the grain is controlled by the trapped charge density in grain boundary interface (N_{ta} m^{-2}), doping concentration (N_d m^{-3}) of the material and applied bias ($V_{applied}$). However for a particular trapped charge density and operating condition the space charge region depends on the doping. Critical doping is defined as a doping concentration above which a particular grain of the detector is partially depleted ($x_l + x_r < L_G$) (Figure 3.4).

In high doping we have,

$$x_l = \frac{(W+d)}{2}\left(1+\frac{V_{applied}}{mV_C}\right)$$
$$x_r = \frac{(W+d)}{2}\left(1-\frac{V_{applied}}{mV_C}\right)$$
$$V_C = \frac{qN_d}{2\varepsilon}\left(N_{ta}N_d^{-1}+d\right)^2$$

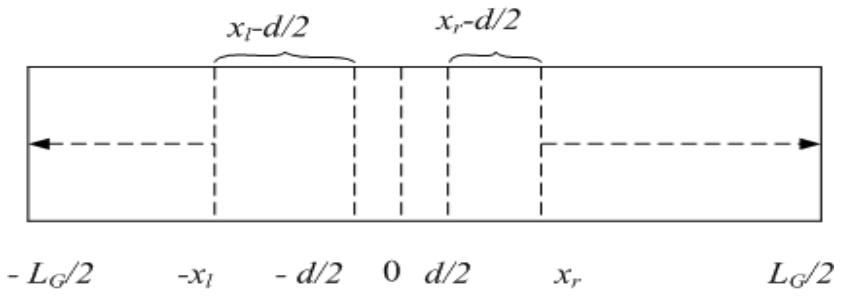

Figure 3.4 Partially depleted grain of a detector. The particular grain is required to be doped above a critical limit to be partially depleted.

$$x_l + x_r \le L_G$$
$$\Rightarrow \frac{(W+d)}{2}\left(1+\frac{V_{applied}}{mV_c}\right)+\frac{(W+d)}{2}\left(1-\frac{V_{applied}}{mV_c}\right) \le L_G$$
$$\Rightarrow (W+d) \le L_G$$
$$\Rightarrow \frac{N_{ta}}{N_d} \le L_G$$

$$\therefore N_d^{*} \ge \frac{N_{ta}}{L_G} \qquad (3.7)$$

Therefore the critical doping concentration is independent of the applied bias as like Seto's model, though the length of space region's are altered and unequal (x_r and x_l) with the applied bias. For example, if we take relative permittivity ε_r=8.3, no. of detector segments m=30, grain size L_G=10μm, trapped charge density N_{ta}=2×10^{15}m^{-2} then critical

doping for the current combination is about N_d^* =2×10^{20} m^{-3}= 2×10^{14} cm^{-3}. Thus, a particular grain is partially depleted if it is doped higher than N_d^*.

3.4 Barrier Height Calculation at High Doping

The barrier height of *m*-segment high doped polycrystalline detector is necessary to determine the charge transport phenomena in highly doped polycrystalline materials. Here, the detector is partially depleted (due to high doping) and a positive voltage is applied to the detector as follows:

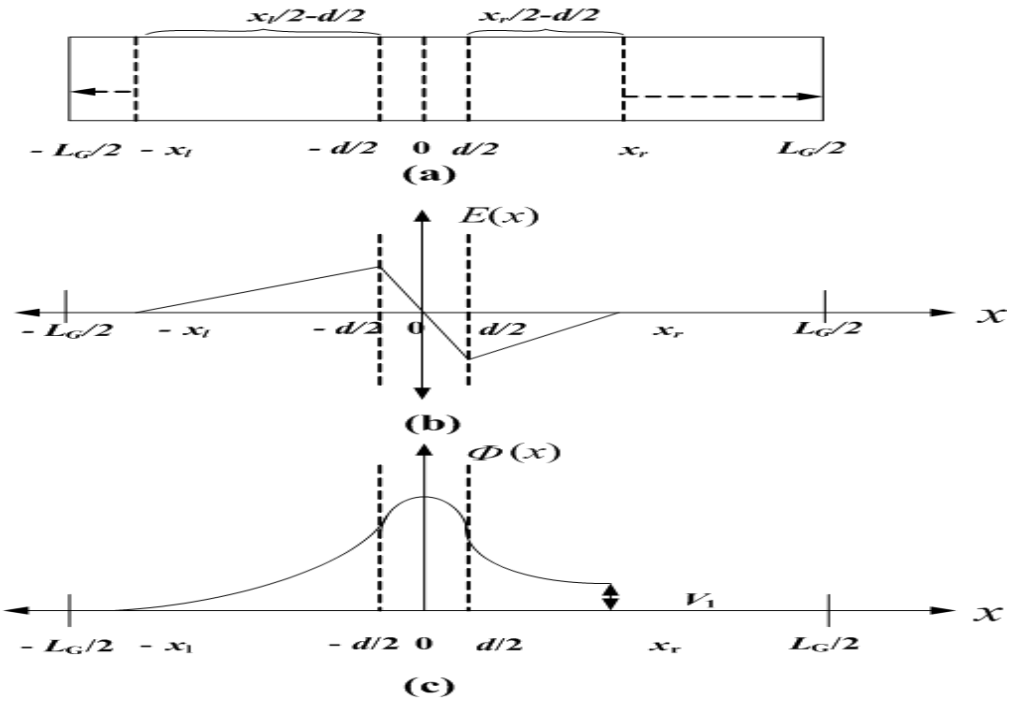

Figure 3.5 Barrier height calculation of highly doped *m*-segment polycrystalline detector, (a) single grain of the detector, (b)electric field distribution of the grain, (c) potential distribution of the grain.

The barrier Height can be expressed as,

$$E_B = -q\left[\Phi_{SII}(0) - \Phi_{SIII}(x_r)\right]$$

$$\Rightarrow E_B = -q\begin{bmatrix} \frac{qN_{ta}}{2\varepsilon d}\frac{d^2}{4} - \frac{qN_d}{\varepsilon}\left(x_l - \frac{d}{2}\right)\frac{d}{2} - \frac{qN_d}{2\varepsilon}\left(x_l - \frac{d}{2}\right)^2 - 0 \\ + \frac{qN_d}{2\varepsilon}\left(x_r - \frac{d}{2}\right)^2 + \frac{qN_d}{\varepsilon}\left(x_l - \frac{d}{2}\right)\left(x_r + \frac{d}{2}\right) + 0 \\ + \frac{qN_d}{2\varepsilon}\left(x_l - \frac{d}{2}\right)^2 - \frac{qN_{ta}}{\varepsilon}x_r \end{bmatrix}$$

$$\Rightarrow E_B = -\frac{q^2 N_d}{2\varepsilon}\left[\frac{N_{ta}}{N_d}\frac{d}{4} - \frac{N_{ta}}{N_d}2x_r + \left(x_l - \frac{d}{2}\right)2x_r + \left(x_r - \frac{d}{2}\right)^2\right]$$

We have,

$$x_l = \frac{(W+d)}{2}\left(1 + \frac{V_{applied}}{mV_C}\right)$$

$$x_l - \frac{d}{2} = \frac{N_{ta}}{2N_d}\left(1 + \frac{V_{applied}}{mV_C}\right) + \frac{d}{2}\frac{V_{applied}}{mV_C};$$

$$x_r = \frac{(W+d)}{2}\left(1 - \frac{V_{applied}}{mV_C}\right)$$

$$x_r - \frac{d}{2} = \frac{N_{ta}}{2N_d}\left(1 - \frac{V_{applied}}{mV_C}\right) - \frac{d}{2}\frac{V_{applied}}{mV_C};$$

Where,

$$V_C = \frac{qN_d}{2\varepsilon}\left(N_{ta}N_d^{-1} + d\right)^2$$

By simplifying the above equation we get,

$$E_B = \frac{q}{4}\frac{qN_d}{2\varepsilon}\left(\frac{N_{ta}}{N_d} + d\right)^2\left\{\left(1 - \frac{V_{applied}}{mV_C}\right)^2 - d\left(\frac{N_{ta}}{N_d} + d\right)^{-1}\right\}$$

$$\Rightarrow E_B = q\frac{V_C}{4}\left\{\left(1 - \frac{V_{applied}}{mV_C}\right)^2 - d\left(\frac{N_{ta}}{N_D} + d\right)^{-1}\right\} \quad (3.8)$$

Therefore, for particular high doped polycrystalline detector if the applied bias is increased (within the detectors' breakdown limit and practical limit of dark current) the barrier height of a particular grain will decrease and it is same for each grain.

3.5 Electrical Properties in Lightly Doped Detector

For intrinsic or low doped polycrystalline materials, the grain can easily be fully depleted even for a small amount of charges in the grain boundaries. Therefore, grain boundaries can possess more trapped charge compare to the depleted bulk grain in intrinsic or low-doped detectors under light illumination. We define low doping case when $N_{ta} \geq N_d L_G$. In this case, the segments can be defined such that $x_l = x_r = L_G/2$, where $L_G >> d$. Figure 3.6 illustrates the model of charge concentration, electric field and potential for a single segment (First one) of the detector (n-type).

Each segment is divided into three regions considering the grain boundary in the middle of the segment. The three regions are: (a) region-I ($-x_l \leq x \leq -d/2$), (b) region-II ($-d/2 \leq x \leq d/2$), and (c) region-III ($d/2 \leq x \leq x_r$). The Poisson's equation is solved in three regions separately.

Poisson's equation is,

$$\frac{d^2\Phi(x)}{dx^2} = -\frac{\rho(x)}{\varepsilon}, \tag{3. 9}$$

where, $\rho = qN_d$ in regions I & III, and $\rho = q\ N_{ta}/d$ in region II. Here, q is the elementary charge, and ε is the permittivity of the polycrystalline material.

The boundary electric fields are assumed as $E(x_l) = E_S$ and $E(x_r) = E_{S+1}$, where S = 1, 2, …..m. The boundary potentials are assumed as $\Phi(x_l) = 0$ and $\Phi(x_r) = -V_s$. However, the expressions for E_S, and V_S are determined later in this research work.

Continuity of the electric field gives, $E_I(-d/2) = E_{II}(-d/2)$ and $E_{II}(d/2) = E_{III}(d/2)$. Also, continuity of potentials can be written as, $\Phi_I(-d/2) = \Phi_{II}(-d/2)$ and $\Phi_{II}(d/2) = \Phi_{III}(d/2)$.

By using the boundary conditions, the potential and electric field for all three regions are expressed as follows:

$$\Phi_I(x) = -\left(\frac{qN_d}{2\varepsilon}\right)(x+x_l)^2 - (x+x_l)E_S; \qquad (-x_l \le x \le -d/2) \tag{3. 10 a}$$

$$\Phi_{II}(x) = \left(\frac{qN_{ta}}{2d\varepsilon}\right)(x+d/2)^2 - \left(\frac{qN_d}{\varepsilon}\right)(x_l - d/2)(x+d/2) - \left(\frac{qN_d}{2\varepsilon}\right)(x_l - d/2)^2 - (x+x_l)E_S; \quad (-d/2 \le x \le d/2) \tag{3.10 b}$$

$$\Phi_{III}(x) = -\left(\frac{qN_d}{2\varepsilon}\right)(x-d/2)^2 - \left(\frac{qN_d}{\varepsilon}\right)(x_l - d/2)(x+d/2) - \left(\frac{qN_d}{2\varepsilon}\right)(x_l - d/2)^2 - (x+x_l)E_S + \left(\frac{qxN_{ta}}{\varepsilon}\right); \qquad (d/2 \le x \le x_r) \tag{3.10 c}$$

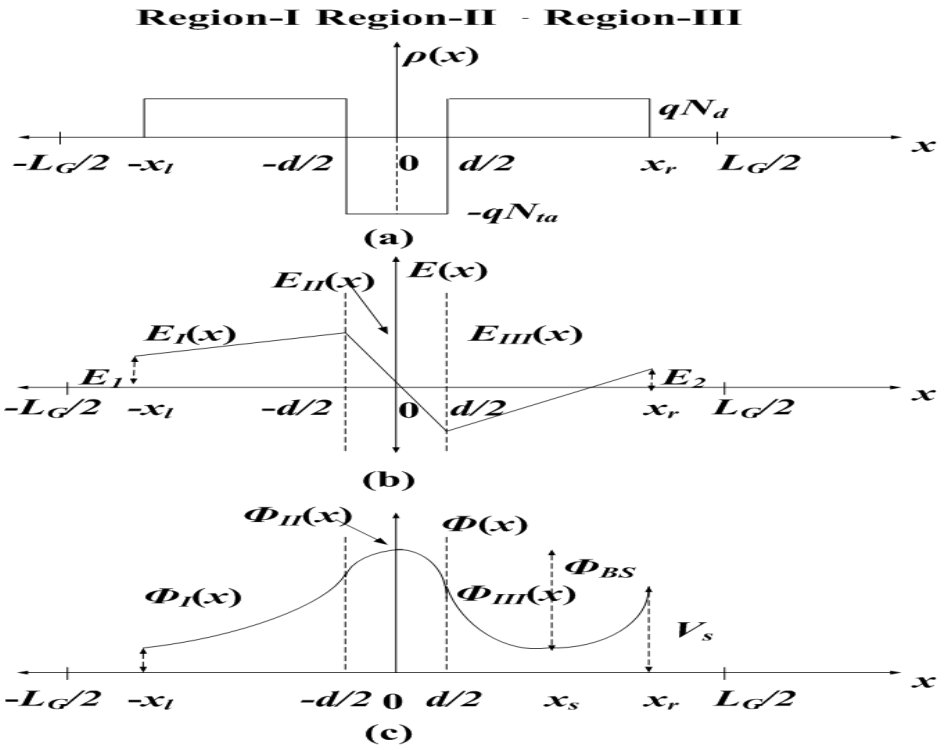

Figure 3.6 Schematic diagram illustrating the space charge concentration, electric field, and potential distributions in the first segment of a low doped detector: (a) charge concentration (ρ), (b) electric field ($E(x)$), and (c) potential variation ($\Phi(x)$).

And electric field,

$$E_I(x) = \left(\frac{qN_d}{\varepsilon}\right)(x + x_l) + E_S\,;\ (-x_l \le x \le -d/2) \tag{3. 11a}$$

$$E_{II}(x) = -\left(\frac{qN_{ta}}{d\varepsilon}\right)(x + d/2) + \left(\frac{qN_d}{\varepsilon}\right)(x_l - d/2) + E_S\,; \qquad (-d/2 \le x \le d/2) \tag{3.11b}$$

$$E_{III}(x) = \left(\frac{qN_d}{\varepsilon}\right)(x - d/2) + \left(\frac{qN_d}{\varepsilon}\right)(x_l - d/2) + E_S - \left(\frac{qN_{ta}}{\varepsilon}\right);(d/2 \le x \le x_r) \tag{3.11c}$$

Let us consider for the first segment,

$$-\frac{d\Phi_{III}(x_r)}{dx} = E_2$$

It is found that,

$$E_2 - E_1 = \left(\frac{qN_d}{\varepsilon}\right)W - \left(\frac{qN_{ta}}{\varepsilon}\right)$$

Where Space charge width, W= (x_l-d/2) + (x_r-d/2).

According to the assumptions if we continue same calculation for the second segment we will find,

$$E_3 - E_2 = \left(\frac{qN_d}{\varepsilon}\right)W - \left(\frac{qN_{ta}}{\varepsilon}\right)$$

$$\Rightarrow E_3 = E_1 + (3-1)\left(\frac{qN_d}{\varepsilon}\right)W - (3-1)\left(\frac{qN_{ta}}{\varepsilon}\right)$$

Therefore, general equation of electric field for S^{th} Boundary (Figure 4.1),

$$E_S = E_1 + (S-1)\left(\frac{qN_d}{\varepsilon}\right)W - (S-1)\left(\frac{qN_{ta}}{\varepsilon}\right) \qquad (3.12)$$

Therefore all the boundary Electric field value can be expressed in terms of first boundary value E_1. The value of E_1 can be obtained by using in two different conditions:

The value of E_1 can be determined as follows,

The value of first boundary electric field value (fully depleted case) can be determined by using,

$$\Phi_{III}(x_r) = -V_1$$

Then we find the voltage difference between two boundaries of the first segments,

$$V_1 = E_1 L_G + \left(\frac{qN_d}{2\varepsilon}\right) L_G^2 - \left(\frac{qN_{ta}}{2\varepsilon}\right) L_G$$

Thus we can find that,

$$V_2 = E_2 L_G + \left(\frac{qN_d}{2\varepsilon}\right) L_G^2 - \left(\frac{qN_{ta}}{2\varepsilon}\right) L_G$$

$$\Rightarrow V_2 = E_1 L_G + (2-1/2)\left(\frac{qN_d}{\varepsilon}\right) L_G^2 - (2-1/2)\left(\frac{qN_{ta}}{\varepsilon}\right) L_G$$

The general value for S^{th} segment can be written as,

$$V_S = E_1 L_G + (S-1/2)\left(\frac{qN_d}{\varepsilon}\right) L_G^2 - (S-1/2)\left(\frac{qN_{ta}}{\varepsilon}\right) L_G \qquad (3.13)$$

The sum of the voltage drops in all segments is equal to the applied voltage $V_{applied}$,

$$V_{applied} = \sum_{S=1}^{m} V_S$$

Therefore by solving this it is obtained,

$$E_1 = \left(\frac{V_{applied}}{mL_G}\right) - \left(\frac{qN_d}{2\varepsilon}\right)(mL_G) + \left(\frac{mqN_{ta}}{2\varepsilon}\right)$$

The value of E_1 can be evaluated for certain operating condition of the detector. E_1 depends on applied bias $V_{applied}$, no. of segments of the detector, m, doping concentrations, N_d, grain size, L_G and also on the trapping concentrations for particular polycrystalline material. Therefore the boundary electric field and potential for S^{th} position of the detector (Figure 3.7):

$$E_S = E_1 + (S-1)\left(\frac{qN_d}{\varepsilon}\right) W - (S-1)\left(\frac{qN_{ta}}{\varepsilon}\right)$$

$$V_S = E_1 L_G + (S-1/2)\left(\frac{qN_d}{\varepsilon}\right)L_G^2 - (S-1/2)\left(\frac{qN_{ta}}{\varepsilon}\right)L_G$$

Now replacing E_1,

$$E_S = \left(\frac{V_{applied}}{mL_G}\right) - \left(\frac{q}{2\varepsilon}\right)(m+2-2S)\left(N_d L_G - N_{ta}\right) \tag{3. 14}$$

& $$V_S = \left(\frac{V_{applied}}{m}\right) - \left(\frac{q}{2\varepsilon}\right)L_G\left(m+1-2S\right)\left(N_d L_G - N_{ta}\right) \tag{3. 15}$$

Therefore, both boundary electric field and potential of each segment is dependent on the applied bias $V_{applied}$ for a particular polycrystalline detector with grain size of L_G and m no. of segments.

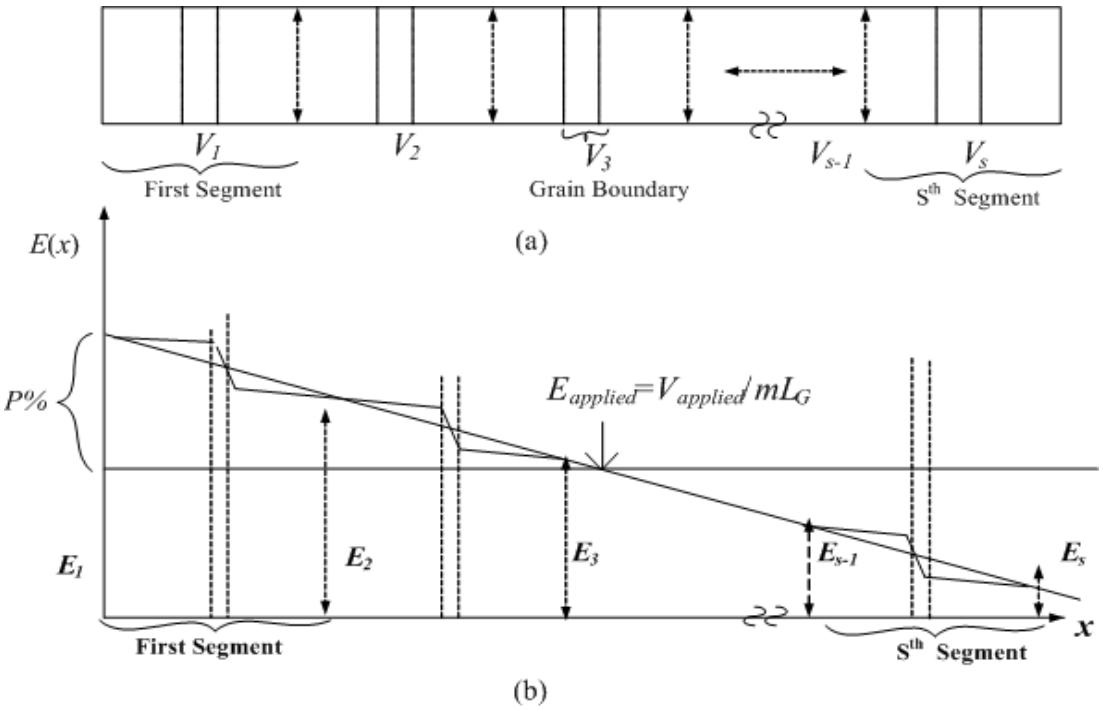

Figure 3.7 Schematic representation of (a) *m*-segment detector with (b)electric field distribution of each segment through the detector.

Boundary electric fields decrease down ward depending on the combination of trapping charge density (N_{ta}) for particular detector in constant operating condition. Later we will see that this electric field orientation control the carrier transport of the detector.

Condition for Intrinsic Doping (N_{di})

The doping concentration of the polycrystalline detector is one of the important factors that control the barrier height for carriers [39]. The intrinsic doping level for the current model has been defined with respect to the average applied electric field ($E_{applied}$= $V_{applied}/mL_G$) at N_{ta}=0.

$$E_1 = \left(\frac{V_{applied}}{mL_G}\right) - \left(\frac{qN_{di}}{2\varepsilon}\right)\left(mL_G\right)$$

$$\Rightarrow E_1 = \left(\frac{V_{applied}}{mL_G}\right)\left(1 - \left(\frac{qN_{di}}{2\varepsilon V_{applied}}\right)\left(mL_G\right)^2\right)$$

$$\Rightarrow \frac{\left|E_{applied} - E_1\right|}{E_{applied}} = \frac{qN_{di}}{2\varepsilon V_{applied}}\left(mL_G\right)^2$$

Here, intrinsic doping concentration (N_{di}) can be defined as the concentration for which the difference between average applied electric field and first boundary electric field is less than *P%* (i.e.1%) of the average applied electric field. Here the value of *P* depends on the polycrystalline material.

$$\frac{\left|E_{applied}-E_1\right|}{E_{applied}} \le \frac{P}{100}$$
$$\Rightarrow N_{di} \le \frac{2\varepsilon V_{applied} P}{100q\left(mL_G\right)^2} \qquad (3.16)$$

For example, if the allowed electric field change P = 1 %, the relative permittivity ε_r=8.3, the total detector thickness L = 300μm, $V_{applied}$=150 V, m= 30, and L_G=10μm, then the intrinsic doping limit $N_{di} \sim 1.5 \times 10^{10}$ cm^{-3}. If the doping is less than N_{di}, the material can be treated as intrinsic.

3.6 Full and Partial-depletion of the Detector Thickness

In Full depletion condition all segments may not experienced the drift movement of the carrier (carrier movement due to the electric field). The number of detector segments those have full electric field varies depending on the operating condition (applied voltage) and also on the trapped charge at the grain boundary. The charge carriers travel rest of the portion of the detector through diffusion. The charge collection efficiency varies with the drift or diffusion movement of the carriers in the detector.

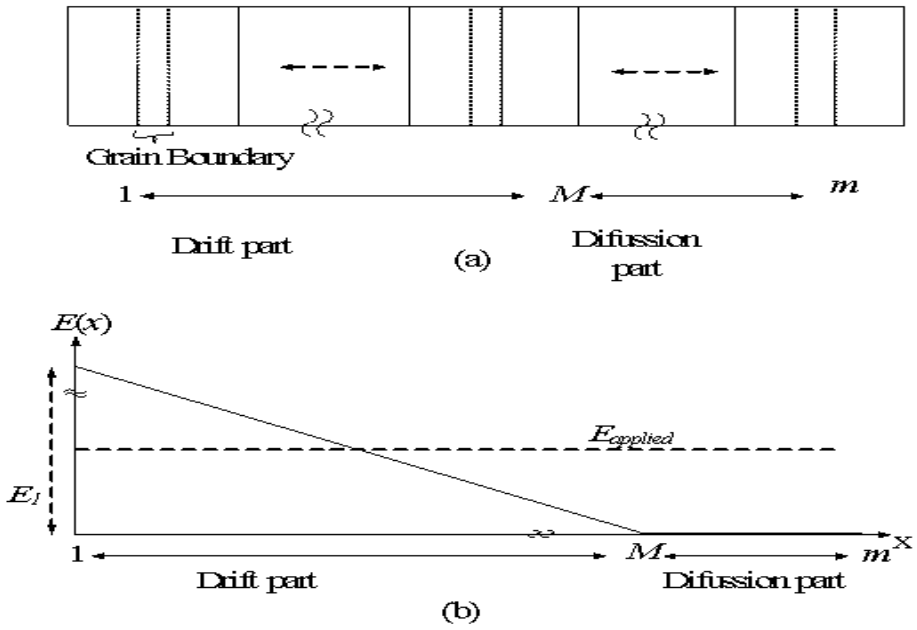

Figure 3.8 (a) Drift and diffusion of the detector of the detector, charge carriers have drift movement up to M^{th} segments and rest of the segments the carriers will move (M^{th} to m^{th}) through diffusion, (b) electric field of the partially depleted detector.

The boundary electric field in the S^{th} position of the detector is given by,

$$E_S = \left(\frac{V_{applied}}{mL_G}\right) - \left(\frac{q}{2\varepsilon}\right)\left(m + 2 - 2S\right)\left(N_d L_G - N_{ta}\right)$$

The detector can be fully depleted for particular operating condition, trapping level at grain boundary, and doping. Under This condition all the segments have positive electric field i.e. carrier will move only through drifting which may improve the charge collection. Let us now calculate the number of segments that are required for a particular detector in particular operating conditions.

In this case all the segments of the multi-segment detector have positive electric field but at the beginning couple of segments have higher boundary electric field than that of applied field ($V_{applied}/mL_G$) and after certain segments boundary electric field will be less than that of applied field. The no. of segments up to which boundary electric field is higher than applied filed is determined by [(m/2)+1] as shown in Figure 3.9 .

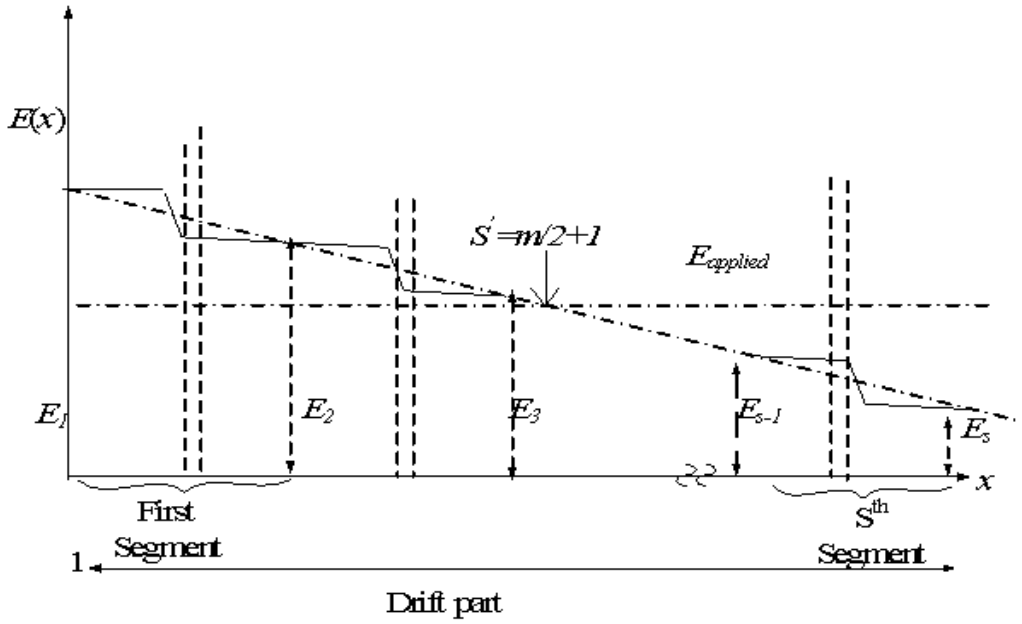

Figure 3.9 Electric field distribution of each segment in multi-segments detector. Here, for $N_{ta}>N_dL_G$, $E_S>V_{applied}/mL_G$ up to $S^{'th}$ segment and after that it decreases depending on the trapping and doping under applied bias.

To find out complete depletion of the detector in the case of $N_{ta}>N_dL_G$, let us take $S=M+1$, $m= M$ where M is last segment of the detector which have drift movement of the carriers (i.e. $E_S\geq 0$).

$$E_S = \left(\frac{V_{applied}}{ML_G}\right) + \left(\frac{q}{2\varepsilon}\right)\left(M + 2 - 2\left(M+1\right)\right)\left(N_{ta} - N_D L_G\right) \geq 0$$

$$\Rightarrow M^2 - \frac{2\varepsilon V_{applied}}{qL_G\left(N_{ta} - N_d L_G\right)} \leq 0$$

$$\therefore M \leq \sqrt{\frac{2\varepsilon V_{applied}}{qL_G\left(N_{ta} - N_d L_G\right)}} \quad ; \qquad M \leq m \tag{3. 17}$$

Therefore for particular operating condition if we consider M segment detector in case of $N_{ta}>N_dL_G$ then full detector will be depleted i.e. the carrier will drift only and there will be no diffusion. Multiplying the above equation by L_G, length of the field region can be written as,

$$L_D = ML_G \leq \sqrt{\frac{2\varepsilon V_{applied}}{q\left(\frac{N_{ta}}{L_G} - N_d\right)}} \tag{3. 18}$$

3.7 Barrier Height Calculation at Low Doping

The barrier height for charge carriers is an important factor to determine charge collection efficiency of the doped polycrystalline detector. The mobility of the charge carrier is altered due to this barrier height. Therefore, it is required to determine the barrier height to improve the performance of the detector. The barrier height for electrons through the low doped polycrystalline detector has been determined by the proposed model.

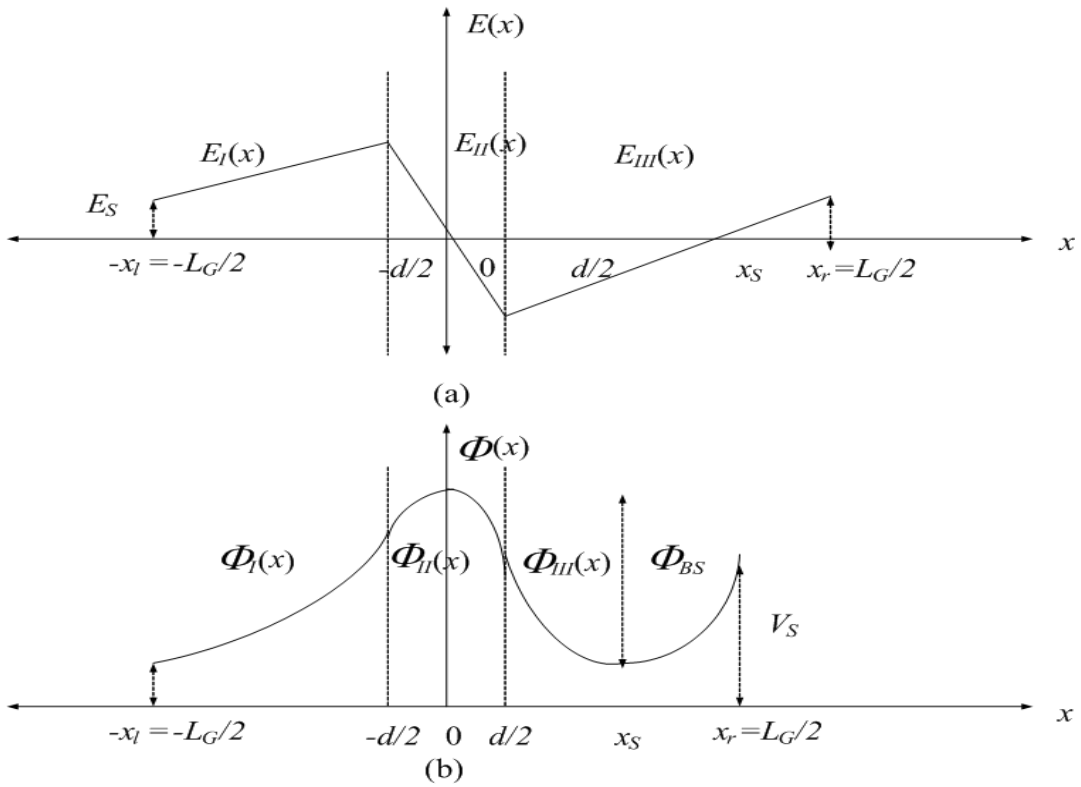

Figure 3.10 Charge carriers' electrical barrier height calculation in low doped polycrystalline detector, (a) electric field in first segment,(b) potential distribution in first segment.

Each segment of the detector has three different regions. A positive voltage, $V_{applied}$ (Figure 3.1) is applied on the *m* segment detector. The electric field has to be negative in order to exist a potential barrier. Therefore, to calculate the barrier height of electron we need to find out the distance x_S at which electric field in third region of a particular segment becomes zero. Now let us determine for first segment (x_1) as,

$$E_{III}(x_1)=\frac{qN_d}{\varepsilon}\left(x_1-\frac{d}{2}\right)+\frac{qN_d}{2\varepsilon}(L_G-d)+\frac{V_{applied}}{mL_G}+\frac{q}{2\varepsilon}m(N_{ta}-N_dL_G)-\frac{qN_{ta}}{\varepsilon}$$

$$\Rightarrow 0=N_d\left(x_1-\frac{d}{2}\right)+N_d(L_G-d)+\frac{\varepsilon V_{applied}}{qmL_G}+\frac{m}{2}(N_{ta}-N_dL_G)-N_{ta}$$

$$\Rightarrow x_1=\frac{L_G}{2}+(m-2)\left(\frac{L_G}{2}-\frac{N_{ta}}{2N_d}\right)-\frac{\varepsilon V_{applied}}{qmL_GN_d}$$

Similarly for S^{th} segment we have,

$$E_{SIII}(x)=\left(\frac{qN_d}{\varepsilon}\right)(x-d/2)+\left(\frac{qN_d}{\varepsilon}\right)(x_l-d/2)+E_S-\left(\frac{qN_{ta}}{\varepsilon}\right);\qquad (\mathrm{d}/2\le \mathrm{x}\le x_r)$$

Therefore at $x=x_S$ we find,

$$x_S=\frac{L_G}{2}+(m-2s)\left(\frac{L_G}{2}-\frac{N_{ta}}{2N_d}\right)-\frac{\varepsilon V_{applied}}{qmL_GN_d} \tag{3. 19}$$

Here, for each individual segments if x_S remains between d/2 and $L_G/2$ ($\frac{d}{2}\le x_S\le\frac{L_G}{2}$) then the barrier height for electrons can be measured through our proposed model. Now let us calculate the barrier height for S^{th} segment can be written as,

$$E_{BS}=-q\left[\Phi_{SII}(0)-\Phi_{SIII}(x_S)\right]$$

$$\Rightarrow E_{BS}=-q\left[\begin{array}{l}\frac{qN_{ta}}{2\varepsilon d}\frac{d^2}{4}-\frac{qN_d}{2\varepsilon}(L_G-d)\frac{d}{2}-\frac{qN_d}{2\varepsilon}\left(\frac{L_G}{2}-\frac{d}{2}\right)^2-\left(0+\frac{L_G}{2}\right)E_S\\ +\frac{qN_d}{2\varepsilon}\left(x_s-\frac{d}{2}\right)^2+\frac{qN_d}{2\varepsilon}(L_G-d)\left(x_S+\frac{d}{2}\right)+\frac{qN_d}{2\varepsilon}\left(\frac{L_G}{2}-\frac{d}{2}\right)^2\\ +\left(x_S+\frac{L_G}{2}\right)E_S-\frac{qN_{ta}}{\varepsilon}x_S\end{array}\right]$$

After solving above equation by replacing x_s and E_s,

$$E_{BS} = \frac{q^2 N_d}{2\varepsilon}\left[x_S^2 - \frac{d}{4}\left(d + \frac{N_{ta}}{dN_d}\right)\right] \tag{3. 20}$$

Therefore the barrier height of a segment can be determined by replacing the value of x_S for a particular operating condition.

By considering the equation 3.8 for high doped polycrystalline material and equation 3.20 for low doped polycrystalline material we can express a general expression as,

$$E_{BI} = \frac{q^2 N_d}{2\varepsilon}\left[x_i^2 - \frac{d}{4}\left(d + \frac{N_{ta}}{dN_d}\right)\right] \tag{3. 21}$$

Where, $x_i = \frac{W_i}{2}\left[1 + (m-2s)\left(1 - \frac{N_{ta}}{N_d W_i}\right) - \frac{2\varepsilon V_{applied}}{qmW_i^2 N_d}\right]$;

$W_i = \begin{cases} L_G & for\ N_{ta} \geq N_d L_G \\ N_{ta}N_d^{-1} + d & for\ N_{ta} < N_d L_G \end{cases}$ and thus we have ,

$$x_i = \begin{cases} x_S & for\ N_{ta} \geq N_d L_G \\ x_r & for\ N_{ta} < N_d L_G \end{cases}$$

Equation 3.21 is the general barrier height representation for polycrystalline material in all doping range.

An analytical model for evaluating the electrical properties (electric field and potential distributions, and energy barrier at the grain boundary) of the polycrystalline detector has been described. The limit of intrinsic doping consideration has also been determined.

CHAPTER 4 RESULTS AND DISCUSSION

The simulation results of our proposed model for polycrystalline grain boundary barrier are presented in this chapter. The objectives of this chapter are to study the variation of electrical properties at:

a) High doped polycrystalline material detector with trapped charge density at grain boundary interface under applied bias condition.
b) Low doped polycrystalline material detector with trapped charge density at grain boundary interface under applied bias condition.
c) Intrinsic polycrystalline material detector with trapped charge density at grain boundary interface under applied bias condition.

Moreover the polarization effect of the low doped or intrinsic doped polycrystalline detector has also been explained briefly.

4.1 Electrical Properties at Highly Doped Detector

The general grain boundary model is applied to polycrystalline materials used in detector applications and examined the electric field distributions and potential barriers at various doping, trapping and biasing conditions. Polycrystalline mercuric iodide is considered as an example whose relative permittivity, ε_r = 8.3. The proposed model evaluates this barrier height by solving Poisson's equation in a particular grain of the detector. At first

we will examine the electric field and potential (Energy band diagram) of the detector segments. And on the basis of this electric field distribution the barrier height of each segment will be calculated. Therefore, we can divide the whole discussion into two parts as,

1) Electric Field and Potential Distribution.
2) Energy Barrier height.

4.2 Electric Field and Potential Distribution at High-doped Detector

Figure 4.1 shows the effect of doping concentration at grain boundary on the electric field distribution of each detector (HgI_2) segments. The grain size is L_G=10μm in m=30 segment detector. Here, trapped charge density is considered as N_{ta}= 1×10^{16} m^{-2}, applied bias is 150 V. The doping concentration is varied from N_d=$8\times10^{21}m^{-3}$, $9\times10^{21}m^{-3,}$ $1\times10^{22}m^{-3}$.The space charge region decreases and peak electric field increases with increasing of doping concentration. However the magnitude of the electric field increases. The energy barrier height of charge carriers (electrons) decrease due to this shrinkage of space charge and thus improve the mobility. Therefore, the charge collection efficiency improves with increasing of doping at high doped regime ($N_{ta}<N_dL_G$) of application.

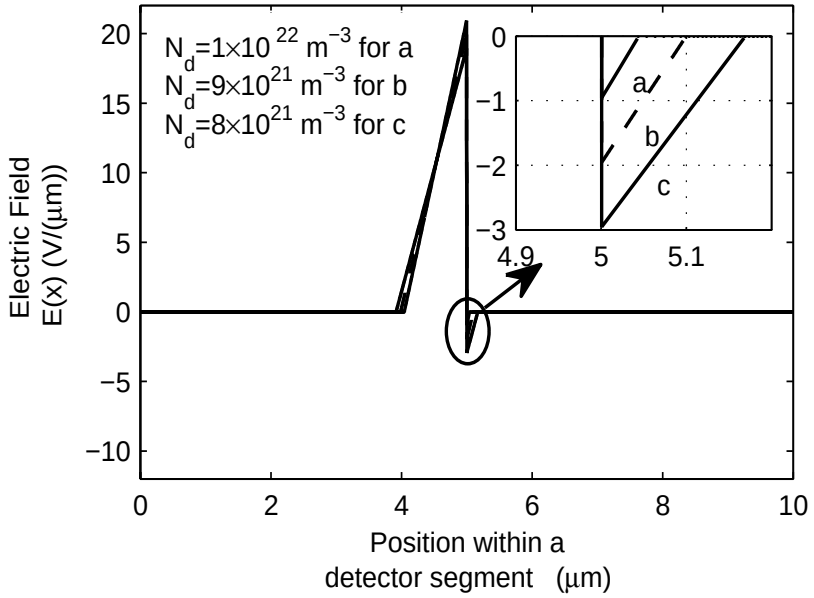

Figure 4.1 Effect of trapped charge density at grain boundary interface on electric field of each detector (HgI_2) segments for different doping concentration at high doped region. Trapped charge density N_{ta}= 1×10^{16} m^{-2}, applied bias $V_{applied}$=150V.

The shrinkage of space charge region with increasing of doping concentration at high doped regime will alter the potential distribution of the detector segments. Figure 4.2 depicts the effect of doping concentration on potential distribution. The doping concentration is varied from N_d=$8\times10^{21}m^{-3}$, $9\times10^{21}m^{-3}$, $1\times10^{22}m^{-3}$. The potential barrier for charge carrier decreases with increasing doping concentration for a fixed trapped charge density. The barrier height decreases in similar manner for all the detector segments at highly doped polycrystalline detector. Therefore, charge carrier (electron) easily overcome this barrier and can travel through the detector. Depending on the detector segments the transit time of the carrier varies. The low barrier height improves the charge collection efficiency.

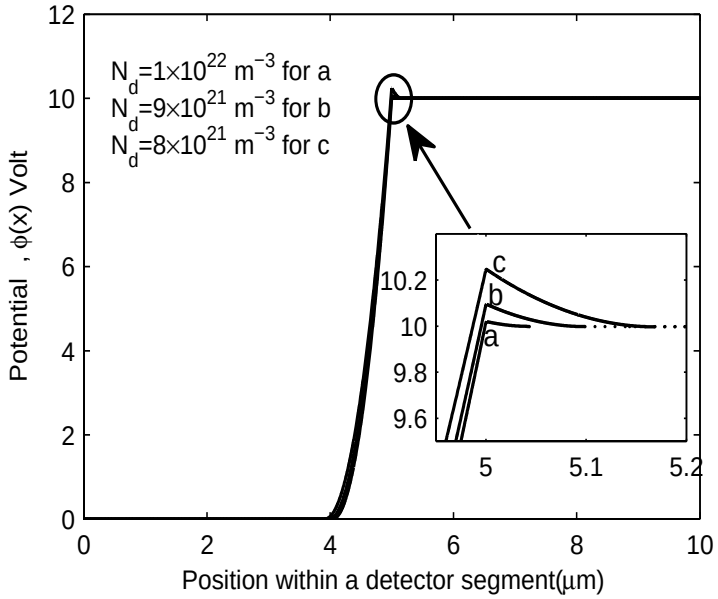

Figure 4.2 Effect of trapped charge density at grain boundary interface on potential of each detector (HgI_2) segment for different doping concentration at high doped region. Here, trapped charge density N_{ta}=1×10^{16}m^{-2}, no. of detector segments m=30.

4.3 Energy Barrier Height at Highly Doped Detector

The energy barrier height of charge carrier (electron) at high doped regional ($N_{ta}<N_dL_G$) is obtained by solving equation (3.8) for a particular detector segment at certain operating condition. Here, the grain size is L_G=10μm, applied bias $V_{applied}$= 150 V and the no. of detector segment m=30. The charge carrier barrier height is same for all the detector segments at high doped regime. Figure 4.3 represents the barrier height E_B versus trapped charge density N_{ta} plot for different doping concentrations. The doping concentration varies as N_d= 7×10^{22} m^{-3}, 8×10^{22} m^{-3}, 9×10^{22}m^{-3}. The space charge electric field increases with increasing of trapped charge density at grain boundary. Therefore, barrier height increases with increasing of trapped charge density for a particular doping concentration

(N_d). However if the doping concentration increases for a fixed trapped charge density, the space charge region decrease and thus lower the energy barrier height of the charge carrier. Thus for a particular operating condition (applied bias) both doping and trapped charge density control the energy barrier height.

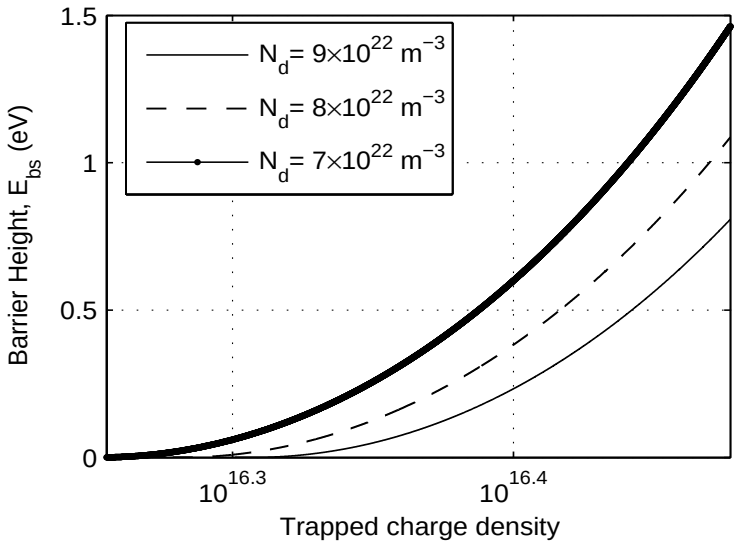

Figure 4.3 Barrier height of each segment E_B versus trapped charge density N_{ta} (m^{-2}) for different doping concentration at applied bias $V_{applied}$= 150 V.

Figure 4.4 represents the effect of biasing voltage on the barrier height. Here, the doping concentration is fixed at N_d=8×10^{22}m^{-3} for m=30 segments detector. The operating bias ($V_{applied}$) varies from 0V, 50V, 150V and 300V. There is negligible barrier height if the trapped charge density is below 1×10^{15} m^{-2}. Barrier height decreases with increasing the operating bias. However increasing $V_{applied}$ also increases the dark current dramatically in most of the detectors. Thus there is a practical limitation on $V_{applied}$.

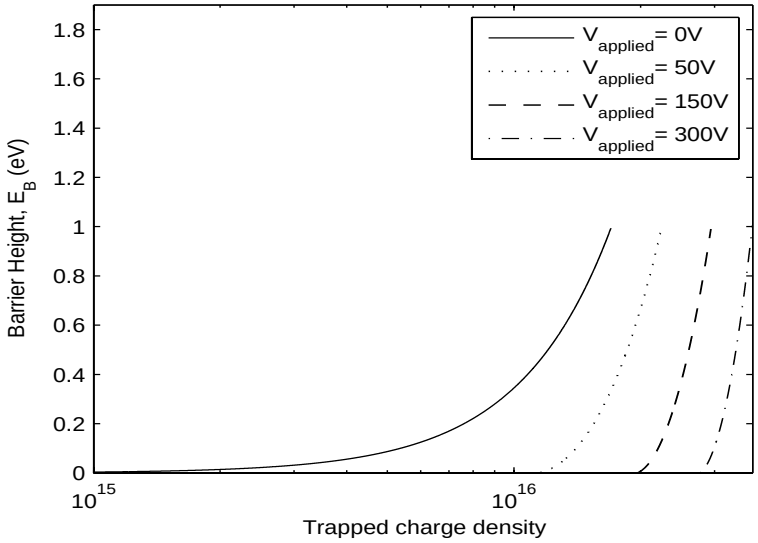

Figure 4.4 Barrier height of each segment E_B versus trapped charge density N_{ta} (m^{-2}) for different operating bias at doping concentration N_d=$8\times10^{22}m^{-3}$.

4.4 Electrical Properties at Low-doped Detector

The proposed grain boundary model is applied to low doped polycrystalline materials used in detector applications and examined the electric field distributions and potential barriers at various doping, trapping and biasing conditions. We consider polycrystalline mercuric iodide as an example whose relative permittivity ε_r = 8.3. The lightly doped polycrystalline semiconductor is defined as $N_{ta}>N_dL_G$ (grain is fully depleted). The trap carriers at grain boundary create a space charge region in doped semiconductors. This space charge region induces electric field, which in turn act as a barrier for charge carrier (electron or hole). Therefore, this induced electric field controls the charge carrier transport through the doped polycrystalline detector. At first the electric field and potential (Energy band diagram) of the detector segments are examined. And on the basis

of this electric field distribution the barrier height of each segment will be calculated. Therefore, we can divide the whole discussion into two parts as follows:

1) Electric Field Distribution.
2) Energy Barrier Height.

4.5 Electric Field at Low-doped Detector

The potential and electric field distributions in each segment are described by the equations (3.10) and (3.11). The boundary electric fields of each detector segment at low doping are determined by the equation (3.14). Figure 4.5 shows the electric field distributions across the detector for various levels of trapped charge density at the grain boundary. The doping concentration is $N_d = 10^{18}$ m^{-3}, $V_{\text{applied}} = 225$ V, $m = 30$, $L_G = 10$ μm, and thus $N_d L_G = 10^{13}$ m^{-2}. The non-uniformity of electric field increases with increasing N_{ta}. There exists a zero-average electric field region for high level of traps at the grain boundary as shown in Figure 4.5. In this case, the detector has two different parts: (i) a high-field drift region and (ii) a zero-average electric field diffusion region. This phenomenon is known as the *polarization effect* [11], [77]. Malm *et al.* also reported the polarization effect and explained the change in electric field distribution in the similar fashion in crystalline CdTe based γ-ray detector [78].This effect is due to the charge trapping and the de-trapping at the grain boundary of the polycrystalline detectors. The space-charge distributions alter with the change of charge trapping at the grain boundary and thus change the electric field profile in the detectors. The polarization effect pre-dominates when the internal electric field due to charge trapping becomes comparable to

the electric field generated by the applied bias [76]. The thickness of the drift region (L_D) can be obtained by equation (3.18). The performance of a detector is mainly determined by the strength of the carrier drift. The reduction of the drift region obviously can reduce the charge collection efficiency and increase the transit time of the detector since the carriers have to move by diffusion in some part of the detector. The higher transit time reduces the response time of the detector. For this particular condition the charge carriers have to travel 50% of the detector through diffusion if the trapped charge density increases up to N_{ta}=1×10^{14}m^{-2} and cause huge degradation of charge transport efficiency. Antonuk *et al.* [37] recently reported that the polarization effect induced by high carrier trapping reduces charge collection efficiency in polycrystalline mercuric iodide detectors. However, the conditions for the existence of a zero-average electric field region also depend on doping concentration and the applied bias.

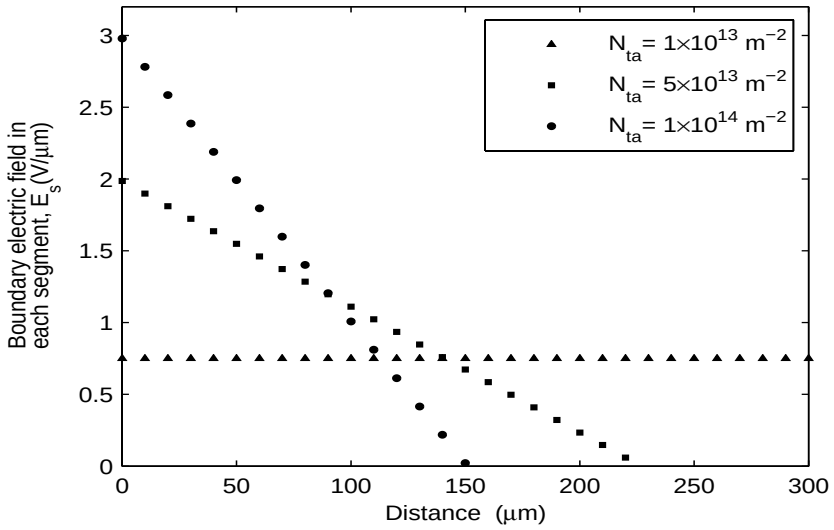

Figure 4.5 Boundary electric field of segments versus distance from the top electrode for various levels of trapped charge densities at the grain boundary. The doping concentration is N_d = 10^{18} m^{-3}, m = 30, L_G = 10 μm, and $V_{applied}$ = 225 V.

Figure 4.6 shows the effects of doping concentration on the electric field distributions across the detector. The applied voltage, $V_{applied}$ = 225 V, m = 30, L_G = 10 μm, and N_{ta} = 10^{14} m^{-2}. For a fixed N_{ta}, the increase of doping concentration reduces the polarization effect. Charge carriers have to travel 50% of the detector through diffusion if the doping concentration is about N_d=1×10^{18} m^{-3}. However if we increase the doping concentration the charge collection efficiency increases with the expansion of the drift region (L_D) and thus improves the performance of the detector.

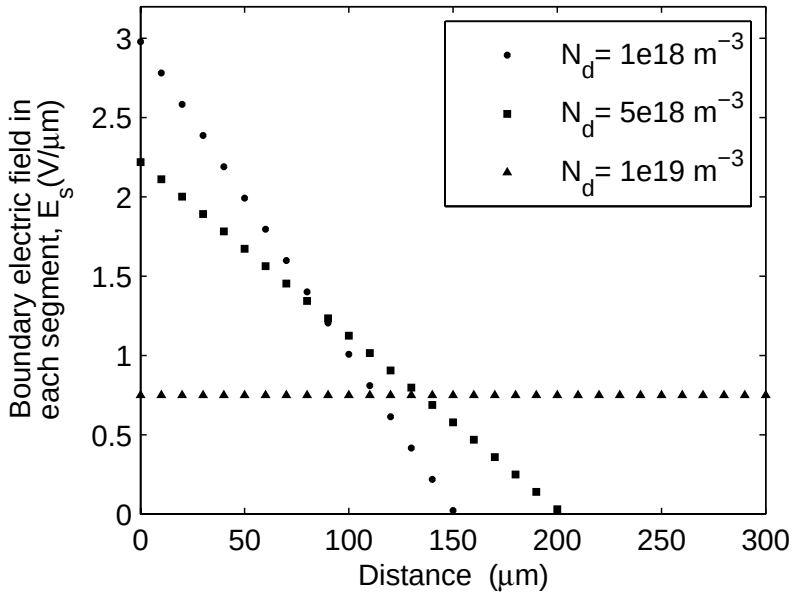

Figure 4.6 Boundary electric field versus distance from the top electrode for various level of doping concentrations. The applied voltage, $V_{applied}$ = 225 V, m = 30, L_G = 10 μm, and N_{ta} = 10^{14} m^{-2}.

Figure 4.7 shows the effects of applied bias on the electric field distributions under fixed doping and trapped charge density at the grain boundary. The doping concentration, N_d = 5×10^{18} m^{-3}, m = 30, L_G = 10 μm, and N_{ta} = 10^{14} m^{-2} are assumed in Figure 4.7. The

drifting region (L_D) increases with increasing applied bias $V_{applied}$ and thus the higher applied bias reduces the polarization effect. However, increasing $V_{applied}$ also increases the dark current dramatically in most of the detectors. Thus there is a practical limitation on $V_{applied}$. The charge carriers drifted throughout the complete detector segments under considered combination if the applied bias increases up to $V_{applied}$=500V.

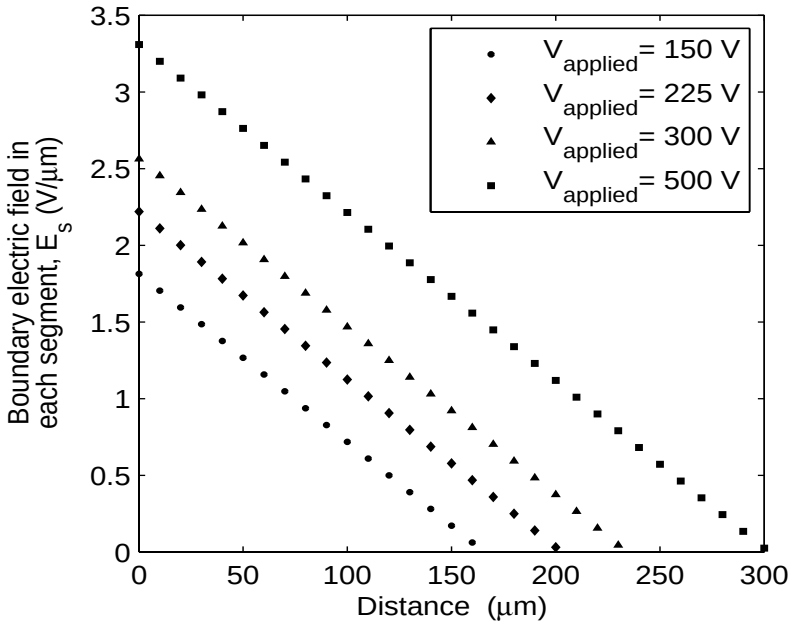

Figure 4.7 Boundary electric field versus distance from the top electrode for different bias voltages. The doping concentration, $N_d = 5 \times 10^{18}$ m^{-3}, $m = 30$, $L_G = 10$ μm, and $N_{ta} = 10^{14}$ m^{-2}. The no. of drifting segments increase with biasing.

The boundary electric field of each detector segment does not depend on the grain size (L_G) if the total trap charge concentration at grain boundary remains constant. The effect of grain size under particular operating condition is obtained by the equation (3.14). Two different operating bias $V_{applied}$=225V and $V_{applied}$=500V are considered for the 30 segments detector. The doping concentration is N_d=1×10^{18}m^{-3} and trapped charge density

N_{ta}=1×10^{14}m^{-2} for L_G=10μm; N_{ta}=2.5×10^{14}m^{-2} for L_G=25μm; N_{ta}=5×10^{14}m^{-2} for L_G=50μm grain size. Figure 4.8 shows the effect of grain size on the electric field distribution for two bias voltages. The number of drifting segment does not alter with the increase of grain size (provided that the total trapped charge in the detector is constant). The HgI_2 layer thickness varies from 100-500 μm, grain size varies from 20-60 μm [27], [77]. We varied grain size of the detector from 10μm, 25 μm and 50μm. Large grain size causes temporal lag and non-uniform response of the detector. It is reported that HgI_2 image detectors with smaller grain sizes show less non-uniformity [43]. The grain sizes must be much smaller than the pixel size to get uniform response. Therefore, it is required to select optimum grain size to achieve uniform response and better charge collection efficiency.

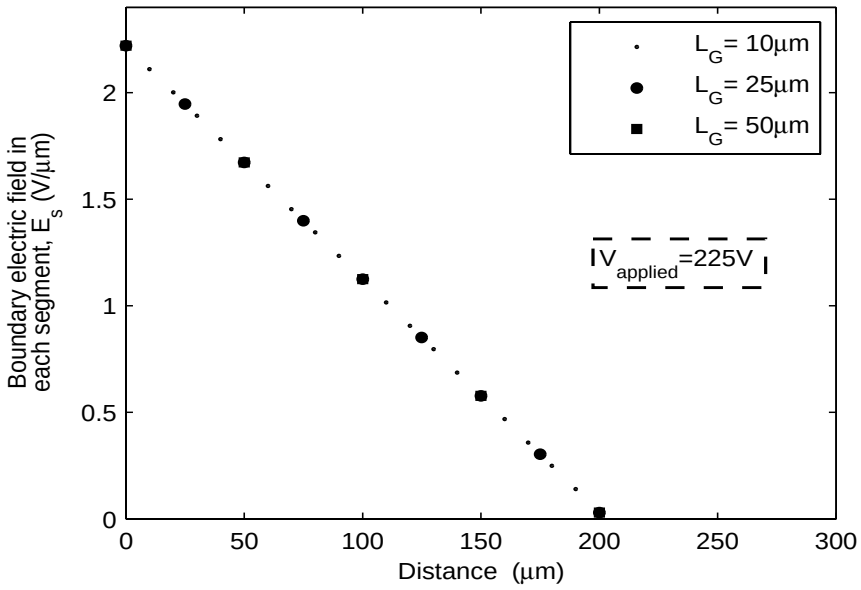

(a)

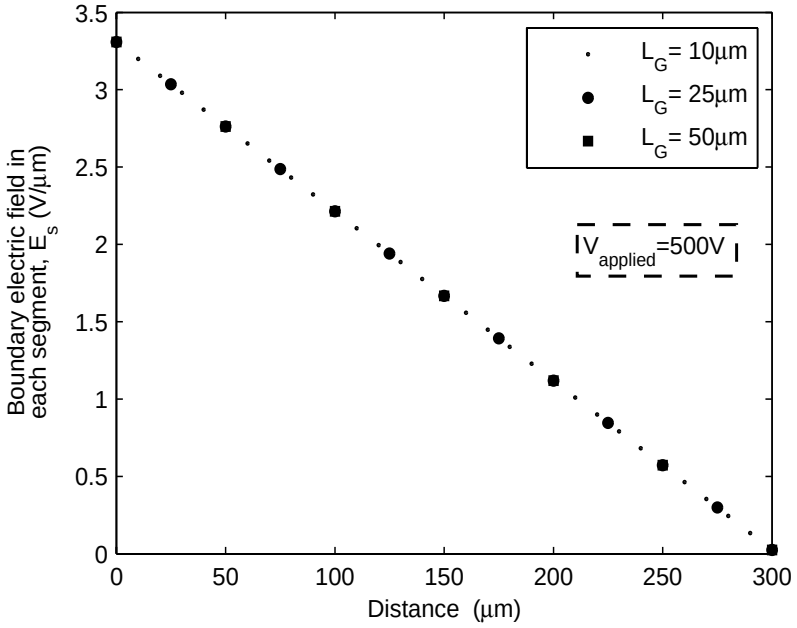

(b)

Figure 4.8 Effect of grain size on electric field in each segment for different operating bias (a) $V_{applied}$=225V, (b) $V_{applied}$=500V. The length of individual grain (L_G) does not have any influence on the electric field if the trapped charge density is constant for a particular operation of the detector.

4.6 Energy Barrier Height at Low-doped Detector

The potential barrier height at low doped polycrystalline materials ($N_{ta}>N_dL_G$) is obtained by using equation (3.20) for a particular detector segment at certain operating condition. There exists a potential barrier for charge carriers if the electric field within a particular segment changes its sign. Figure 4.9 shows the typical example for having barrier in the low doped polycrystalline detector. Therefore to investigate the presence of energy barrier we need to evaluate electric field and potential by solving the equations (3.11 (a)) through (3.11(c)).Then we can calculate the energy barrier height by using equation (3.20) if there is any barrier present for particular operating condition.

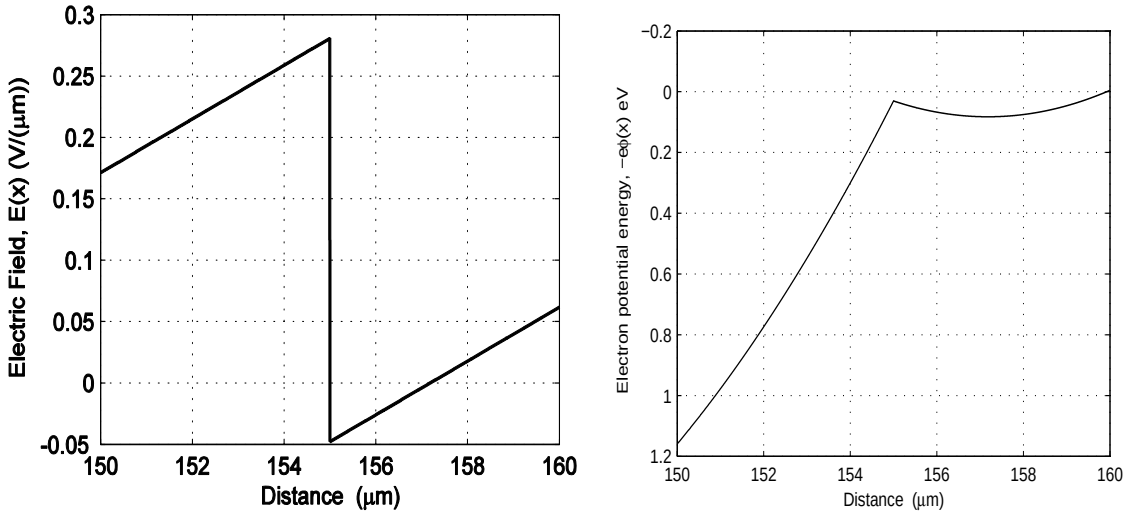

(a) (b)

Figure 4.9 Typical example of energy barrier creation at low doping region. Here, N_{ta}=1.5×10^{14} m^{-2}, N_d=10^{19}m^{-3}, m=30, $V_{applied}$=150V, (a) electric field, (b) electron potential energy -$e\Phi(x)$ in eV.

In order to investigate the presence of an energy barrier we consider a certain combination of applied bias, doping and grain boundary trapped charge density so that a zero average field region exists in some part of the detector. Considering N_d = 10^{19} m^{-3}, $V_{applied}$ = 150 V, m = 30, L_G = 10 μm, and N_{ta} = 1.1 × 10^{14} m^{-2}, M becomes 30 i.e. the non-zero average field region prevails throughout the entire detector. In this case, the electric field and potential distributions across the detector thickness are shown in Figure 4.10. The electric field does not change its sign and therefore there is no barrier for charge carriers. This effect enhances the charge collection efficiency as both barrier and polarization effects are absent.

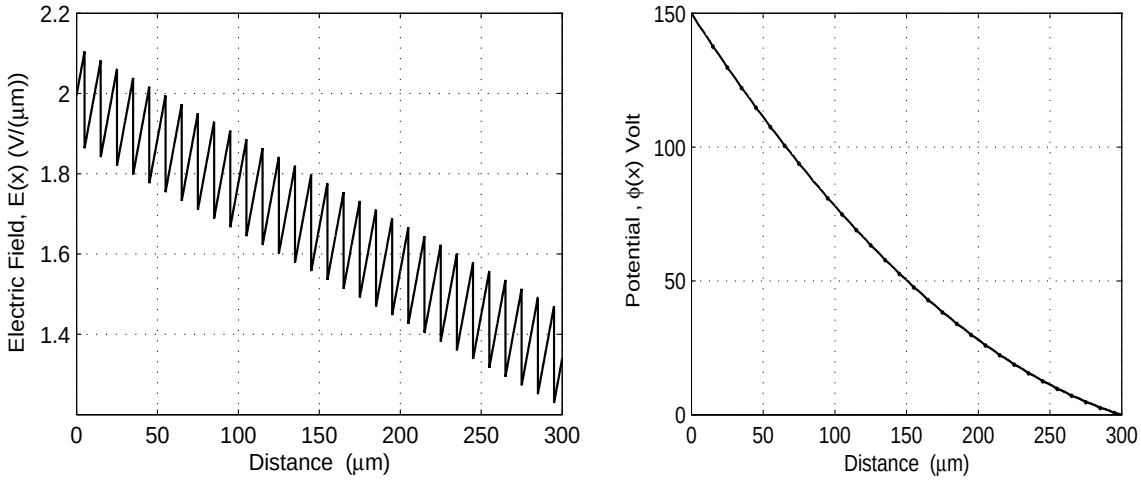

(a) (b)

Figure 4.10 Electric field (figure a) and potential (figure b) distributions when N_{ta}=1.1 × 10^{14}. The doping concentration N_d=10^{19} m^{-3} and $V_{applied}$= 150V.

The increase of trap charge density changes the internal electric field distribution and the number of non-zero average electric field regions according to the equation (3.18). Figure 4.11 represent the electric field and potential of the detector when the trapped charge density increases from N_{ta}= 1.1 × 10^{14} m^{-2} to N_{ta}= 1.4 × 10^{14} m^{-2} and other parameters are the same as in Fig 4.10. *M* becomes 18. The average potential drop beyond 18th segment is zero. The average electric field up to 18th segment (i.e. up to 180 μm in Figure 4.11(a)) is non-zero and it is approximately zero in the rest of the detector. The electric field changes its sign starting from the 18th segment and thus there is no energy barrier for electron up to the 17th segment. The potential distribution in Figure 4.11 (b) shows that there exists an energy barrier for electrons at the 18th segment and the barrier height is 0.095 eV.

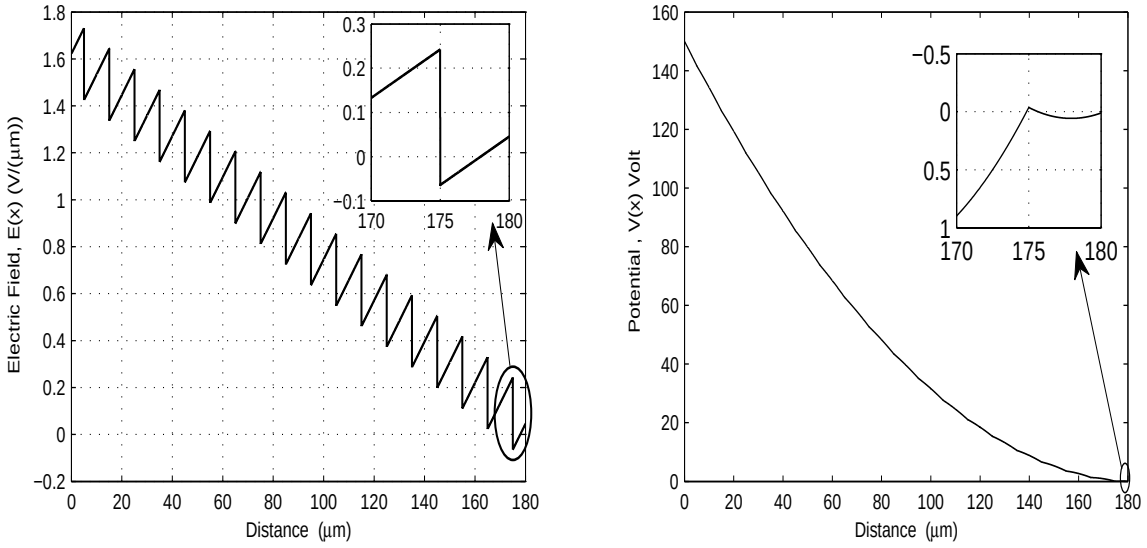

(a) (b)

Figure 4.11 The electric field $E(x)$ and potential $\Phi(x)$ distributions across the detector thickness when the non-zero average electric field region does not exist throughout the detector thickness. The doping concentration $N_d = 10^{19}$ m^{-3}, $V_{applied} = 150$ V, $m = 30$, $L_G = 10$ μm, and $N_{ta} = 1.4 \times 10^{14}$ m^{-2}. The inset in (b) shows the electron potential energy diagram in eV.

The doping concentration and applied bias can change the internal electric field distribution at fixed trapped charge density in the polycrystalline detector. In the previous operating condition the detector has both polarization phenomena and barrier height starting from the 18th segment of the detector. Considering all the previous conditions if we increase the doping concentration from $N_d = 10^{19}$ m^{-3} to $N_d = 1.3\times10^{19}$ m^{-3}; M becomes 30 i.e. the non- zero average field region prevails throughout the entire detector. Moreover electric field does not change its sign and therefore there is no barrier height for charge carriers (Figure 4.12).

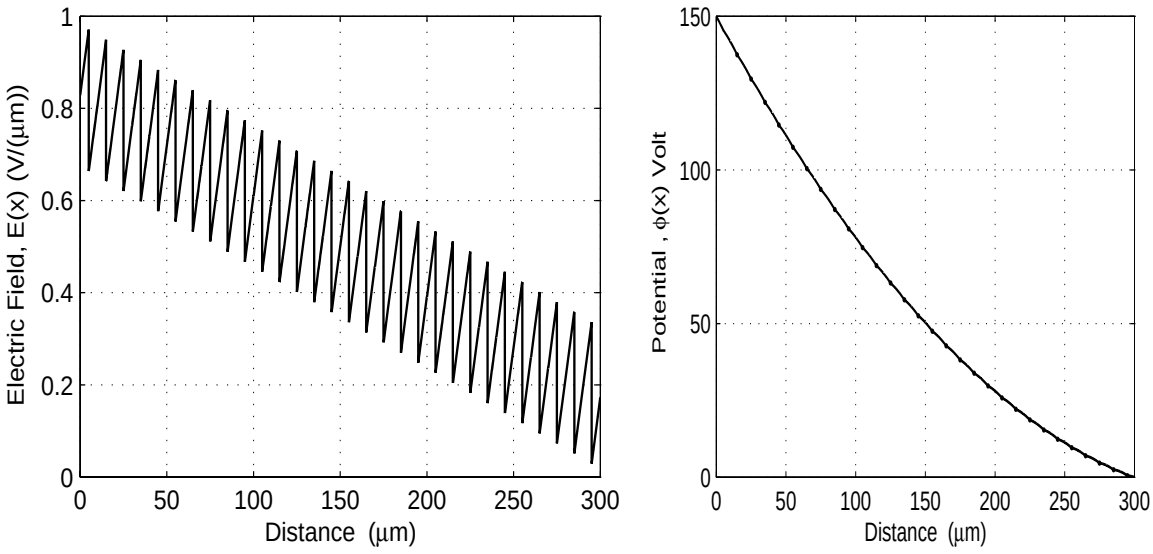

(a) (b)

Figure 4.12 The electric field $E(x)$ and potential $\Phi(x)$ distributions across the detector thickness when the non-zero average electric field regions exist throughout the detector thickness. The doping concentration $N_d = 1.3 \times 10^{19}$ m^{-3}, $V_{applied} = 150$ V, $m = 30$, $L_G = 10$ μm, and $N_{ta} = 1.4 \times 10^{14}$ m^{-2}.

Figure 4.13 shows the effect of increase in the applied bias on the polarization effect and barrier height for charge carriers. Considering $N_d = 10^{19}$ m^{-3}, $m = 30$, $L_G = 10$ μm, $N_{ta} = 1.4 \times 10^{13}$ m^{-2} (other parameters are the same as in Figure 4.11) and increases the bias voltage from $V_{applied} = 150$ V to 500V. The number of non zero average electric field region (M) increase from 18 to 30 i.e. the non- zero average field region prevails throughout the entire detector. Moreover there is no barrier for charge carrier.

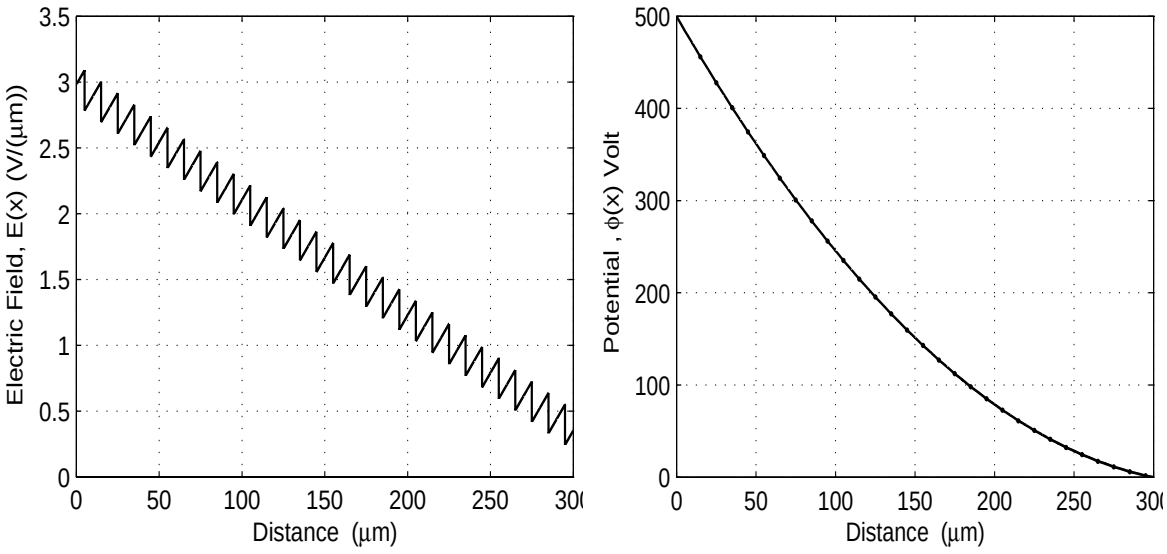

(a) (b)

Figure 4.13 Electric field (figure a) and potential (figure b) distributions when $N_d = 1 \times 10^{19}$ m^{-3}, $V_{applied} = 500$ V, $m = 30$, $L_G = 10$ μm, and $N_{ta} = 1.4 \times 10^{14}$ m^{-2}. The polarization effect disappears due to the increase in applied bias.

The barrier height is controlled by the applied bias, doping concentration and trapped charges. For a very high grain boundary trapped charges (~10^{15} m^{-2}) together with moderate doping (~10^{20} m^{-3}) condition, the electric field changes its polarity in many segments without having a zero average electric field region. In this case, N_{ta} is slightly greater than $N_d L_G$. The potential barrier exists in many segments but its magnitude varies throughout the detector. In order to investigate this situation in moderately doped polycrystalline detector we consider a certain combination of applied bias, doping and grain boundary trapped charge density. Considering $N_d = 10^{20}$ m^{-3}, $V_{applied} = 300$ V, $m = 30$, $L_G = 10$ μm, and $N_{ta} = 1.005 \times 10^{14}$ m^{-2} in Figure 4.14. The energy barrier height increases gradually through the detector. However this barrier height can be decreased by increasing applied bias within the practical limit of dark current of the detector.

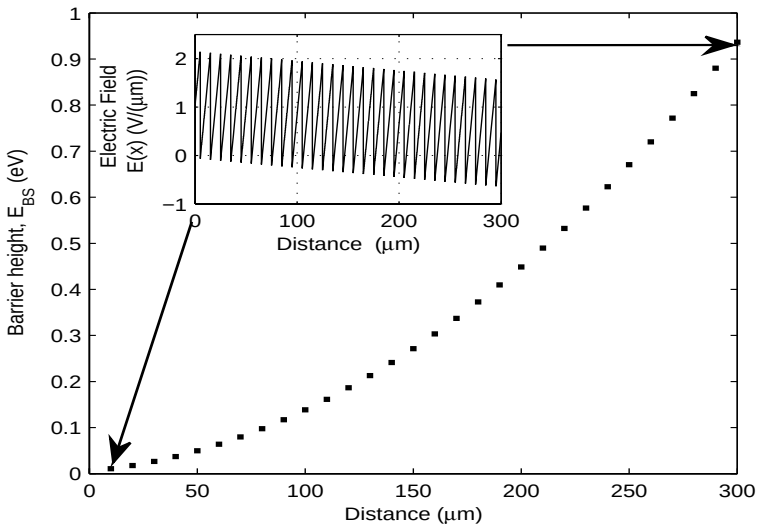

(a)

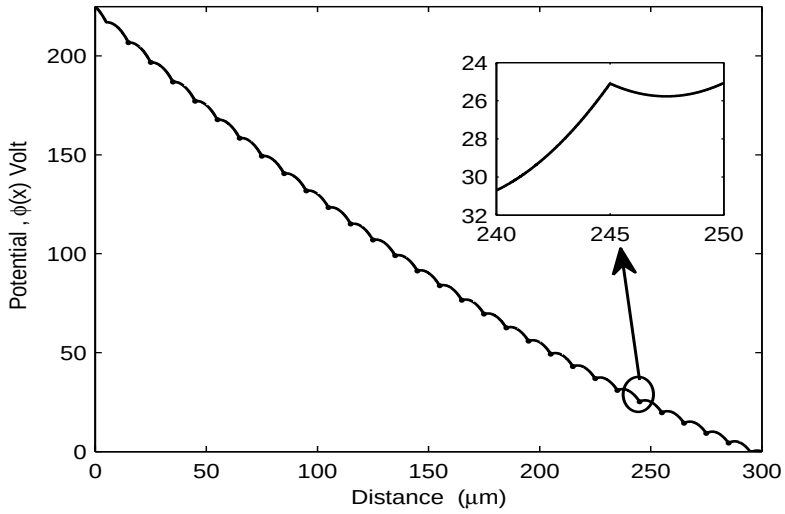

(b)

Figure 4.14 Potential barrier height with electric field distribution (figure a), and potential (figure c) distributions when N_{ta} is very high and slightly greater than $N_d L_G$. The doping concentration $N_d = 10^{20}$ m^{-3} and $N_{ta} = 1.009 \times 10^{15}$ m^{-2}. The inset in (b) shows the electron potential energy diagram in eV.

Figure 4.15 (a) shows that the barrier height decreases with increasing bias $V_{applied}$. The applied operating bias alters the Electric field through the detector as shown in Figure 4.15 (b) and thus the polarity of electric field cannot change for some of the detector segments which cause the barrier height to be zero. Therefore, energy barrier height decreases largely with the increase of the operating bias. The corresponding potential diagram is shown in Figure 4.15 (c). Here it is shown that the potential barrier is higher for a particular segment for the applied bias 225V (lower one in Figure 4.15 (c)). Moreover the increase in applied bias decreases the polarization effect and thus improves the transit time of the charge carrier. Therefore, by increasing the applied bias the charge collection efficiency of the detector can be improved.

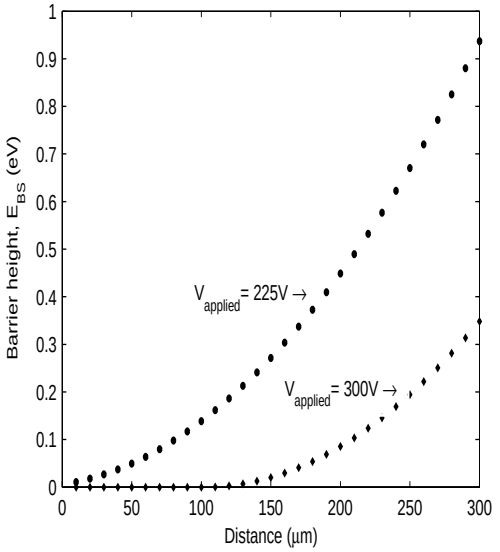

(a)

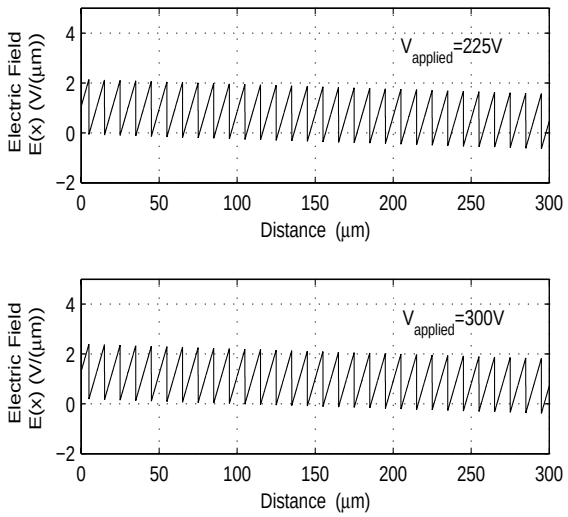

(b)

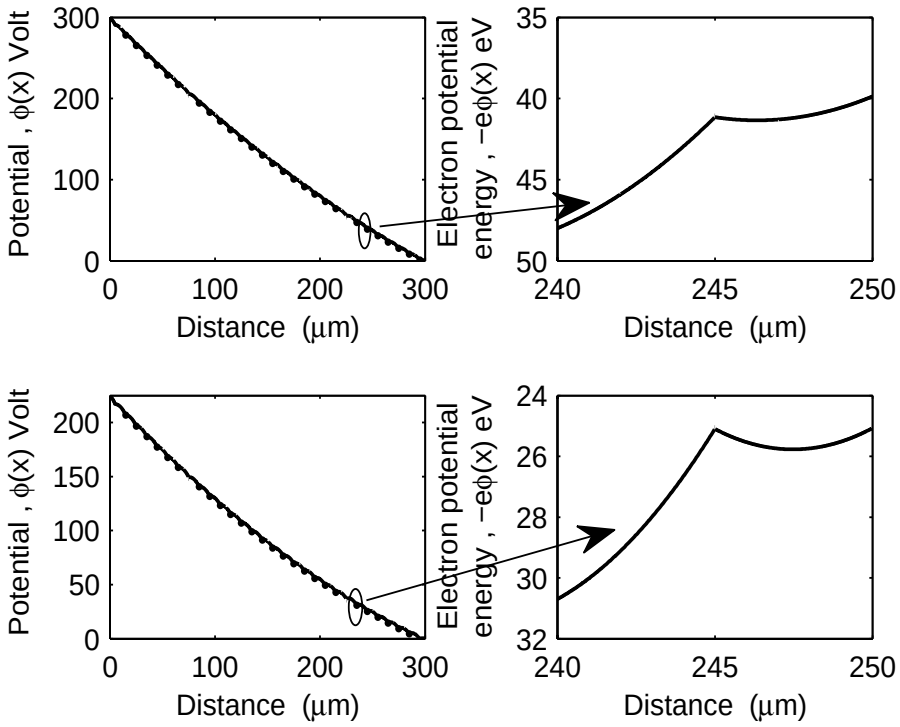

(c)

Figure 4.15 Potential barrier height (figure a), electric field (figure b) and potential (figure c) distributions when N_{ta} is very high and slightly greater than $N_d L_G$. The doping concentration $N_d = 10^{20}$ m^{-3} and $N_{ta} = 1.009 \times 10^{15}$ m^{-2}. Inset in (c) shows the electron potential energy diagram in eV.

4.7 Electrical Properties at Intrinsic Detector

The intrinsic doping (N_{di}) of a polycrystalline detector under applied bias can be determined by equation (3.16) .We consider P=1 i.e. 1% change in electric field due to the space charge to define the intrinsic doping level of a particular detector at a particular operating condition. Let us consider the applied bias $V_{applied}$=150 V, grain size L_G=10μm,

no. of detector segments m=30, and relative permitivity of the polycrystalline material ε_r=8.3 (HgI_2) and thus the intrinsic doping concentration becomes $N_{di}=1.522\times10^{16}m^{-3}=1.522\times10^{10}$ cm^{-3}. If the doping is less than this, it can be treated as intrinsic doping under applied bias of 150V.

The electric filed variation at the boundary of each detector segment with the change of trapped charge density at the grain boundary interface is depicted in Figure 4.16. Here, the doping concentration is $N_{di}=1.522\times10^{16}m^{-3}$, no. of detector segments m=30, grain size of each detector segments L_G=10μm.The operating bias is 150V. The magnitude of the boundary electric filed change with the trapped charge density according to the equation (3.14).The high-field region prevails for whole detector segments if the trapped charge density remains about $N_{ta}\sim1\times10^{13}m^{-2}$. However if the trapped charge density increases, the detector segments has two different regions: high-field drift region and low-field diffusion region. No. of drift and diffusion region varies with the trapped charge density and is obtained by the equation (3.18). The internal electric field changes with increasing trapped charge density and thus causes polarization effect to take place in the detector. For this particular condition the charge carriers have to travel 50% of the detector through diffusion if the trapped charge density increases up to $N_{ta}=6\times10^{13}m^{-2}$. This may causes huge degradation of charge transport efficiency.

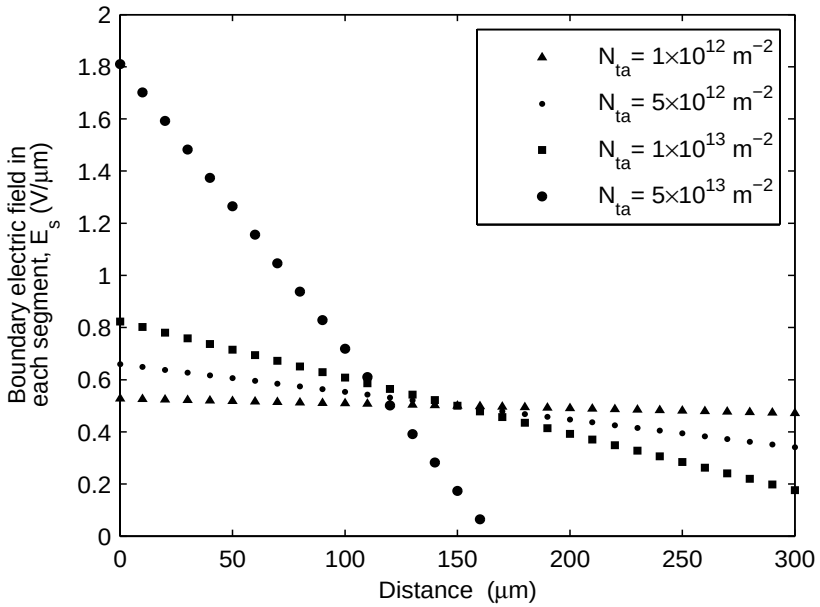

Figure 4.16 Boundary electric field in each segment of the detector for different trapped charge density at grain boundary interface. Here, applied bias,$V_{applied}$=150V, doping concentration N_d=1.552×10^{16}m^{-3} (intrinsic doping at applied bias of 150V).

Polarization effect can be reduced by increasing the applied bias of the detector. The number of drifting segment is required to increase to reduce the transit time of the carrier through the detector. Figure 4.17 shows that the number of drifting detector segment is increased with the increase of operating bias. The Intrinsic doping concentration is also altered with the applied bias by the equation (3.16). Here, Intrinsic doping concentration N_{di}=2.2836×10^{16} m^{-2} at an applied bias $V_{applied}$=225 V and N_{di}=3.0448×10^{16} m^{-2} at an applied bias $V_{applied}$=300 V. The no. of drift and diffusion region varies with the trapping and doping concentration and is obtained by the equation (3.18).

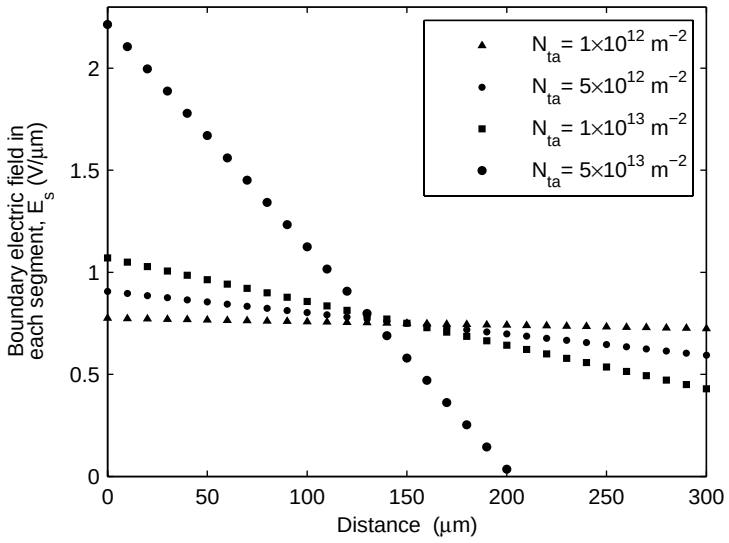

(a)

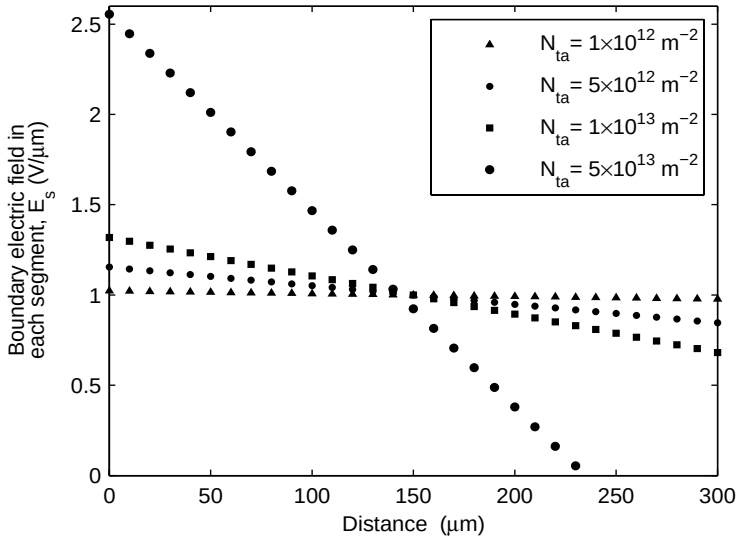

(b)

Figure 4.17 Effect of operating biasing on the number of drift and diffusion segment in the intrinsic doped detector for different trapped charge density (a) $V_{applied}$=225V, intrinsic doping concentration at this applied bias N_{di}=2.2836×10^{16}m^{-2}, (b) $V_{applied}$=300V, intrinsic doping concentration at this applied bias N_{di}=3.0448×10^{16}m^{-2}.

From Figure 4.18 it is found that not all the segments have high-field effect for the trapped charge density N_{ta}=3×10^{13}m^{-2}. However if we increase the operating bias to

$V_{applied}$=300V then the whole detector segments has high field region i.e. no diffusion of carrier. Thus the transit time improves which in-turn increase the charge collection efficiency of the detector. The Number of drifting segments under different operating bias is determined by equation (3.18).

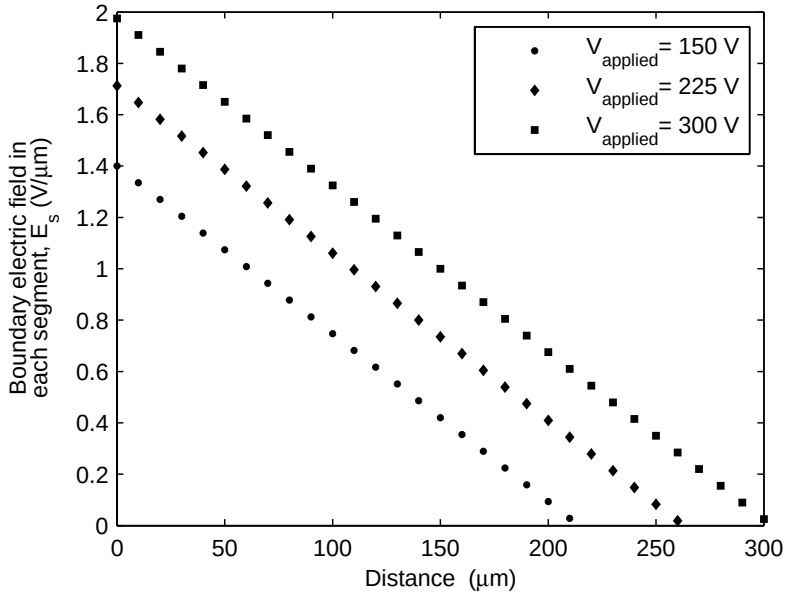

Figure 4.18 Variation of drift and diffusion segment in the intrinsic doped detector with operating bias for trapped charge density of N_{ta}=3×10^{13}m^{-2}. The no. of drifting segments increase with biasing.

Figure 4.19 shows the electrical field distribution and potential distribution through the detector at intrinsic doping N_{di}=1.522×10^{16}m^{-3}. Here, no. of grain m=30, and grain size L_G=10μm. There is no change of sign in the electric field and thus energy barrier will be zero for charge carrier. In this operation all the 30 segments are under high field region. Therefore, transit time of the carrier will be small. However due to small amount of doping the charge collection efficiency will be low.

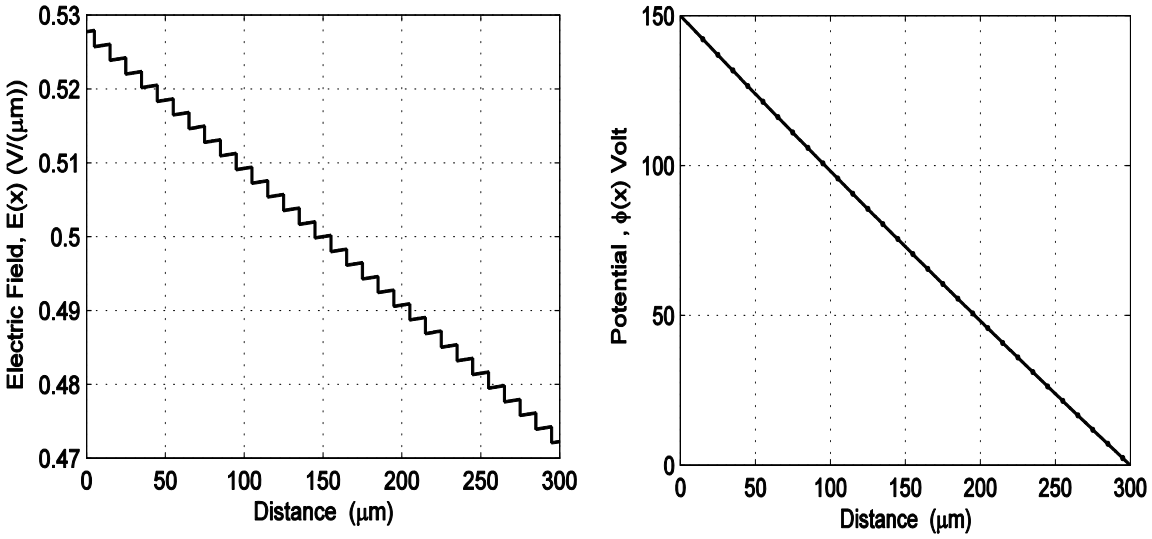

(a) (b)

Figure 4.19 (a) electric field distribution, and (b) potential distribution through m=30 segments detector at an applied bias $V_{applied}$=150V, trapped charge density N_{ta}=1×10^{12}m^{-2}, doping concentration N_{di}=1.552×10^{16}m^{-3}.

In case of intrinsic doped polycrystalline material the electric field will never change its sign. Therefore, the energy barrier will be zero all the time in the nonzero average field region. The number of drift and diffusion segment changes with the increase of trapped charge density set by equation (3.18). We increase the trapped charge density so that the 50% of the detector have the influence of drifting electric filed. However still electric field does not change the sign and thus barrier height is zero (Figure 4.20) in non zero-average electric field region.

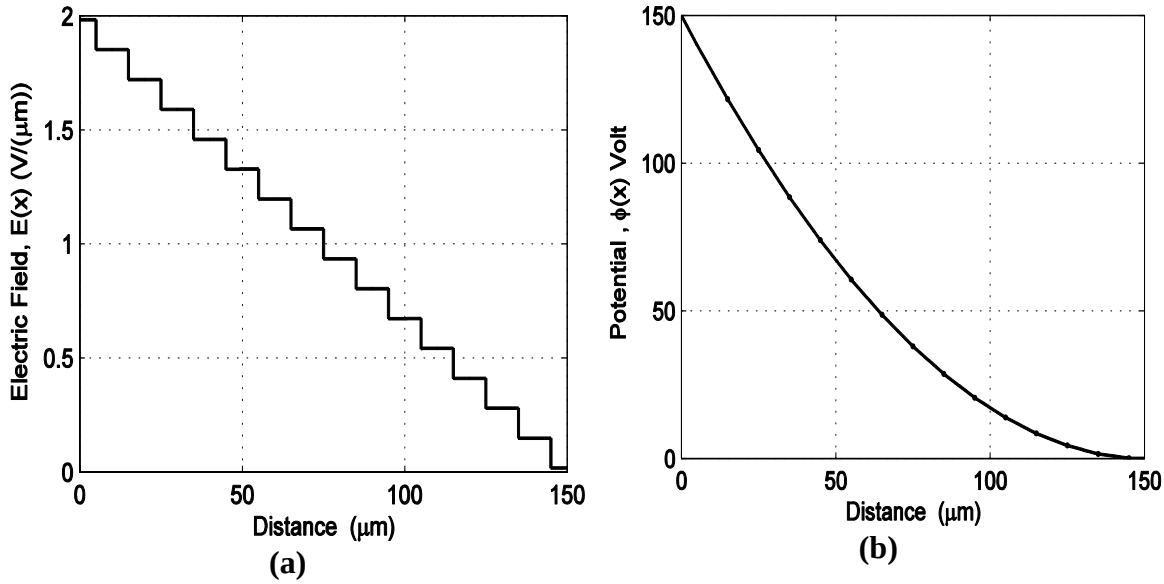

Figure 4.20 (a) electrical field distribution, and (b) potential distribution through m=30 segments detectors at an applied bias $V_{applied}$=150V, trapped charge density $N_{ta}=6\times10^{13}m^{-2}$, doping concentration $N_d=1.522\times10^{16}m^{-3}$.

4.8 Electrical Properties at Fully Depleted Grains Maintaining Charge Neutrality

The space charge region is expanded over whole grain for a particular combination of doping, trapping and operating bias at low doped polycrystalline material. A special case may arise, for which all the grains will be depleted as well as charge neutrality is maintained throughout the detector. This is the on-set condition of low-doped ($N_{ta}\geq N_dL_G$) case. The barrier height may exist depending on the magnitude of the trapped charge density at the grain boundary interfaces. The barrier height can be determined by the equation (3.20) by considering charge neutrality condition ($N_{ta}=N_dW=N_dL_G$). The magnitude of the barrier height will be equal for all considered grains.

Figure 4.21(a) shows the electric field distribution through the 30 segment detector with grain size of 10μm at an operating bias of $V_{applied}$=150 V. The doping concentration N_d=4×10^{19}m^{-3} and trapped charge density N_{ta}= 4×10^{14}m^{-2}. In this case the detector is charge neutral ($Nta=N_dW=N_dL_G$). At this situation there is no change of electric field for any particular segment. The corresponding potential diagram ($\Phi(x)$) is shown in Figure 4.21 (b) .However the high-field drift region prevails throughout the whole detector.

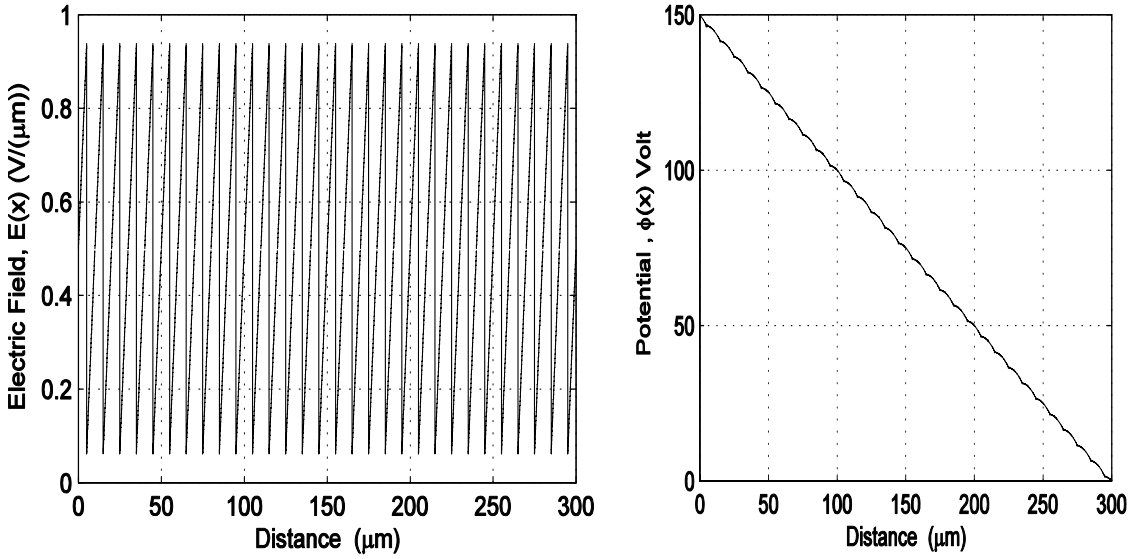

Figure 4.21 (a) electric field distribution, and (b) potential distribution through m=30 segments detector at charge neutral condition. Applied bias $V_{applied}$=150V, trapped charge density N_{ta}=4×10^{14}m^{-2}, doping concentration N_d=4×10^{19}m^{-3}.

The increase of trapped charge density changes the electric field distribution and the non-zero average segments according to the equation (3.18). Figure 4.22 represent the electric field and potential of the detector when the trapped charge density increases from N_{ta}=

$4\times10^{14}m^{-2}$ to N_{ta}= $5\times10^{14}m^{-2}$ and doping concentration N_d=$4\times10^{19}m^{-3}$ to N_d=$5\times10^{19}m^{-3}$ to maintain the charge neutrality at the applied bias $V_{applied}$= 150V. Here, the electric field changes polarity and therefore there will be barrier for charge carriers. The magnitude of the barrier height is the same for all the detector segments. However the barrier height is small as shown in Figure 4.22(b). The charge carriers will have to overcome this potential barrier to pass the whole detector segments.

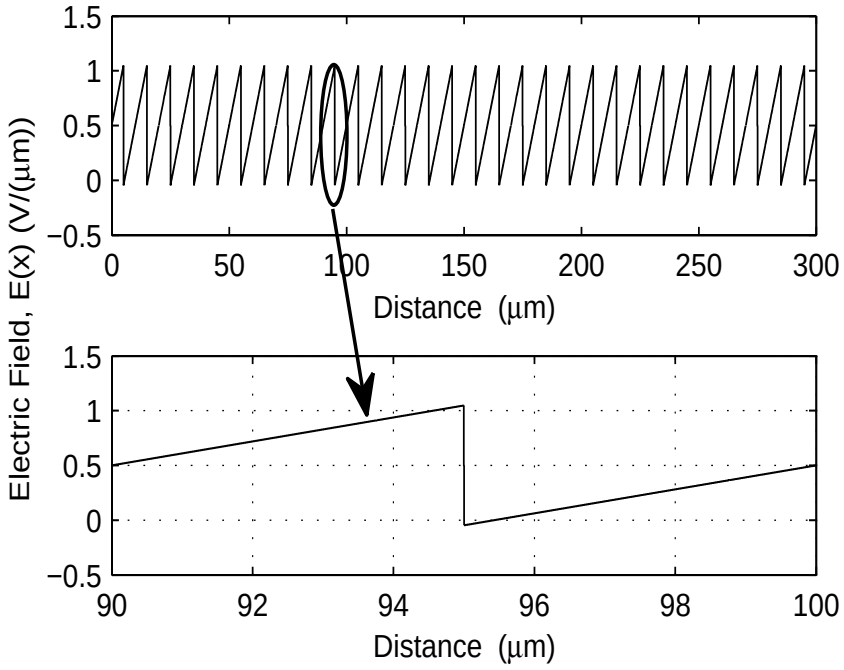

(a)

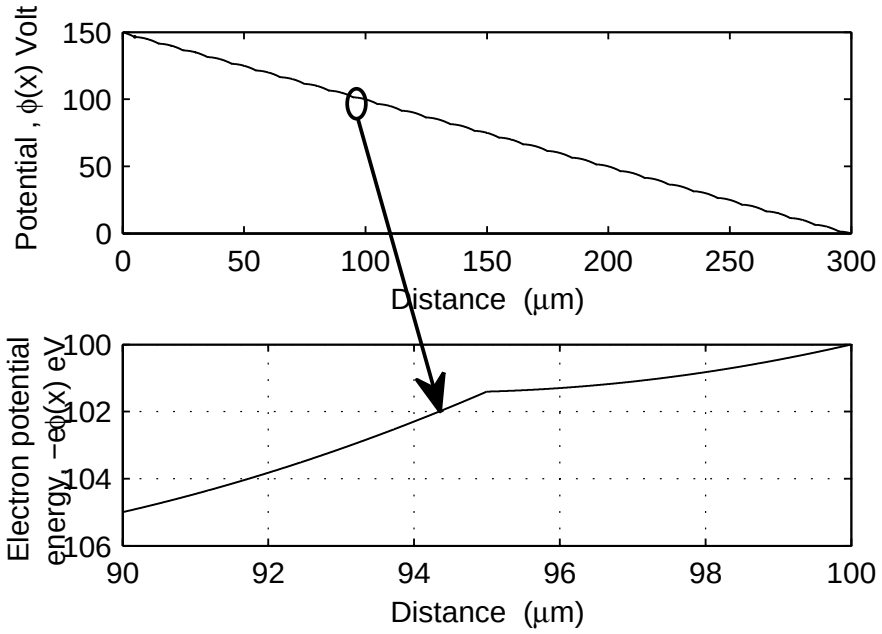

(b)

Figure 4.22 (a) electric field distribution, and (b) electron potential energy distribution, $-e\Phi(x)$ eV, through m=30 segments detector at charge neutral condition. Trapped charge density $N_{ta}=5\times10^{14}\text{m}^{-2}$, doping concentration $N_d=5\times10^{19}\text{m}^{-3,}$ and applied bias $V_{applied}$=150V.

The change of barrier height with the increase of trapped charge density is expressed in the Figure 4.23 for various combinations mentioned in Table 4.1. The barrier height increases with the increase of trapped charge density for a fixed operating bias.

Table 4. 1 Different operating combination of the detector at charge neutrality condition

Combination	Trapping concentration N_{ta} (m^{-2})	Doping concentration N_d (m^{-3})
1	5×10^{14}	5×10^{19}
2	7×10^{14}	7×10^{19}
3	9×10^{14}	9×10^{19}

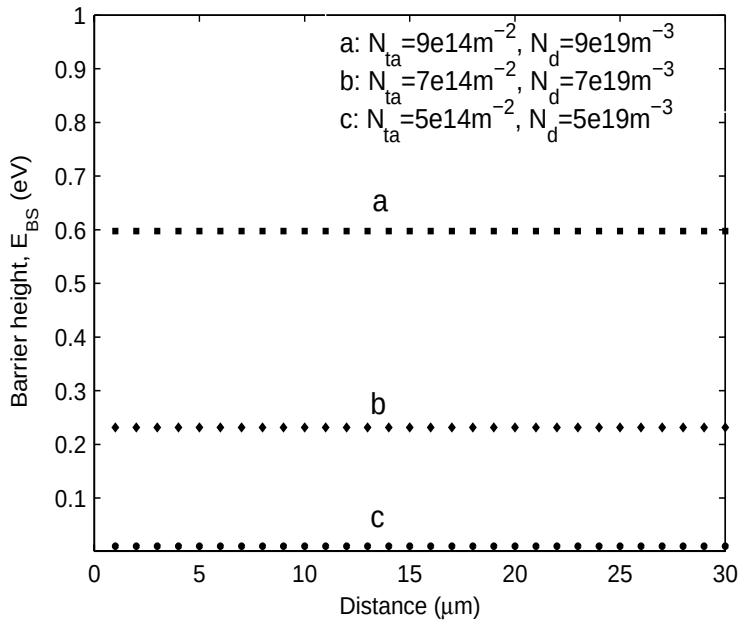

Figure 4.23 Effect of trapping on barrier height through the detector segments at charge neutrality condition. Here applied bias $V_{applied}$=150V.

The Electric field of the detector segment can be controlled by changing the applied bias $V_{applied}$. The effect of operating bias on electric field is shown in Figure 4.24(a). Considering the doping concentration N_d=5×10^{19}m^{-3} and trapped charge density N_{ta}= 5×10^{14}m^{-2} at an operating bias $V_{applied}$=225V. The electric field for the same trapped charge density and doping concentration at an operating bias $V_{applied}$=150V is shown in Figure 4.22(a). At an applied bias 150V the electric field changes polarity and therefore creates barrier for charge carrier (Figure 4.22(b)). However by increasing applied bias the electric field distribution is changed as shown in Figure 4.24(a). For this case the sign of the electric field does not change and thus there is no sign of barrier for charge carrier (Figure 4.24(b)).

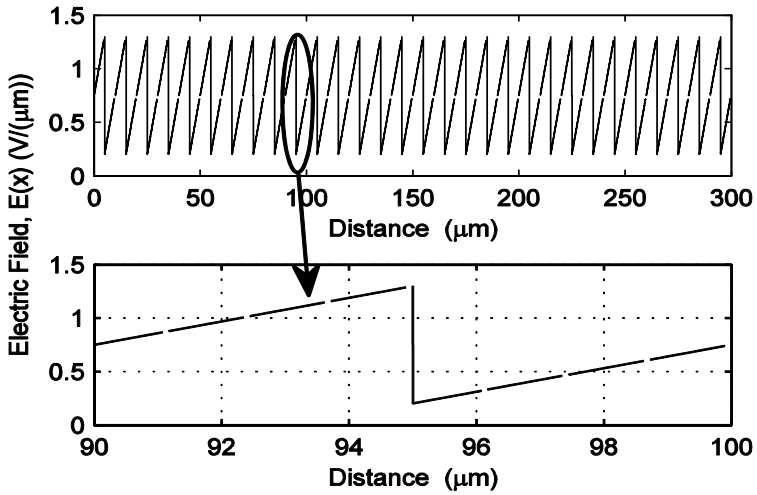

(a)

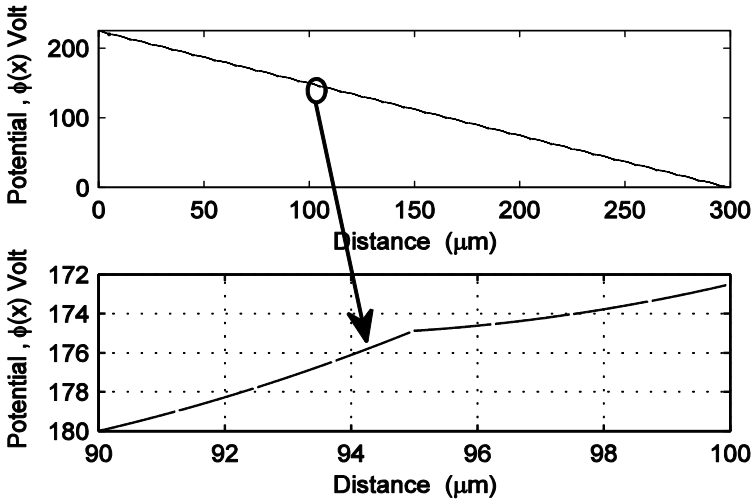

(b)

Figure 4.24 Effect of bias voltage on the (a) electric field, (b) electron potential energy distribution, $-e\Phi(x)$ eV, through charge neutral detector.

The increased applied bias diminishes the barrier height for charge carriers. Figure 4.25 shows the influence of the applied bias on the barrier height through the detector. The magnitude of the barrier rapidly decreases with increasing of voltage from 150V to 300 V

for the same trapped charge density $N_{ta}=1\times10^{15}\text{m}^{-2}$ and doping concentration $N_d=1\times10^{20}\text{m}^{-3}$.

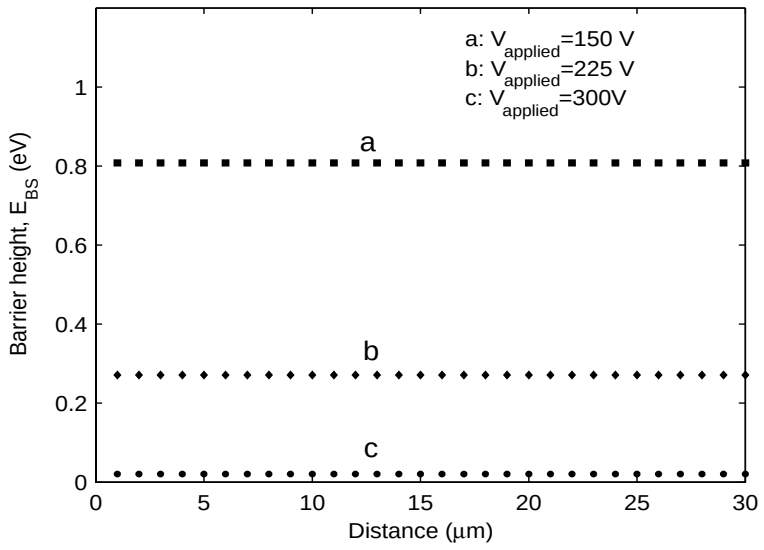

Figure 4.25 Effect of biasing voltage on barrier height through the detector segment at charge neutrality condition. Here, trapped charge density $N_{ta}=1\times10^{15}\text{m}^{-2}$ and doping concentration $N_d=1\times10^{20}\text{m}^{-3}$.

In this chapter, a detail analysis of the grain boundary properties of polycrystalline materials are given under various combination of trapped charge density, doping concentration, and applied biases.

CHAPTER 5 CONCLUSION, CONTRIBUTIONS & FUTURE WORK

In this thesis a theoretical model has been developed for evaluating the effect of trapped charge in grain boundary interfaces of low-doped polycrystalline detector under applied bias condition. The model considers the effects of carrier transport in all the grains of the multi-grains detector. Moreover each grain is divided into three distinct regions and the charge concentration in each region is calculated based on the systematic solution of the Poisson's equation in a photoconductor. The dynamic model ultimately is useful in developing samples to improve charge collection efficiency as well as image quality in the medical image detector or output current in the solar cell. A detector sample with appropriate doping in a particular operating condition (trapping concentration, applied bias) for various imaging and photovoltaic applications can be fabricated. The proposed model is also extended for heavily doped polycrystalline material.

5.1 Contributions

An analytical model for evaluating the electrical properties of the polycrystalline detector has been described. The electric field may collapse, i.e., a nearly zero average electric field region exists, in some part of the biased detector at high trapped charge densities at the grain boundaries. This effect can reduce the charge collection efficiency and the

response time of the detector. This polarization effect diminishes with increasing the applied voltage of the detector. There exists a potential barrier at the grain boundary only if the electric field changes its polarity at the opposite side of the grain boundary. The most of the grains possess barrier in the moderately doped (~10^{20} m^{-3}) polycrystalline detector at high trapped charge densities (~$10^{15}m^{-2}$) and slightly imbalanced charge neutral circumstances. It is found that the potential barrier may not present in all grains at low doped polycrystalline materials and it never exists in intrinsic polycrystalline detector under applied bias condition provided there is no charge in the grain. Therefore, intrinsic or low-doped polycrystalline materials are suitable for detector or solar cell applications. Therefore the contribution of the present research in the development of polycrystalline detectors summarize as,

- An analytical grain boundary model for determining electrical properties of polycrystalline materials considering an arbitrary amount of grain boundary charges, doping, bias voltages and a finite width of grain boundary region has been developed. This model is applicable for any doping levels of the polycrystalline materials under biasing condition.
- The electrical properties (e.g. electric and potential distributions, charge carrier barrier height) of grain boundaries in polycrystalline detectors under various combinations of doping concentration, trapped charge density and applied biases have been analyzed. Polycrystalline mercuric iodide (HgI_2) detector is taken as an example.
- The polarization phenomenon in polycrystalline based detectors has been explained by the model. The conditions of existence of an energy barrier at the

grain boundary and a zero average field region in some portion of the detector have also been determined.

- The effect of bias voltage on the polarization phenomena has been evaluated by this theoretical model.

Although, polycrystalline mercuric iodide is taken as sample calculations, the model is applicable for any polycrystalline materials used in detectors and solar cell applications.

5.2 Suggestions for Future Work

The effects of carrier trapping and de-trapping, and minority carrier recombination with trapped charges in the grain boundary force an equilibrium trapped charge density in the grain boundary under light illumination and biasing condition. In other way, these effects limit the trapped charge density at the grain boundary. Therefore, the proposed grain boundary model in this thesis can be improved by incorporating the charge carrier trapping in the grain and the minority carrier recombination with trapped charges in the grain boundary.

REFERENCES

[1] G. Zopp , I. Forbes, R. W. Miles, P. J. Dale, J. J. Scragg, and L. M. Peter, "$Cu_2ZnSnSe_4$ thin film solar cells produced by Selenisation of magnetron sputtered precursors," *Prog. Photovolt: Res. Appl.,* vol.17, pp.315-319, 2009.

[2] N. E. Hartsough, E. Nygard, N. Malakhov, W. C. Barber, and T. Gandhi, "Polycrystalline mercuric iodide films on CMOS readout arrays," *IEEE Trans Nucl Sci.,* vol.56, no. 4,pp. 1810–1816, August 2009.

[3] Z. A. Smith, and K. D. Taylor, "Renewable and alternative energy resources," ABC-CLIO, Inc., Santa Barbara, California, p.164, 2008.

[4] D. M. Chapin, C. S. Fuller, G. L. Pearson, "A new silicon p-n junction photocell for converting solar radiation into electrical power," *J. Appl. Phys.*, vol. 25, 676–677, 1954.

[5] K. Yu, and J. Chen,"Enhancing solar cell efficiencies through 1-d nanostructures," *Nanoscale Res. Lett.*, vol. 4, pp.1–10, 2009.

[6] A. M. Acevedo, "Effective absorption coefficient for graded band-gap semiconductors and the expected photocurrent density in solar cells," *Solar Energy Materials & Solar Cells,* vol.93, pp.41– 44, 2009.

[7] T. Zdanowicz, T. Rodziewicz, M. Zabkowska-Waclawek, "Theoretical analysis of the optimum energy bandgap of semiconductors for fabrication of solar cells for applications in higher latitudes locations," *Solar Energy Materials & Solar Cells*, vol. 87, pp. 757–769, 2005.

[8] C. H. Henry, “Limiting efficiencies of ideal single and multiple energy gap terrestrial solar cells,” *Journal of applied physics B,* vol.51, pp. 4494, 1980.

[9]Y. Eisen, A. Shor, I. Mardor, “CdTe and CdZnTe gamma ray detectors for medical and industrial imaging systems”, *Nuclear Instruments and Methods in Physics Research A*, vol.428, pp.158-170, 1999.

[10] D. Patidar, K. S. Rathore, N. S. Saxena, K. Sharma, T. P. Sharma, “Energy band gap and conductivity measurement of CdSe thin films,” *Chalcogenide Letters*, vol. 5, no. 2, pp. 21 – 25, February 2008.

[11] S. Del Sordo, L. Abbene, E. Caroli, A. M. Mancini, A. Zappettini and P. Ubertini, “Progress in the development of CdTe and CdZnTe semiconductor radiation detectors for astrophysical and medical applications,” *Sensors*, vol.9, pp. 3491-3526, 2009.

[12] X. Wu, “High-efficiency polycrystalline CdTe thin-film solar cells,” *Solar Energy*, vol.77, pp. 803–814, 2004.

[13] A. M. Acevedo, “Thin film CdS/CdTe solar cells: research perspectives,” *Solar Energy*, vol.80, pp.675–681, 2006.

[14] M. A. Contreras, B. Egaas, K. Ramanathan, J .Hiltner, A. Swartzlander, F. Hasoon and R. Noufi, ” Progress toward 20% efficiency in Cu(In, Ga)Se_2 polycrystalline thin film solar cell,” *Progress in Photovoltaics: Research and Applications.,* vol. 7, pp.311-316,1999.

[15] M. A .Green, K Emery, Y. Hishikawa, and W. Warta, "Solar cell efficiency tables (version36)," *Prog. Photovolt: Res. Appl.,* vol.18, pp.346–352, June 2010.

[16] D. C. Hunt, O. Tousignant, and J. A. Rowlands,"Evaluation of the imaging properties of an amorphous selenium-based flat panel detector for digital fluoroscopy," *Med. Phys.*, 31, pp. 1166-1175, 2004.

[17] K. Suzuki, "Flat panel displays using amorphous and mono-crystalline semiconductor devices," in Amorphous and Microcrystalline Devices: Optoelectronic devices, edited by J. Kanicki, Boston, MA: Artech House, 1991, Ch. 3.

[18] J. A. Rowlands and J. Yorkston, "Flat panel detectors for digital radiography" in Handbook of Medical Imaging Vol. 1, edited by J. Beutel, H. L. Kundel and R. L. Van Metter (SPIE Press, Washington, 2000), Ch. 4.

[19] M. J. Yaffe and J. A. Rowlands, "X-ray detectors for digital radiology*," Phys. Med. Biol*., vol.42, pp. 1-39, 1997.

[20] A. R. Cowen, "Digital x-ray imaging," *Measurement Science and Technology*, vol.2, no.8, August 1991.

[21] I. Fujieda, G. Cho, J. Drewery, T. Gee, T. Jing, S. N. Kaplan, V. Perez-Mendez, and D. Widermuth, "X-ray and charged particle detection with CsI(T1) layer coupled to a-Si:H photodiode layers," *IEEE Trans. Nucl. Sci*., vol. 38, pp.255-262,1991.

[22] S. O. Kasap, and J. A. Rowlands, "Direct-conversion flat-panel x-ray image sensors for digital radiography," *Proc. IEEE*, vol. 90, pp. 591-603, 2002.

[23] E. Samei, and M. J. Flynn,"An experimental comparison of detector performance for direct and indirect digital radiography systems," *Med. Phys*., vol.30, pp. 608-622, 2003.

[24]J. M. Boone, "Chapter 1: X-ray production, interaction, and detection in diagnostic imaging", Handbook of Medical Imaging: Volume 1. Physics and Psychophysics, edited by Beutel J., Kundel H.L., and VanMetter R.L., SPIE Press, Bellington,2000, pp. 1-78.

[25] S. O. Kasap, "X-ray sensitivity of photoconductors: application to stabilized a-Se", *Journal of Physics D: Applied Physics*, vol.33, pp. 2853-2865, 2000.

[26] B. Polischuk, Z. Shukri, A. Legros, and H. Rougeot, "Selenium direct converter structure for static and dynamic x-ray detection in medical imaging," *Proc. SPIE*, vol.3336, pp. 494-504, 1998.

[27] S. O. Kasap, M. Zahangir Kabir, and J. A. Rowlands," Recent advances in x-ray photoconductors for direct conversion x-ray image sensors," *Current Applied Physics*, vol.6, pp.288-292, 2006.

[28] K. Oh, M. Yun, S. Choa, M. Kim, Y. Kim, Y. Kim, J. Sin, S. Nam, _ "Laminate structure detectors for low dark current with photoconductors in digital x-ray imaging," *Nuclear Instruments and Methods in Physics Research A*, vol.607, pp.158–161, 2009.

[29] S. O. Kasap and J. A. Rowlands, "X-ray photoconductor and stabilized a-Se for direct conversion digital flat-panel x-ray image detectors," *Journal of Material Science: Materials in Electron*ics, vol. 11, pp.179-198, 2000.

[30] A. Zuck, M. Schieber, O. Khakhan, and Z. Burshtein,"Near single-crystal electrical properties of polycrystalline HgI_2 produced by physical vapor deposition," *IEEE Trans. Nucl. Sci.*, vol. 50, pp. 991-997, 2003.

[31] S. Tokuda, H. Kishihara, S. Adachi, and T. Sato, "Improvement of the temporal response and output uniformity of polycrystalline CdZnTe films for high sensitivity x-ray imaging," *Proc. SPIE*, vol.5030, pp. 861-870, 2003.

[32] R. A. Street, S. E. Ready, K. Van Schuylenbergh, J. Ho, J. B. Boyec, P. Nylen, K. Shah, L. Melekov, and H. Hermon, "Comparison of PbI_2 and HgI_2 for direct detection active matrix x-ray image sensors," *J. Appl. Phys.*, vol. 91, pp. 3345-3355, 2002.

[33] S. Tokuda, H. Kishihara, S. Adachi, and T. Sato, "Preparation and characterization of polycrystalline CdZnTe films for large area, high sensitivity x-ray detectors: review*," J. Mat. Sci.: Mat. Elec.*, vol.15, pp. 1-8, 2004.

[34] M. Simon, R. A. Ford, A. R. Franklin, S. P. Grabowski, B. Mensor, G. Much, A. Nascetti, M. Overdick, M. J. Powell, and D. U. Wiechert, "PbO as direct conversion x-ray detector material," *Proc. SPIE*, vol.5368, pp. 188-199, 2004.

[35] S. O. Kasap and J. A. Rowlands, "Direct-conversion flat panel x-ray image detectors," *IEE Proc.-CDS,* vol. 149, pp. 85-96, 2002.

[36] M. Z. Kabir, S.O. Kasap and J.A. Rowlands, "Photoconductors for x-ray image detectors", in Springer Handbook of Electronic and Photonic Materials, (Springer, Würzburg, 2006), Ch. 48.

[37] H. Du, L. E. Antonuk, Y. El-Mohri, Q. Zhao, Z. Su, J. Yamamoto, and Y. Wang, "Investigation of the signal behavior at diagnostic energies of prototype, direct detection, active matrix, flat-panel imagers incorporating polycrystalline HgI_2," *Physics in Medicine and Biology*, vol.53, pp. 1325-1351, February 2008.

[38] M. Z. Kabir, "Effects of charge carrier trapping on polycrystalline PbO X-ray imaging detectors," *J. Appl. Phys.*, vol. 104, pp. 1–9, 2008.

[39] J. Y. W. Seto,"The electrical properties of polycrystalline silicon films," *Journal of Applied Physics*, vol. 46, no. 12, December 1975.

[40] F. Greuter, and G. Blatter, " Electrical properties of grain boundaries in polycrystalline compound semiconductors," *Semiconductor Science and Technology,* vol. 5, pp.111-137, February, 1990.

[41] Z. Su, L.E. Antonuk, Y. El-Mohri, L. Hu, Hong. Du, A. Sawant, Yixin. Li, Yi. Wang, Jin.Yamamoto and Q. Zhao, "Systematic investigation of the signal properties of polycrystalline HgI_2 detectors under mammographic, radiographic, fluoroscopic and radiotherapy irradiation conditions," *Physics in medicine and biology,*vol.50, pp.2907-2928, 2005.

[42] M. Schieber, A. Zuck, H. Gilboa, and G. Zentai, "Reviewing Polycrystalline Mercuric iodide x-Ray detectors," *IEEE Transactions on Nuclear Science*, vol.53, no.4, 2006.

[43] G. Zentai, L. Partain, R. Pavlyuchkova, C. Proano, B. N. Breen, A. Taieb, O. Dagan, M. Schieber, H. Gilboa, and J. Thomas, "Mercuric iodide medical imagers for low exposure radiography and fluoroscopy," *Proc. SPIE,* vol. 5368, pp. 200-210, 2004.

[44] M. Schieber, A. Zuck, M. Braiman, J. Nissenbaum, R. Turchetta, W. Dulinski,D. Husson, and J.L. Riester, "Novel mercuric iodide polycrystalline nuclear particle counters," *IEEE Transactions on Nuclear Science,* vol.44, no.6, pp. 2571-2575, 1997.

[45] R. C. Whited and L. V. D. Berg, "Native defect compensation in HgI_2 crystals," *IEEE Transactions on Nuclear Science,* vol.24, p.165, 1977.

[46] G. Zentai, M. Schieber, L. Partain, R. Pavlyuchkova, C. Proano, "Large area mercuric iodide and lead iodide x-ray detectors for Medical and non-destructive industrial imaging," *Journal of Crystal Growth*, vol.275, pp.1327-1331, 2005.

[47] M. Schieber, N. Zamoshchik, O. Khakhan, A. Zuck, "Structural changes during vapor-phase deposition of polycrystalline-PbI_2 films," *Journal of Crystal Growth*, vol.310, pp.3168–3173, 2008.

[48] G. Zentai, L. Partain, R. Pavlyuchkova, C. Proano, G. Virshup, L. Melekhov, A. Zuck, B. N. Breen, O. Dagan, A. Vilensky, M. Schieber, H. Gilboa, P. Bennet, K. Shah, Y. Dmitriev, and J. Thomas, "Mercuric iodide and lead iodide x-ray detectors for radiographic and fluoroscopic medical imaging," *Proc. SPIE*, vol.5030, pp. 77-91, 2003.

[49] J. F. Condeles, R. A. Ando, M. Mulato, " Optical and structural properties of PbI_2 thin films," *Jouranl of Material Science*, vol.43, pp.525-529, 2008.

[50] R. A. Street, S. E. Ready, F. Lemmi, K. S. Shah, P. Bennett, and Y. Dmitriyev, "Electronic transport in polycrystalline PbI_2 films," *Journal of Applied Physics*, vol.86, pp. 2660-2667, 1999.

[51]A. Brauers, N. Conrads, G. Frings, U. Schiebel, M.J. Powell, and C. Glasse, "X-ray sensing properties of a lead oxide photoconductor combined with an amorphous silicon TFT array," *Materials Research Society*, vol. 50, pp.321–326, 1998.

[52] M. Simon, R. A. Ford, A. R. Franklin, S. P. Grabowski, B. Menser, G. Much, A. Nascetti, M. Overdick, M.J. Powell, and D.U. Wiechert, "Analysis of Lead Oxide (PbO) layers for direct conversion x-Ray detection," *IEEE Transactions on Nuclear Science,* vol.52, no.5, pp.2035-2040, 2005.

[53] S. Irvine, "Solar cells and Photovoltaics," in Springer Handbook of Electronic and Photonic Materials, (Springer, Würzburg, 2006), Ch. 46.

[54] J. H. Won, K. H. Kim, J. H. Suh, S. H. Cho, P. K. Cho, J. K. Hong, and S. U. Kim, "The X-ray sensitivity of semi-insulating polycrystalline CdZnTe thick films, " *Nuclear Instruments and Methods in Physics Research A*, vol.591, pp.206-208, 2008.

[55] R. Decorby, M. Isshiki, J. Wang, "II-IV Semiconductors for optoelectronics: CdS, CdSe, CdTe," in Springer Handbook of Electronic and Photonic Materials, (Springer, Würzburg, 2006), Ch. 34.

[56] K. Kim , S. Cho, J. Suh, J. Won, J. Hong, S. Kim, "Schottky-type polycrystalline CdZnTe x-ray detectors," *Current Applied Physics*, vol.9, pp.306–310, 2009.

[57] S. H. Wei, S. B. Zhang, A. Zunger, "Effects of Ga addition to CuInSe2 on its electronic, structural, and defect properties," *Appl. Phys. Lett.*, vol.72 pp.3199-3201, 1998.

[58] G. Baccarani, and B. Ricco, "Transport properties of polycrystalline silicon films," *Journal of Applied Physics*, vol. 49, no. 11, November 1978.

[59] C. H. Seager**,** " Grain boundaries in polycrystalline Silicon,**"** *Annual Review of Materials Science*, vol. 1,pp. 271-302, August 1985.

[60] G. Blatter, and F. Greuter, "Electrical breakdown at semiconductor grain boundaries," *Physical Review B (Condensed Matter),* vol. 34, Issue 12, pp.8555-8572, December 15, 1986.

[61] S. N. Mohammad, and C. E. Rogers, "Theory of electrical transport and recombination in polycrystalline semiconductors under optical illumination," *Solid-State Electronics*, vol.31, no.7, pp.1157-1167, 1988.

[62] W. Shockley , and W.T.Reed, "Statistics of the recombination's of holes and electrons," *Physical Review*, vol.87, no.5, pp.835-842,1952.

[63] H. C. Card, and E. S. Yang,"Electronic process at grain boundaries in polycrystalline semiconductors under optical illumination," *IEEE Transactions on Electron Devices*, vol. ED-24, no.4, April 1977.

[64] P. Panayotatos, and H. C. Card,"Recombination velocity at grain boundaries in polycrystalline Si under optical illumination," *IEEE Transactions on Electron Devices*, vol. EDL-1, no.12, December 1980.

[65] C. H. Seager,"Temperature dependency of minority carrier recombination velocities at grain boundaries in silicon", *Applied Physics Letters*, vol.41, no.9, November 1982.

[66] C. H. Seager, "Grain boundary recombination: Theory and experiment in silicon", *Journal of Applied Physics*, vol.52, no.6, June 1981.

[67] D. P. Joshi,"Carrier recombination at grain boundaries in polycrystalline silicon under optical illumination," *Solid-State Electronics*, vol.29, no.1, pp.19-24, 1986.

[68] D. P. Joshi, and D. P. Bhatt, "Theory of grain boundary recombination and carrier transport in polycrystalline silicon under optical illumination," *IEEE Transactions on Electron Devices*, vol. 37, no.1, January1990.

[69] G. Horowitz, M.E. Hajlaoui, "Grain size dependent mobility in polycrystalline organic field-effect transistors," *Synthetic Metals*, vol. 122, pp.185-189, 2001.

[70] S. A. Kolosov, Y. V. Klevkov, and A. F. Plontnikov, "Electrical properties of fine-grained polycrystalline CdTe," *Semiconductors*, vol. 38, no.4, pp. 445-460, 2004.

[71] M. A. Matiowsky, and H. C. Card, "Temperature dependence of photoconductivity in polycrystalline semiconductors," *Solar Cells,* vol.*6,* pp.119 – 123,1982.

[72] J. W. Orton and M. J. Powell, "The hall effect in polycrystalline and powdered semiconductors," *Rep. Prog. Phys.,* vol. 43, pp. 1263-1307,1980.

[73] M. A .Green, K Emery, Y. Hishikawa, and W. Warta, "Solar cell efficiency tables (version 35)," *Prog. Photovolt: Res. Appl.,* vol.18, pp.144–150, 2010.

[74] C. A. Dimitriadis, “Influence of grain boundary recombination velocity and grain size on the Minority carrier lifetime in polycrystalline semiconductors,” *Solid State Communications*, vol.56, no.11, pp. 925-927, 1985.

[75] X. Wu, J. Zhou, A. Duda, J. C. Keane, T. A. Gessert, Y. Yan and R. Noufi, “13.9%-efficient CdTe Polycrystalline Thin-film Solar Cells with an Infrared Transmission of ~50%,” *Prog. Photovolt: Res. Appl.,* vol.14, pp.235-239, 2008.

[76] H. W. Yao, R. B. James, E. Y. Lee, R. W. Olsen, H. Hermon, R. J. Anderson,” Optical studies of the internal electric field distributions, crystal defects, and detector performance of CdZnTe radiation detectors,” *Proc. SPIE*, vol. 3446, p.169,1998.

[77] M. Schieber, H. Hermon, R. A. Street, S. E. Reddy, A. Zuck, A. I .Vilensky , L. Melekhov , R. Shatunovsky, M. Lukach, E. Meerson, Y. Saado, E. Pinkhasy, “Mercuric iodide thick films for radiological x-ray detector,” *Proc. SPIE*, Vol. 4142, p.197, 2000.

[78] H. L. Malm, and M. Martini, "Polarization phenomena in CdTe: Preliminary results," *Can. J. Phys.*, vol. 51, pp.2336-2340, 1973.